Title

Dynamics of Electron Relaxation Studied Using Time-Resolved Photoelectron Spectroscopy in Liquid Microjets

Author

Elkins, Madeline Hyde

Publication Date

2015

Dynamics of Electron Relaxation Studied Using Time-Resolved Photoelectron Spectroscopy in Liquid Microjets

by

Madeline Hyde Elkins

A dissertation submitted in partial satisfaction of the

requirements for the degree of

Doctor of Philosophy

in

Chemistry

in the

Graduate Division

of the

University of California, Berkeley

Committee in charge:

Professor Daniel M. Neumark, Chair
Professor Richard J. Saykally
Professor Yuen-Ron Shen

Fall 2015

Dynamics of Electron Relaxation Studied Using Time-Resolved Photoelectron Spectroscopy in Liquid Microjets

Abstract

Dynamics of Electron Relaxation Studied Using Time-Resolved Photoelectron Spectroscopy in Liquid Microjets

by

Madeline Hyde Elkins

Doctor of Philosophy in Chemistry

University of California, Berkeley

Professor Daniel M. Neumark, Chair

The solvated electron, an isolated electron in polar solution, is a species of fundamental interest to the physics of solvation and to the understanding of condensed phase reactions in the presence of ionizing radiation. In radiation chemistry and biology, the solvated electron acts as a powerful reductant and has been shown to act as a reagent in a wide range of processes from atmospheric chemistry to radiation-induced DNA damage. As the "simplest" quantum mechanical solute, the solvated electron serves as a fundamental probe of solute-solvent interaction and thus has been used as a model system for studying solvation processes.

Here, time-resolved photoelectron spectroscopy is used to study the binding motifs and solvation dynamics of solvated electrons in various polar solvents. This thesis is separated into three parts: first, an introduction to the research and description of the apparatus, second, results from experiments on the relaxation dynamics of the solvated electron after photoexciation and after generation by charge-transfer-to-solvent and, third, preliminary designs and proposed experiments for a liquid jet photoelectron spectrometer with attosecond time resolution.

Dedicated to my parents
Donna Hyde-Elkins and James Elkins

Contents

List of Figures

Acknowledgments

I have truly loved my time in grad school. Some of it, I have only enjoyed in hindsight, but the good was worth the bad. To Dan and to my parents, whose advice and support made this document possible, thank you.

I've had the privilege of working with two great labmates: Alexander Truesdell Shreve and Holly L. (H.) Williams. I can't imagine doing science with two better friends. Thank you, Holly, for reading and re-reading my dissertation, for food-bribes, for cat pictures, for bickering with me about data analysis, and for designing the figures that make our science look sexy. To Alex, thank you for visiting from Portland just to make me a schedule, for unplanned trips to Yosemite, for letting a first-year boss you around, and for phrases like "stupid for historical reasons", "less actively user-hostile", and "local physics-free zone".

Thank you to my classmates, Neil Cole-Filipiak and Sarah King, who made first year bearable, who suffered through quals with me, and who made grad school a team sport. Thank you, Sarah, for guiding me through the hills of Berkeley via road bike and not minding when I drafted shamelessly. Thank you for 12 pages of practice qual notes and reminding me that quiting was an option, but not one either of us would take, *ever*. Thank you, Neil, for introducing me to beer and to Scotch, for just letting me vent, for poop jokes, for lending me The Animated Series for a solid year, and for surviving "the thesis" with me.

Thank you to the Neumark Group for a support network in grad school, for advice, and for friendships forged through late-nights and broken equipment. Thanks especially to Maggie Yandell-Zhao and Ryan Young for letting me borrow half their optics drawer and explaining ten years of solvent cluster anion data. Thanks also to Tom Oliver, once of the Fleming Group and now of the Oliver Group, for all of the gossip and The Thick of It.

Michelle Haskins single-handedly makes everything in the group run smoothly. I hope she knows how much science she makes possible simply by making bureaucratic problems go away. Thank you so much.

Thank you, Lucy Archer, my favorite Berzerkelian, for late night and early morning phone calls, for being offended, for archery questions and bike questions, and for a place to crash (on two continents, in two countries, and in three states).

Cal Archery absorbed more of my free time over the last five years than I care to admit. To my teammates, to the archers that I coached, to Professor/Coach/Faculty-Advisor/Trouble-Maker Dennis Lieu, to Coach Rafael Recto, and to Coach Hye-Youn Park thank you and Go Bears!

Finally, thank you to Alphonse Teng, Andrea Spacht, Sterling Collins, Chris Schantz, and Alex Wen for taco-Tuesdays, spinnaker practice, and reminding me that there is life outside of academia.

Part I

Introduction and Methods

Chapter 1

Introduction

1.1 Overview

The study of water is crucial to the understanding of life and its underlying chemistry. While reactions that take place in a vacuum may be easier to study in absolute energetic detail, an enormous amount of chemistry takes place in a bath of fluid, especially one of water. This liquid environment fundamentally alters the chemistry taking place inside it. The nature of a solvent can change the outcome of a reaction. It changes the energy of the various quantum states. It can absorb or donate energy to the components dissolved in it. This family of effects, solvation phenomena, shapes the nature of the solute in time regimes from years to attoseconds and in energy regimes from terahertz to soft x-rays.

The first step in studying an exceedingly complex problem is to reduce its dimensionality. An electron, a subatomic particle with no known substructure, may be the simplest solute imaginable. It has no known internal degrees of freedom nor does it have any discrete quantum states in the absence of a confining potential. For this reason, the spectrum of the electron is entirely determined by its environment, which makes it a perfect probe of the solvent. The work presented here concerns the study of electrons in water and other solutions as a model solute and of how their energy changes in real time.

The following sections of this chapter introduce the motivation and relevant background information for the subsequent chapters. Chapter 2 discusses the experimental methods, and Chapter 3 pertains to analysis of the time-resolved data. Chapters 4 through 6 discuss solvated electron dynamics in various solutions on a femtosecond timescale (10^{-15}s). The focus changes in Chapter 7 to proposed experiments and preliminary design work for a liquid jet, time-resolved photoelectron spectrometer with attosecond time resolution (10^{-18}s). Finally, the appendices include designs for optical assemblies, data analysis code, and technical drawings.

1.2 Dynamics of Solvated Electrons

While dissolving an electron in water might seem complicated, so-called hydrated electrons are produced in nature when water is exposed to ionizing radiation (from the sun for instance) and subsequently last for microseconds. In fact, hydrated electrons have proven to be a relatively ubiquitous species in radiation chemistry [1] and have been implicated in biological processes such as the radiative damage of DNA[2].

The first scientific paper demonstrating the synthesis of an electron dissolved in a fluid, or solvated electron, was published by W. Weyl in 1864[3], who thought he had made a novel metallic compound similar to the ammonium amalgam by dissolving sodium and potassium in ammonia; however, the brilliant color of alkali metals dissolved in gaseous ammonia was certainly known to Sir Humphry Davy circa 1809[4]. That a free electron was responsible for the conduction in these solutions was first proposed by Charles Kraus in 1908. The same paper also happens to be the first instance of the cavity model of the solvated electron, wherein he describes the electron as "surrounded by an envelope of solvent molecules"[5]. The structure of the solvated electron remains a hotly debated topic even one hundred and two years later[6].

The first use of the term "solvated electron" is credited to George Gibson and William Argo, also working at UC Berkeley, who demonstrated that the color seen by Weyl was in fact due an electron trapped by locally oriented solvent molecules[7]. In water, hydrated electrons were first identified by their absorption spectrum at 720 nm by Hart and Boag in 1962[8]. Their pulsed radiolysis work inspired a large body of similar studies concerning the reactions of electrons in solution on microsecond timescales[9].

Since then, the solvated electron has been implicated in thousands of scientific articles on subjects ranging from the photochemistry of DNA[10] to the well known Birch reduction in synthetic organic chemistry[11]. In Part II, our aim is to study how the spectrum of the solvated electron evolves in real time after generation by charge-transfer-to-solvent and after optical excitation of the absorption band identified by Hart and Boag.

1.2.1 Charge-Transfer-to-Solvent Dynamics

An efficient and relatively general way of creating solvated electrons is via the charge-transfer-to-solvent (CTTS) bands of halides dissolved in solution[12, 13]. Though these ions have no bound excited states in the gas phase, in solution they have broad absorption bands in the ultraviolet (UV) which allow for ejection of an electron into the surrounding solvent network [14, 15]. Halides have two CTTS states, the ${}^2P_{3/2}$ and ${}^2P_{1/2}$ states, which are named for the spin orbit states of the halogens generated by photodetachment of a halide. Unlike gas phase photodetachment of iodide, these bands are below the threshold for detaching the electron to vacuum; instead, the transient state excited at this band is stabilized by the solvent network yielding solvated electrons[16]. These CTTS bands lie in the UV and are separated by a similar spin-orbit splitting as exhibited by the halogen in the gas phase. It is by the splitting of these two peaks that Frank and Scheibe first inferred the that the bands they discovered in iodide led to the production of electrons in 1928[14].

Transient absorption studies of CTTS processes in water[17–20] and methanol[21] form the bulk of the prior work on the dynamics of CTTS. These experiments are complemented by theory [22–24] and provide a detailed picture of the solvation dynamics. First, the CTTS band rapidly evolves on a timescale of hundreds of femtoseconds leading to the ejection of electrons. The electrons at this stage still remain in some proximity to the parent iodine atom. After this point, the kinetics branch into those electrons which recombine with the parent neutral and those which diffuse away, thereby escaping recombination. Both processes have timescales of tens to hundreds of picosceconds but, because the pair diffusion rate is faster than the recombination rate, some fraction of the electrons survive into the nanosecond and longer time regime. The survival probability ranges from 30% in water to 70% in methanol.

1.2.2 The Excited State of the Solvated Electron

In the cavity picture of the solvated electron, the spectrum of the electron can be modeled as a particle in a quasi-spherical well. This picture seems to be relatively robust, and even more sophisticated quantum chemical models yield an "*s*-like" ground state and set of nearly degenerate "*p*-like" excited states as the two bound, localized states of the solvated electron, exactly as expected from the particle-in-a-box model. Beyond the *p*-state, the excited states of the electron begin to couple to the diffuse conduction band of the solvent. These bands lead to the characteristic absorption band in the near infrared (NIR) originally observed in water in 1962.

The relaxation of the electron after excitation of the $s \rightarrow p$ band is a model case of solvent mediated, electronically non-adiabatic dynamics in solution, and as such, much theoretical[25–32] and experimental[33–37] effort has gone in to investigating the dynamics subsequent to $s \rightarrow p$ excitation. Much of the history of experimental work in this system was done using transient absorption (TA). In water, early characterization of the relaxation mechanism of the hydrated electron after photoexcitation was performed in pioneering work in the Barbara Group [33]. These experiments were later performed in methanol by Silva [34] and later Thaller [35]. They were able to measure three lifetimes (<100 fs, 200-400 fs, and 1.1 ps) but were unable to conclusively assign to which processes each lifetime belonged.

Two mechanisms have been proposed: the "adiabatic" and "non-adiabatic" mechanisms[33]. In the adiabatic mechanism, the fastest observable lifetime in the TA data is assigned to relaxation on the *p*-state surface. The few hundred femtosecond lifetime is assigned to internal conversion between the *s* and *p* states. The final lifetime is assigned to relaxation of the solvent on the ground state. In the “non-adiabatic” mechanism, the <100 femtosecond lifetime corresponds to internal conversion and the ground state relaxes via a two step mechanism. Identification of the relaxation mechanism hinges upon the assignment of the internal conversion lifetime. In Chapters 4, 5, and 6, the relaxation of the excited state of the solvated electron is studied in a variety of polar solvents with the goal of elucidating the nature of this relaxation mechanism.

1.2.3 Microsolvation in Clusters and Extrapolation to the Bulk

Microsolvation studies in solvent cluster anions provide a complementary perspective to this work. [38, 39] By observing the onset of “bulk-like” properties as a function of cluster size, the study of gas phase clusters provides a tractable proxy for studying the bulk with significantly reduced degrees of freedom and the state specificity of a jet cooled molecular beam. Further, these small systems require significantly reduced computational cost as compared to the bulk, allowing for accurate theoretical modeling. Water, deuterium oxide, methanol, acetonitrile, and tetrahydrofuran cluster anions, clusters of solvent molecules with an excess electron, have all been used to predict bulk properties such as binding energies and solvation timescales[40–43]. Further, clusters of water and methanol with an iodide anion have been used as a model system for studying charge transfer dynamics in clusters and as a proxy for studying charge-transfer-to-solvent in the bulk[44–46].

The first test of these extrapolation methods was a measurement of the vertical binding energy of the solvated electron in various solvents. Figure 1.1 shows a plot of the binding energy as a function of cluster size of the solvated electron in various solvent cluster anions including: water, methanol, and acetonitrile[47–53]. Also shown are the measured binding energies found by various groups using liquid jet photoelectron spectroscopy. In 2010, four groups were able to show that the binding energy of the hydrated electron was in remarkable agreement with predicted results from water cluster anions[47–51]. From water alone, it would seem that extrapolation is a powerful and reliable tool for studying the bulk.

In methanol, the agreement between the extrapolated results and the bulk are not so close: 2.4 eV from the extrapolation and 3.4 eV for the bulk[52, 53]. In acetonitrile, which has two bulk binding motifs[54], there is good agreement between the extrapolated binding energy for isomer II and the bulk binding energy of the dimer bound state; however, for the solvated electron there is yet another ∼1 eV gap between the predicted and measured binding energy [52]. It seems clear that direct extrapolation from even vary large cluster isomers has mixed success predicting bulk binding energies. A motivator for this work is to measure solvation timescales in the bulk as a direct test of extrapolated values from gas-phase clusters.

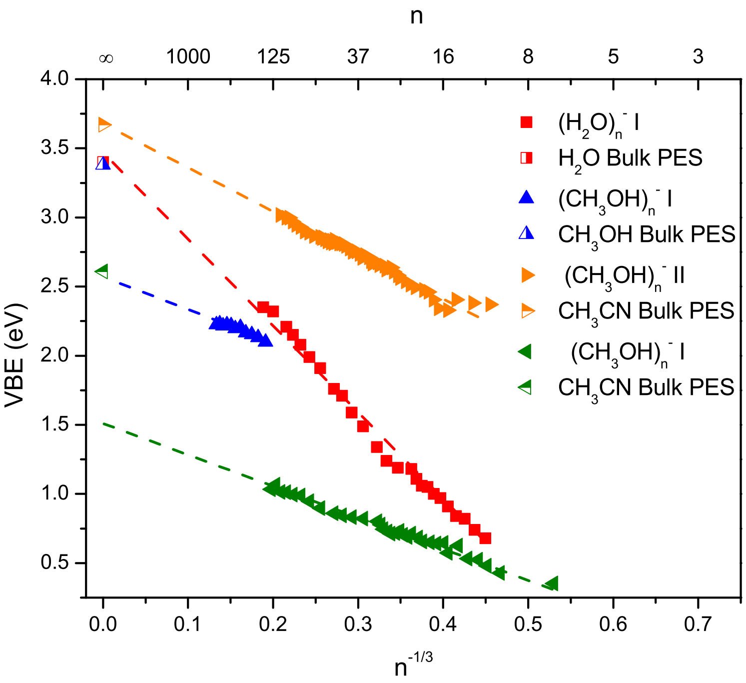

Figure 1.1: Solvent cluster anion data, extrapolations, and bulk VBE for three solvents. In water and methanol, cluster anion data are shown for isomer I, which is generally accepted as the cavity bound species. In acetonitrile, isomer I is assigned to the cavity bound state and isomer II to a dimer bound anion.

1.3 Attosecond Dynamics in Liquid Jets

The development of chirped pulse amplification in conjunction with titanium doped sapphire lasers opened the field of ultrafast chemistry[55]. As these techniques become more sophisticated, it becomes possible to study the motions of electrons rather than simply nuclear motion with attosecond resolution[56]. The frontier of ultrafast chemistry now lies at the fastest extreme of achievable pulse durations, about one hundred attoseconds, and beyond the easily achievable energy range of commercial ultrafast lasers using mixing crystals, about six electron volts.

As the field of attosecond science develops, experiments with sub-femtosecond resolution in the gas phase have become increasingly common[57]. Recently, it has become possible to study electron dynamics in solid phase, for example, the evolution of the band gap in silicon after carrier formation in the conduction band[58]. The study of electron dynamics in the liquid phase remains an unexplored frontier. In Chapter 7, proposed experiments and preliminary designs are presented with the aim of studying electronically non-adiabatic dynamics mediated by a liquid solvent on a attosecond timescale

1.4 Principles of Photoelectron Spectroscopy

All of the experiments presented here, in some fashion, make use of photoelectron spectroscopy (PES)[59, 60]; therefore, a description of this method must be provided before proceeding. If a photon interacts with molecule or atom with energy, hν, greater than the binding energy of an electron, eBE, that electron will be detached from the parent species. By conservation of energy, the emitted photoelectron will leave with some amount of kinetic energy equal to the difference between the photon energy and the binding energy, as given by the energy balance:

$$eKE = h\nu - eBE \tag{1.1}$$

As implied in the equation above, electrons photodetached from different quantum states will be emitted with different kinetic energies. The photoelectron spectrum is the intensity of detached electrons as a function of kinetic energy, or as appropriate binding energy, for that species.

The intensity of the spectrum at a particular energy is related to the photodetachment cross section via the transition rate, which is given by Fermi's golden rule. This states that rate of transition from an initial state, i, to a final state, f, is proportional to the square of the expectation value of the transition dipole moment, μ, connecting the two states scaled by the density of final states.

$$\Gamma_{f\leftarrow i} \propto |\langle\Psi_f|\hat{\mu}|\Psi_i\rangle|^2\rho(E_f) \tag{1.2}$$

In the Born-Oppenheimer approximation, the electronic and nuclear coordinates are assumed to be separable. This is a reasonable approximation if the nuclear motion is "slow" relative to the electronic motion. The initial and final state wave functions can then be approximated as products of the electronic wave function, which depends on the electronic and nuclear coordinates, $\phi(r_i, R_\alpha)$, and the nuclear wave function, which depends only on the nuclear coordinates, $\chi(R_\alpha)$: $\Psi = \phi(r_i, R_\alpha)\chi(R_\alpha)$. Substituting in the new equation for the wave function and simplifying yields the relation below:

$$\Gamma_{f\leftarrow i} \propto |\langle\phi_f(r_i, R_\alpha)|\hat{\mu}|\phi_i(r_i, R_\alpha)\rangle^2\langle\chi_f(R_\alpha)|\chi_i(R_\alpha)\rangle|^2\rho(E_f) \tag{1.3}$$

The relation $|\langle\phi_f|\hat{\mu}|\phi_i\rangle|^2$ contains the orbital selection rules for the transition, and the relation $|\langle\chi_f|\chi_i\rangle|^2$ is the Frank-Condon factor. The Frank-Condon factor scales the intensity of the transition such that initial and final states with similar nuclear wave functions have a high transition rate and therefore a high intensity. Conversely, a transition with no overlap in the nuclear wave functions is not allowed, even if there is sufficient energy to access the state. More conceptually, the Frank-Condon factor can be thought of as a geometric consideration. If the geometry of the final state resembles that of the initial state, the transition is likely to occur.

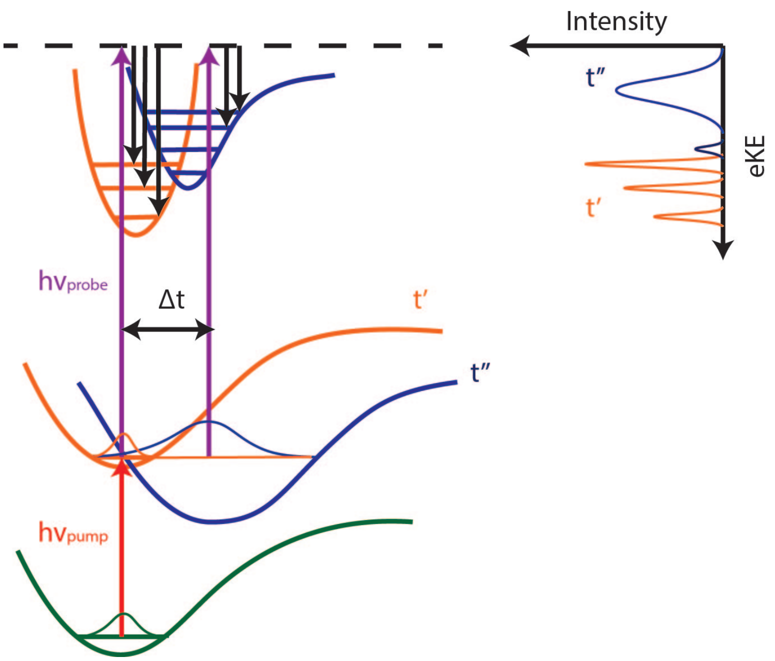

Figure 1.2: Time resolved photoelectron spectroscopy: With a first pulse, the system is perturbed from its initial state. The perturbed state can then evolve with time from t' to t", and at a variable delay Δt, an electron is detached with the a second laser pulse. A PES for the two delays is shown vertically. The intensity of the transition is proportional to the Frank-Condon factor connecting the prepared state and the manifold of photodetached states.

The impact of the Frank-Condon factor on the photoelectron spectrum is illustrated in graphical form in Fig 1.2. The transition between the initial state and the final state can be represented by a vertical line connecting the two states at the same location on a common nuclear coordinate. If a set of nuclear wave functions is superimposed upon the potential energy diagram, for example, the simple harmonic oscillator wave functions, we see that there exist coordinates at which the amplitude of the wave function is high in both the initial and final state and some where there is no overlap at all. These amplitudes are reflected in the spectrum shown vertically in the diagram. In solution, features in the photoelectron spectrum are significantly broadened, due in part to the wide range of accessible solvent configurations. Because of the width of these distributions, the quantity of interest for much of the work presented here is the vertical binding energy (VBE) characterized by the peak of the binding energy distribution. The VBE can also be understood as the point of maximum Frank-Condon overlap and is characteristic of the spectrum regardless of photon energy.

1.5 Time-Resolved Photoelectron Spectroscopy

With ultrafast laser pulses, it is possible to monitor how photoelectron spectra change in time via a pump-probe experiment. In these experiments, a first pulse excites the species of interest and, after some delay, a second pulse is then used to generate a photoelectron spectrum. The photoelectron spectrum as a function of delay between the two pulses is a map of how the populations in different quantum states evolve with time.

As a toy system[61], assume a three state model where an initial state, 1, is optically excited to a second state, 2. State 2 is then probed by a photon which couples 2 to state, 3. Finally, assume no transition is allowed directly between 1 and 3. This provides a decent model for any pump-probe spectroscopy with a single intermediate state. The dynamics of this simple system can be understood using second order time-dependent perturbation theory. The time-dependent wave function can be expanded in the fashion below.

$$a_{f\leftarrow i} = \delta_{i,f} + \frac{1}{i\hbar}\int_0^t dt' \langle f|H'_{pump}|i\rangle + \frac{1}{\hbar^2}\int_0^t \int_0^{t'} dt'dt'' \langle f|H'(t')_{pump} H'(t'')_{probe}|i\rangle \tag{1.4}$$

The first term is zero since the initial and final states are different and the second is also zero since there is no allowed transition from state 1 to state 3. By resolution of the identity, the third term can be written:

$$a_{f\leftarrow i} = \frac{1}{\hbar^2}\sum_n \int_0^t \int_0^{t'} dt'dt'' \langle f|H'(t')_{probe}|n\rangle\langle n|H'(t'')_{pump}|i\rangle. \tag{1.5}$$

The expression above is a sum over states that couple the initial state to the final state. Since there is only one intermediate in our toy system, we can drop the sum and consider only the one intermediate. Next, by making the Born-Oppenheimer Approximation and inserting $H' = \vec{\mu}\cdot\vec{\epsilon}$ for the perturbation, we can rewrite the expression as follows:

$$a_{f\leftarrow i} \propto \int_0^t \int_0^{t'} dt'dt'' \langle \phi_f|\vec{\mu}\cdot\vec{\epsilon}_{probe}|\phi_n\rangle\langle\chi_f|e^{-iH''(t''-t'')}|\chi_n\rangle\langle\phi_n|\vec{\mu}\cdot\vec{\epsilon}_{pump}|\phi_i\rangle\langle\chi_n|\chi_i\rangle. \tag{1.6}$$

Finally, the transition rate is related to the square of the time-dependent wave function. As in the last section, the transition rate is subject to the Frank-Condon factors coupling each pair of states. As a futher complication, if the intermediate state is allowed to evolve in time, the transition rate then becomes dependant on the time evolving Frank-Condon factors. Since the transition dipole operator contains the amplitude of the electric field coupling the states, the transition probability is linear in the intensity of each driving field.

1.6 Summary of Systems Studied

1.6.1 Charge-Transfer-to-Solvent Dynamics in Methanol

In Chapter 5, the charge-transfer-to-solvent dynamics in methanol are studied using TRPES. The nascent solvated electron undergoes a two step solvation process involving rapid evolution of the CTTS state and a solvation shift of the hot ground state population. Once equilibrated with solution, the electrons may then diffuse away from the parent iodine atom or undergo geminate recombination to form iodide. >50% of electrons escape this recombination step and live well past the observation window.

1.6.2 Excited State Relaxation Dynamics in Water, Deuterated Water, and Methanol

In Chapter 4, the relaxation mechanism of the hydrated electron is studied using TRPES. The lifetime of the excited state of the electron in water is found to be 75 ± 20 fs. This lifetime is in agreement with results from TA, solvent cluster anions, and the "non-adiabatic" mechanism. Finally, the first measurement of the VBE of the excited state of the hydrated electron is reported, 2.5 eV. In Chapter 5, the dynamics of the excited state of the solvated electron in methanol is investigated. Significantly longer excited state lifetimes are measured in the alcohols; however, the measured dynamics present a kinetic mechanism that is consistent with results in water.

Finally, in Chapter 6, the effect of isotopic substitution on the relaxation mechanism is studied. The internal conversion lifetime of the solvated electron in deuterium oxide is found to slow by a factor of 1.3 ± 0.1. The ground state solvation time is unchanged. This provides further evidence for our assignment of the non-adiabatic mechanism.

1.7 References

[1] B. C. Garrett, D. A. Dixon, D. M. Camaioni, D. M. Chipman, M. A. Johnson, C. D. Jonah, G. A. Kimmel, J. H. Miller, T. N. Rescigno, P. J. Rossky, S. S. Xantheas, S. D. Colson, A. H. Laufer, D. Ray, P. F. Barbara, D. M. Bartels, K. H. Becker, K. H. Bowen, S. E. Bradforth, I. Carmichael, J. V. Coe, L. R. Corrales, J. P. Cowin, M. Dupuis, K. B. Eisenthal, J. A. Franz, M. S. Gutowski, K. D. Jordan, B. D. Kay, J. A. LaVerne, S. V. Lymar, T. E. Madey, C. W. McCurdy, D. Meisel, S. Mukamel, A. R. Nilsson, T. M. Orlando, N. G. Petrik, S. M. Pimblott, J. R. Rustad, G. K. Schenter, S. J. Singer, A. Tokmakoff, L.-S. Wang, and T. S. Zwier, Chem. Rev. **105**, 355 (2005).

[2] B. Boudaïffa, P. Cloutier, D. Hunting, M. A. Huels, and L. Sanche, Science **287**, 1658 (2000).

[3] W. Weyl, Annalen der Physik **197**, 601 (1864).

[4] H. Davy, "The Bakerian Lecture of 1809," in *The Collected Works of Sir Humphry Davy*, Vol. V (Smith, Elder, & Co., London, 1840).

[5] C. A. Kraus, J. Am. Chem. Soc. **30**, 1323 (1908).

[6] R. E. Larsen, W. J. Glover, and B. J. Schwartz, Science **329**, 65 (2010).

[7] G. E. Gibson and W. L. Argo, J. Am. Chem. Soc. **40**, 1327 (1918).

[8] E. J. Hart and J. W. Boag, J. Am. Chem. Soc. **84**, 4090 (1962).

[9] E. J. Hart and M. Anbar, *The Hydrated Electron* (Wiley-Interscience, New York, NY, 1970) p. 267.

[10] J. Gu, J. Leszczynski, and H. F. Schaefer, Chem. Rev. **112**, 5603 (2012).

[11] A. J. Birch, Journal of the Chemical Society (Resumed) , 430 (1944).

[12] X. Y. Chen and S. E. Bradforth, Annu. Rev. Phys. Chem. **59**, 203 (2008).

[13] F. H. Long, X. L. Shi, H. Lu, and K. Eisenthal, J. Phys. Chem. **98**, 7252 (1994).

[14] J. Frank and G. Scheibe, Zeitschrift Fur Physikalische Chemie A **139**, 22 (1928).

[15] M. J. Blandamer and M. F. Fox, Chem. Rev. **70**, 59 (1970).

[16] J. Jortner, M. Ottolenghi, and G. Stein, J. Phys. Chem. **68**, 247 (1964).

[17] J. A. Kloepfer, V. H. Vilchiz, V. A. Lenchenkov, A. C. Germaine, and S. E. Bradforth, J. Chem. Phys. **113**, 6288 (2000).

[18] J. A. Kloepfer, V. H. Vilchiz, V. A. Lenchenkov, X. Y. Chen, and S. E. Bradforth, J. Chem. Phys. **117**, 766 (2002).

[19] J. A. Kloepfer, V. H. Vilchiz, V. A. Lenchenkov, and S. E. Bradforth, Chem. Phys. Lett. **298**, 120 (1998).

[20] H. Iglev, A. Trifonov, A. Thaller, I. Buchvarov, T. Fiebig, and A. Laubereau, Chem. Phys. Lett. **403**, 198 (2005).

[21] V. H. Vilchiz, X. Chen, J. A. Kloepfer, and S. E. Bradforth, Radiat. Phys. Chem. **72**, 159 (2005).

[22] W.-S. Sheu and P. J. Rossky, J. Phys. Chem. **100**, 1295 (1996).

[23] A. Staib and D. Borgis, J. Chem. Phys. **104**, 9027 (1996).

[24] S. E. Bradforth and P. Jungwirth, J. Phys. Chem. A **106**, 1286 (2002).

[25] L. Turi and P. J. Rossky, Chem. Rev. **112**, 5641 (2012).

[26] B. J. Schwartz and P. J. Rossky, J. Chem. Phys. **101**, 6902 (1994).

[27] B. J. Schwartz and P. J. Rossky, J. Chem. Phys. **101**, 6917 (1994).

[28] K. Fueki, D. F. Feng, and L. Kevan, Chem. Phys. Lett. **10**, 504 (1971).

[29] P. Mináry, L. Turi, and P. J. Rossky, J. Chem. Phys. **110**, 10953 (1999).

[30] A. A. Mosyak, O. V. Prezhdo, and P. J. Rossky, J. Chem. Phys. **109**, 6390 (1998).

[31] A. A. Zharikov and S. F. Fischer, J. Chem. Phys. **124**, 054506 (2006).

[32] J. Zhu and R. I. Cukier, J. Chem. Phys. **98**, 5679 (1993).

[33] K. Yokoyama, C. Silva, D. H. Son, P. K. Walhout, and P. F. Barbara, J. Phys. Chem. A **102**, 6957 (1998).

[34] C. Silva, P. K. Walhout, P. J. Reid, and P. F. Barbara, J. Phys. Chem. A **102**, 5701 (1998).

[35] A. Thaller, R. Laenen, and A. Laubereau, J. Chem. Phys. **124**, 024515 (2006).

[36] M. Assel, R. Laenen, and A. Laubereau, Chem. Phys. Lett. **317**, 13 (2000).

[37] M. S. Pshenichnikov, A. Baltuska, and D. A. Wiersma, Chem. Phys. Lett. **389**, 171 (2004).

[38] D. M. Neumark, Mol. Phys. **106**, 2183 (2008).

[39] R. M. Young and D. M. Neumark, Chem. Rev. **112**, 5553 (2012).

[40] A. E. Bragg, J. R. R. Verlet, A. Kammrath, O. Cheshnovsky, and D. M. Neumark, Science **306**, 669 (2004).

[41] A. Kammrath, G. B. Griffin, J. R. R. Verlet, R. M. Young, and D. M. Neumark, J. Chem. Phys. **126**, 244306 (2007).

[42] R. M. Young, M. A. Yandell, M. Niemeyer, and D. M. Neumark, J. Chem. Phys. **133**, 154312 (2010).

[43] R. M. Young, G. B. Griffin, A. Kammrath, O. T. Ehrler, and D. M. Neumark, Chem. Phys. Lett. **485**, 59 (2010).

[44] L. Lehr, M. T. Zanni, C. Frischkorn, R. Weinkauf, and D. M. Neumark, Science **284**, 635 (1999).

[45] J. R. R. Verlet, A. E. Bragg, A. Kammrath, O. Cheshnovsky, and D. M. Neumark, Science **310**, 1769 (2005).

[46] R. M. Young, M. A. Yandell, and D. M. Neumark, J. Chem. Phys. **134**, 124311 (2011).

[47] K. R. Siefermann, Y. X. Liu, E. Lugovoy, O. Link, M. Faubel, U. Buck, B. Winter, and B. Abel, Nature Chemistry **2**, 274 (2010).

[48] A. Lübcke, F. Buchner, N. Heine, I. V. Hertel, and T. Schultz, Phys. Chem. Chem. Phys. **12**, 14629 (2010).

[49] K. Suzuki, Y. Ohmori, and E. Ratel, Plant Cell Physiol. **52**, 1697 (2011).

[50] H. Shen, N. Kurahashi, T. Horio, K. Sekiguchi, and T. Suzuki, Chem. Lett. **39**, 668 (2010).

[51] A. T. Shreve, T. A. Yen, and D. M. Neumark, Chem. Phys. Lett. **493**, 216 (2010).

[52] A. T. Shreve, M. H. Elkins, and D. M. Neumark, Chemical Science **4**, 1633 (2013).

[53] T. Horio, H. Shen, S. Adachi, and T. Suzuki, Chem. Phys. Lett. **535**, 12 (2012).

[54] I. A. Shkrob and M. C. Sauer, J. Phys. Chem. A **106**, 9120 (2002).

[55] A. H. Zewail, Journal of Physical Chemistry A **104**, 5660 (2000).

[56] M. Drescher, M. Hentschel, R. Kienberger, G. Tempea, C. Spielmann, G. A. Reider, and F. Krausz, Science **291**, 1923 (2001).

[57] L. Gallmann, C. Cirelli, and U. Keller, Annual Review of Physical Chemistry **63**, 447 (2012).

[58] M. Schultze, K. Ramasesha, C. D. Pemmaraju, S. A. Sato, D. Whitmore, A. Gandman, J. S. Prell, L. J. Borja, D. Prendergast, K. Yabana, D. M. Neumark, and S. R. Leone, Science **346**, 1348 (2014).

[59] T. Suzuki and B. J. Whitaker, Int. Rev. Phys. Chem. **20**, 313 (2001).

[60] A. Stolow, A. E. Bragg, and D. M. Neumark, Chem. Rev. **104**, 1719 (2004).

[61] V. S. Batista, M. T. Zanni, B. J. Greenblatt, D. M. Neumark, and W. H. Miller, J. Chem. Phys. **110**, 3736 (1999).

Chapter 2

Experimental Methods

2.1 Overview

The designs for the liquid-jet photoelectron spectrometer used for these experiments is presented in the thesis of Alexander T. Shreve [1]. The apparatus was assembled per Dr. Shreve's designs after his graduation in December of 2012; however, a number of changes to the original designs were made during the commissioning process. As such, a full description of the instrument in its current form is warranted. A full description of the principles of jets and the practical implementation of the liquid source is described in detail in both Alexander T. Shreve's thesis and the thesis of Terry A. Yen [2] and will not be repeated here.

2.2 Liquid Microjets

Photoelectron spectroscopy (PES) is typically a high vacuum technique[3, 4]. The most basic description of a PES experiment is that a photon goes in and an electron comes out carrying with it information about species from which it came. If we want to access that information, the electron must not be "disturbed" on its way to the detector. If the photoelectron encountered, a background gas molecule on the way to the detector, that collision would change the measured kinetic energy of the electron. It is important, therefore, that we know what the average distance is that an electron can travel without undergoing collisions. This distance is the "mean free path" of the electron, and for a 1 eV electron at atmospheric pressure, that distance is less than 5 μm. Since a 5 μm flight length is much too short for practical purposes, it is necessary to remove as much excess gas from the chamber as possible.

With turbomolecular pumps and vacuum chambers, it poses little difficulty to reach pressures low enough to study gas phase species; however, when using a liquid source with a high vapor pressure, gas molecules evaporate from the liquid surface. This dense vapor layer significantly reduces the electron mean free path. The mean free path of an electron traveling through water vapor at its equilibrium vapor pressure is only 11 μm. The amount of evap-

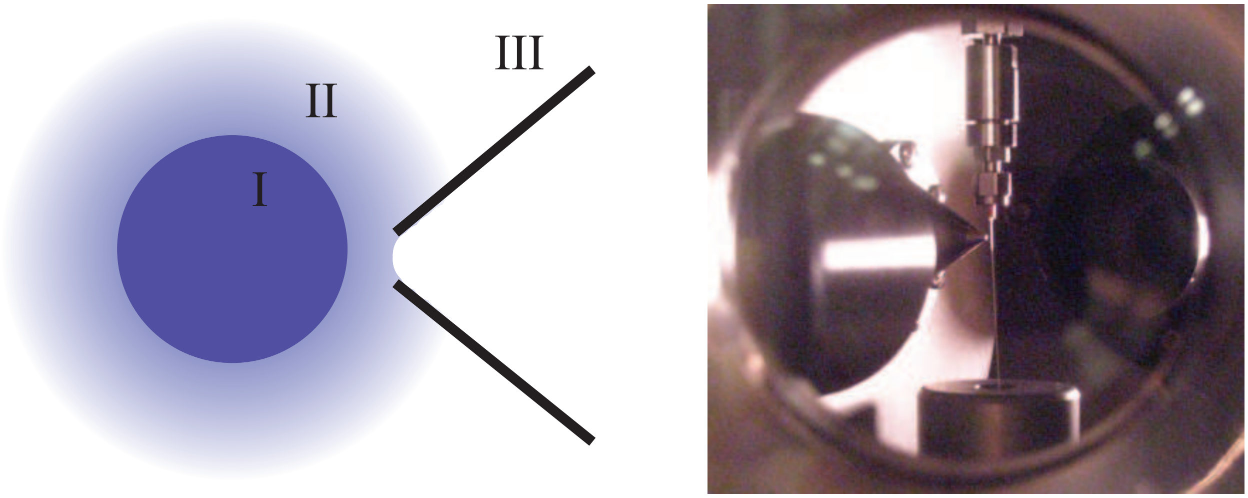

Figure 2.1: Left: Schematic cross section of the liquid jet (I), vapor layer (II), and skimmer(III). Right: Photograph of the liquid jet in the chamber.

orated gas can be reduced greatly by simply limiting the surface area for evaporation. For a sufficiently thin jet of liquid flowing in a vacuum, gas molecules evaporate “ballistically”. Which is to say, liquid evaporates radially from the surface and does not condense back onto the surface of the jet. In this geometry, the gas density falls off as the inverse of the distance away from the jet, r_0/r[5]. In order to make the mean free path longer, one need only make the jet diameter, r_o, small and the path length through the vapor as short as possible.

Practically, a small jet diameter is achieved by pushing a liquid at high backing pressure (∼100 atm) through a 20 μm inner diameter fused silica capillary. A full description of the jet design is provided elsewhere[1, 2]. Briefly, the capillary is held by a small PEEK tube mounted in a 1/16th inch Swagelock fitting. The Swagelock fitting is in turn attached to an in-line filter assembly with a 5 μm pore size. This filter helps limit clogging of the liquid jet by particulate contamination.

The high backing pressure for the jet assembly is provided by a 500 mL syringe pump (Teledyne Isco). The pump is capable of producing up to 200 atm of backing pressure. Though the pump can be operated in a constant pressure mode, typically the backing pressure is continuously modified to provide a constant liquid flow velocity of between 0.25 and 0.5 mL/min. This corresponds to a jet flow velocity of 10-25 m/s. At these flow velocities and with a one kilohertz experimental repetition rate, the sample of liquid interrogated by the lasers is renewed with every shot.

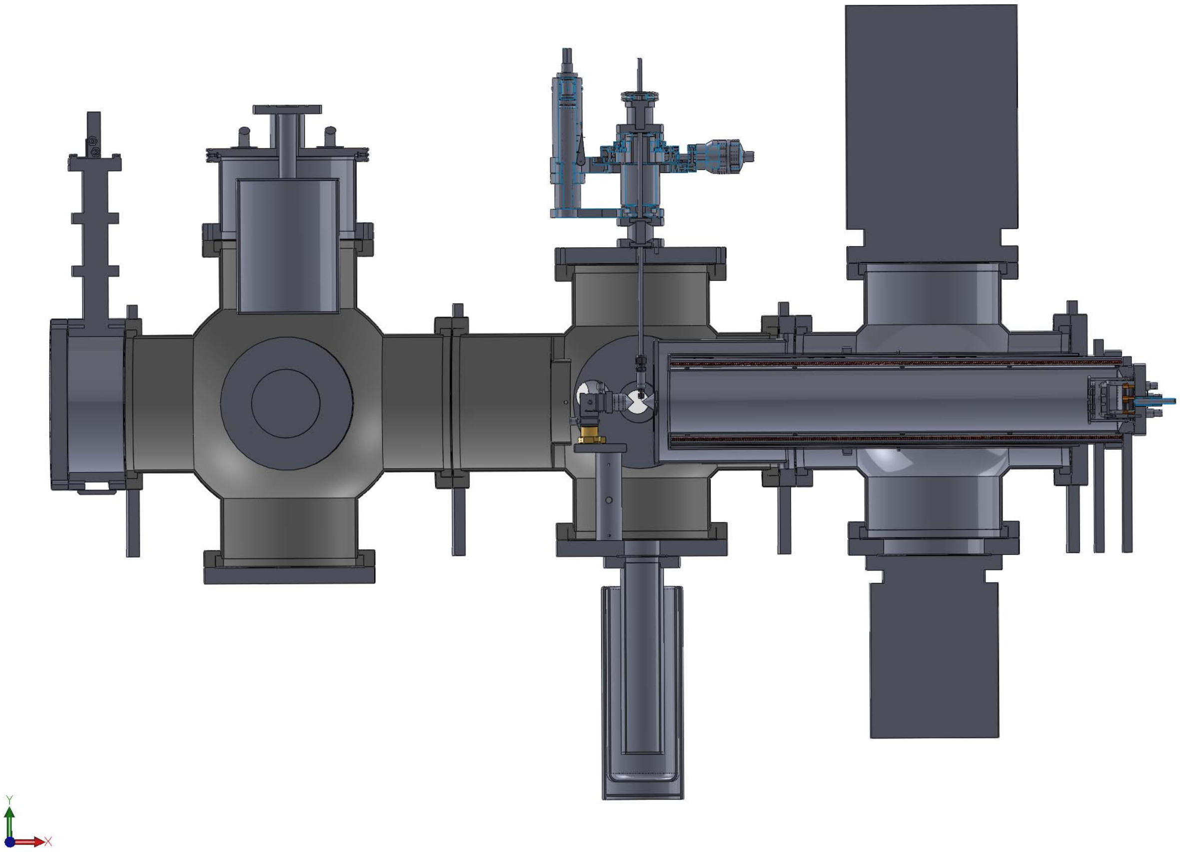

Figure 2.2: Liquid Jet Photoelectron Spectrometer in cross-section as of November 2015.

2.3 Photoelectron Spectrometer

The apparatus consists of a vacuum chamber containing the liquid jet and a magnetic bottle time-of-flight photoelectron spectrometer. The entire apparatus can be broken down into two sections: the trap chamber, which contains the liquid jet, and the detector chamber which contains the drift tube, solenoid, and detector. These two sections are separated by a skimmer with a 900 μm opening, which allows for differential pumping of the two regions. A full picture of the liquid jet apparatus is shown in Figure 2.2.

2.3.1 The Trap Chamber

In the trap chamber, the liquid of interest is pumped into vacuum at a backing pressure of approximately 100 atm through a 20 μm fused silica capillary. The jet assembly can be

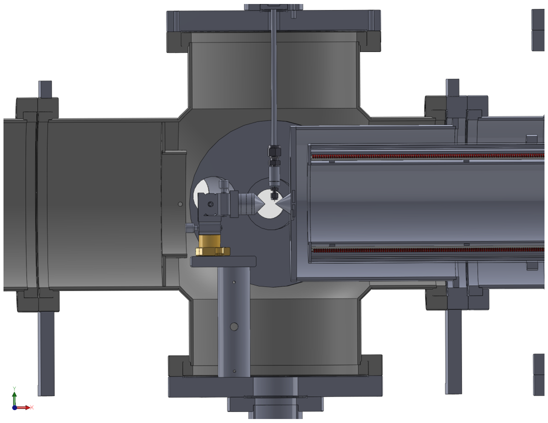

Figure 2.3: Main chamber of liquid microjet photoelectron spectrometer.

moved in three axes via a micrometer feedthrough on a bellows. The liquid is crossed with a sequence of laser pulses at the interaction point generating photoelectrons. For normal operation, the jet is placed 1 mm from a 900 μm skimmer. This is well inside the vapor layer created by the jet. The short distance between the jet and the skimmer limits the total path length of the ejected electrons through the vapor.

The photodetached electrons are then steered toward the detector by the rare earth magnets of the magnetic bottle, described in section 2.5. The magnetizable metal cone focuses the magnetic field of the magnets to a fine point which can be positioned by a three axis translation stage, described in more detail in section 2.5.1.

The evaporating liquid from the jet creates a large virtual leak inside the chamber. When running high vapor pressure liquids, cryogenic pumping is a very effective means of achieving low trap pressure. A seven liter liquid nitrogen dewar is kept continuously full while running. Though the dewar can be filled by hand, a secondary dewar with an additional 12 liters can be attached to the dewar which allows for 24 hr supply of liquid nitrogen. Below the liquid jet, a liquid nitrogen cooled trap catches the spent liquid and provides further cryogenic pumping. Despite the efficiency of cryogenic pumping, it takes time for the dewars to cool; therefore, a turbo molecular pump on this region is also used to speed up pump down times. Ultimate chamber pressure in this region is typically $\sim 10^{-4}$ Torr.

2.3.2 The Detector Chamber

The detector chamber consists of the flight tube, μ metal shielding, magnetic bottle solenoid, microchannel plate detector, and phosphor screen. The magnetic bottle technique necessitates two sources of magnetic fields: a high field generated by the rare earth magnets in the trap region and a low field generated by a solenoid in the detector[6]. The flight tube is

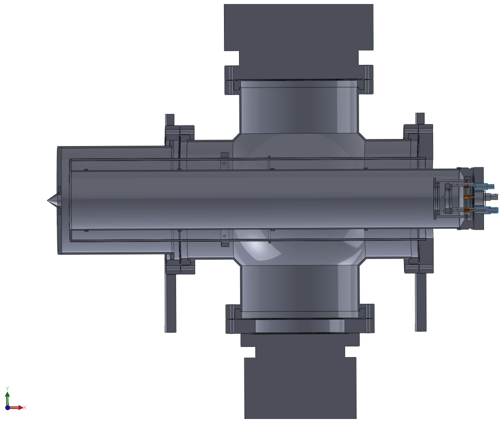

Figure 2.4: Detector Chamber, showing the flight tube with its E shapped cross-section, from the tip of the skimmer left to the detector assembly right.

wrapped by a wire copper wire, which creates the low field. The flight tube is also shielded from stray magnetic fields by a μ metal tube wrapped around the solenoid. At the end of the flight tube is a microchannel plate detector.

The detector chamber has somewhat strange geometry. If the coil were kept under vacuum, gas would be trapped in the coil, which would act as a leak. In order to both bring the start of the coil close to the interaction region and keep the coil at atmosphere, the detector chamber is shaped like a “E” in cross section. The coil for the solenoid rests inside the arms of the E at atmospheric pressure, see Figure 2.4. To allow the coil to be removable, the wire is wrapped around a plastic tube and epoxied in place.

Unlike prior versions of this apparatus[1, 7, 8], the detector region is vented with the trap when the experiment is shut down. The chamber is pumped by three turbomolecular pumps with a combined pumping speed of 1400 L/s. The 450 L/s magnetically levitated turbo has been removed to simplify the interlock system and was replaced by a 150 L/s turbo. No significant change to the ultimate pressure in the detector was observed.

Finally, data are recorded as the capacitively coupled current off of the phosphor screen as a function of time. This analogue signal is collected on an oscilloscope, converted to a digital signal, and saved on the data acquisition computer. A full description of the updated data acquisition code will appear in the upcoming thesis of Holly L. Williams. The phosphor screen allows for alignment of the magnets only. Images are not recorded or used for data collection purposes.

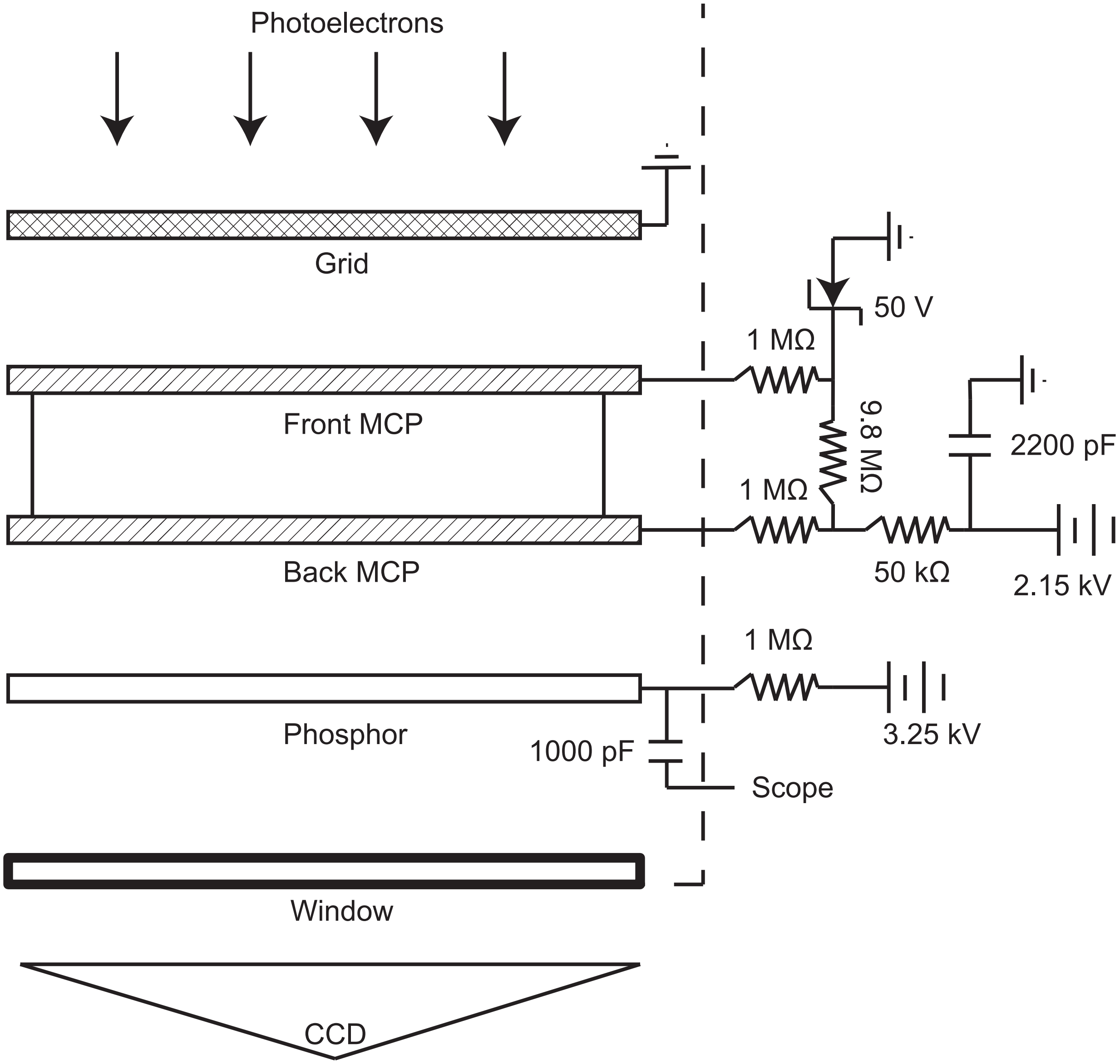

Figure 2.5: Detector Circuit Schematic. The dotted line separates components that are in versus out of vacuum.

2.3.2.1 Detector Circuit

The wiring diagram for the electron detector is based on the circuit from the thesis of Alexandra Weaver[9]. A microchannel plate (MCP) is essentially an electron multiplier[10]. When an electron hits the wall of one of the many channels, an electron cascade is initiated, eventually resulting in a gain of 10^4 electrons/plate. Multiple plates in sequence can be used to substantially increase the total gain. Two are used in the current detector design. The electrons are then accelerated to a phosphor screen on a glass plate. The electrons contain enough energy to excite the phosphor and create an image. While in other experiments this image may be used to provide angular information about the PE spectrum, the image from the screen in this experiment is used only to align the bottle. Photoelectron spectra are generated by recording the current off of the phosphor as a function of time. No obvious improvements were observed by capacitively coupling on the back MCP versus the phosphor screen.

The plates must be held at a bias voltage both to accelerate the electrons to the detector and to replenish electrons accelerated to the detector. The bias voltage is about 1 kV per plate and 3.25 kV for the phosphor. One $M\Omega$ resistors separate the high voltage supplies from the plates to prevent electronic ring in the time of flight spectrum due to impedance mismatch between the high impedance plates and relatively low impedance wire[11]. A grounded nickel mesh grid is placed in front of the detector to prevent the electric field from the plates from affecting the flight of the photoelectrons.

2.3.3 Increased Uptime and Interlock System

Various improvements have been made to allow for near continuous experimental uptime. The 800 milliliter trap can hold up to 48 hours of solution at typical flow rates. Also, an automatic filler for the liquid nitrogen dewar allows for cryogenic pumping for approximately 24 hours without refilling. The interlock system has been updated to assure a safe shut down of the instrument in the event of jet freezing, power outage, or other emergency. Finally, the detector pressures are live fed to a monitoring system, so that the chamber pressure can be monitored remotely via the internet.

The interlock wiring system are based on the original turbomolecular pump interlock diagram from the thesis of Alexandra Weaver[9]. The updated diagram is pictured in Figure 2.6. The interlocks are tripped by a turbo pump failure, high detector foreline pressure, high detector pressure, and building power outage. In the event of a trip, any electronics plugged into the interlock power strip, such as the detector and the syringe pump, will turn off immediately. On a 10 second delay, the foreline valves will close, the solenoid vent valves will open, and all four turbos will be shut down. The secondary vent valves must be opened manually to vent the chamber, so after an interlock trip the chamber will remain at approximately

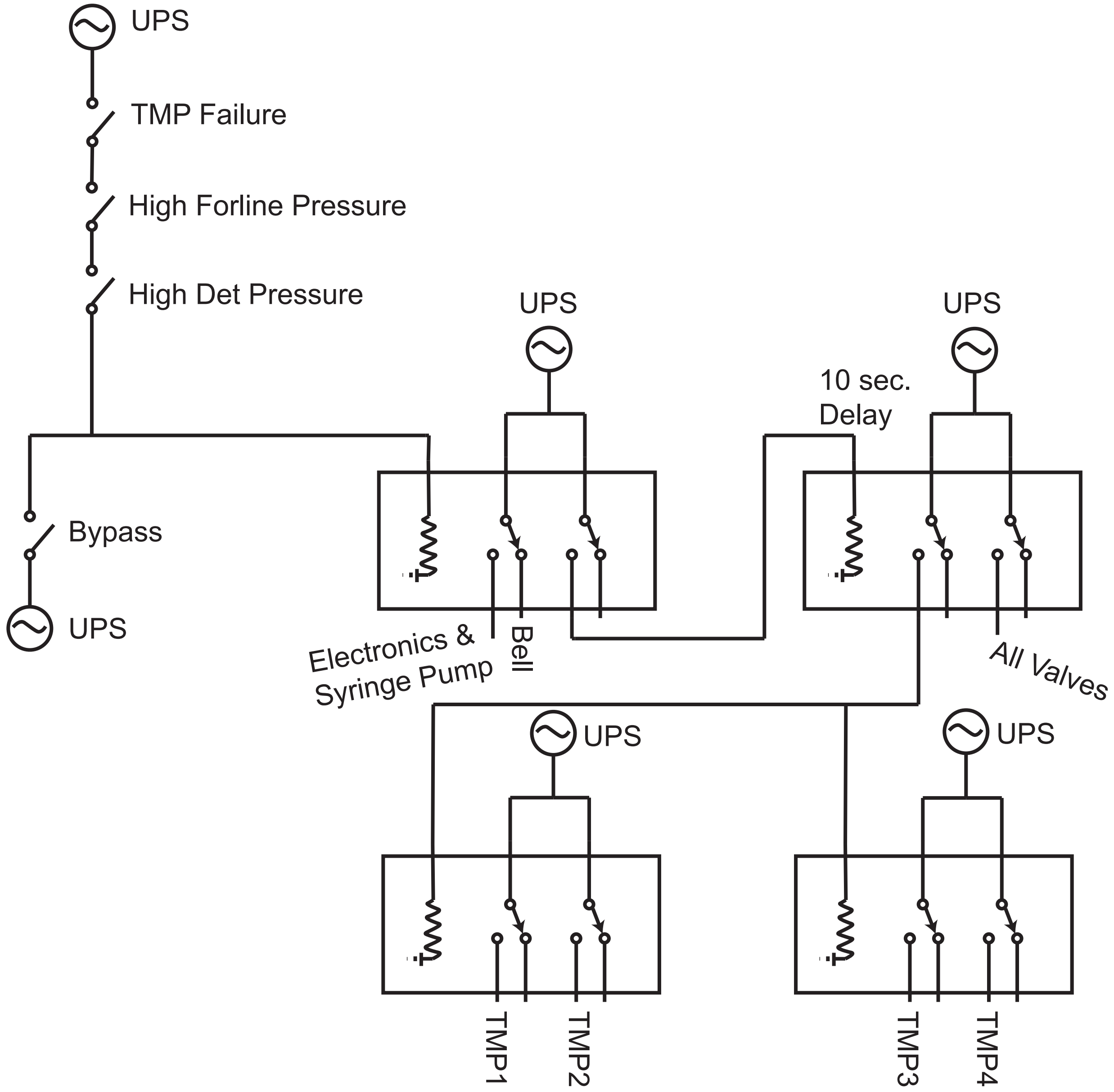

Figure 2.6: Interlock Circuit, based on the original designs from the Anion PES instrument.

10^{-3} Torr.

In the event of a power outage, the ion gauge controller will turn off, and the interlock system will trip. The interlock system is plugged into an uninterruptible power supply (UPS), so in the event of building power ripples or surges, the apparatus will continue to operate. In the event of a black out longer than ten seconds, the interlock system will start instrument shutdown, and eventually, the UPS will run out of power.

The detector pressures are fed to the Watchdog monitoring system via a 2.5 mm audio jack. The analog output from the Granville-Phillips 307 Gauge controller (containing the detector gauges) outputs a 0-10 V potential proportional to the logarithm of the measured pressure. That 10 V output is fed through a voltage divider to the monitoring system, which rescales the potential from 0 - 10 on the online page. The actual pressure is related to the displayed value by the relation below.

$$P = 10^{-(11.5-V)} \tag{2.1}$$

2.4 Time of Flight and Energy Resolution

Photoelectron spectra are generated from the time of flight (TOF) distribution of the photoelectrons on the microchannel plate relative to an external trigger. The Tektronix oscilloscope is triggered by the one kilohertz repetition rate of the amplifier pump laser of the femtosecond system, which is set such that the oscilloscope is triggered shortly ahead of the laser interaction time. The oscilloscope is capable of two nanosecond time bins which are recorded out to two microseconds after the interaction time. The amplitude of the capacitively coupled current off of the phosphor is recorded as voltage as a function of time by the oscilloscope.

Conversion of the raw TOF spectra to electron kinetic energy is quite simple. If the length of the flight tube and the delay between the trigger and interaction time are known, the electron kinetic energy is just the square of the length divided by the square of the time of flight times the mass of an electron divided by two, Equation (2.2). Since typical electron kinetic energies in this experiment are many orders of magnitude faster than the jet flow velocity, a conversion to center of mass coordinates is not necessary, as is used in the Weaver thesis[9]. The length of the flight tube, ℓ, and the time offset, t_o, are the only calibration factors.

$$eKE = \frac{1}{2}m_e v_e^2 = \frac{1}{2}m_e \frac{\ell^2}{(t-t_o)^2} \tag{2.2}$$

In principle, both calibration factors are well known before calibration. The length of the flight tube is 66 cm, and without another rebuild of the instrument, it should not change significantly between calibrations. When the laser arrives at the jet, a significant amount of the laser light is scattered in all directions, some of which goes directly down the flight tube. These scattered photons create a ring on the detector. Since the speed of light in a vacuum is always about a foot per nanosecond and the flight length is about two feet, the ring on the detector is always two nanoseconds after t_o. Since both calibration factors are known, regular calibration is used as a check that the experiment is working and that the laws of physics are not being locally violated.

In energy space, the resolution decreases non-linearly with increasing electron kinetic energy. Since $t \propto eKE^{-1/2}$, as defined in Equation (2.2), whereas $\frac{\Delta eKE}{eKE} = \frac{2\Delta t}{t}$, the energy resolution scales with kinetic energy to the three halves, $\Delta eKE \propto eKE^{3/2}$; therefore, slow electrons are measured with much greater energy resolution than fast electrons. In principle, the resolution of the instrument is given by the time resolution of the oscilloscope. However, in practice, a number of factors can effect the width of the time of flight distribution. For example, the width of the ultrafast, ultraviolet pulses in energy often exceeds the instrumental resolution for the slowest electrons. As an estimate of the best, instrumental TOF resolution, a Xenon photodissociation line at a relatively fast arrival time has an 8 ns full width at half maximum. This is also the full width half maximum of a single dark count. Assuming an 8 ns time of flight resolution, the energy space resolution at 600 ns TOF is 80 meV and at 1000 ns is 20 meV.

The non-linear scaling of energy with time also manifests in the amplitudes of the photoelectron signal. The peak intensities from TOF to eKE space are related by the Jacobian transformation[9].

$$I(eKE) \propto i(t)eKE^{-3/2} \tag{2.3}$$

Because the intensity of the dark counts on the detector is uniform across all time of flight bins, the amplitude of the background noise is amplified at low eKE by the Jacobian. Further, if the baseline is not, on average, zero for the entirety of the photoelectron spectrum, a sloping background can appear in the spectra. This issue is averted by leveling the baseline in TOF in the data processing program prior to Jacobian scaling.

2.5 Magnetic Bottle Technique

The liquid jet photoelectron spectroscopy apparatus underwent a significant rebuild in the Fall of 2012. Central to the design of the new apparatus was the addition of a magnetic bottle. First described by Kruit and Reid[6] and as implemented previously in the Neumark group [12, 13], the magnetic bottle makes the use of an inhomogeneous magnetic field to direct up to 50% of generated photoelectrons to the detector. This was a significant increase in collection efficiency over the original apparatus, which had a collection efficiency of about 0.09%[1].

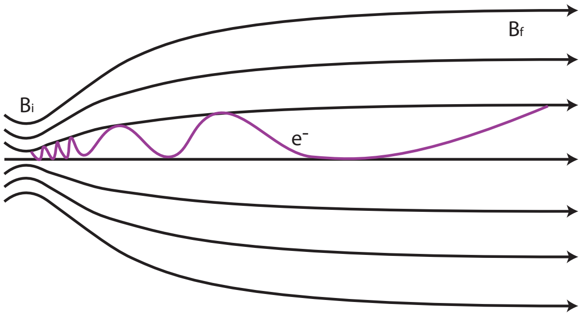

Figure 2.7: Schematic showing the helical trajectory of an electron in the field of the magnetic bottle.

In order to bend the electrons to the detector, a strong magnetic field of ∼1.1 Tesla is generated near the interaction region using a stack of rare earth magnets. A second weak field is generated by a coil of wire wrapped around the flight tube. This creates a uniform 10 Gauss magnetic field along the time of flight axis. The combination of these two sources create a magnetic field shaped like a bottle with the mouth at the interaction region and the bottom of the bottle at the detector.

Without symmetry considerations, generated photoelectrons are emitted in all directions from the interaction point. Since the force on a charged particle in a magnetic field is the cross product of the velocity and the magnetic field, $\vec{F} = q\vec{v} \times \vec{B}$[14], any electrons moving in the same direction as the magnetic field will be unaffected; however, any electrons that are moving at some angle relative to the magnetic field will be bent perpendicularly to the field lines and begin to spiral around the time of flight axis. As the magnitude of the magnetic field gets smaller on the way to the detector, the spiral becomes larger and slower and, to conserve energy, kinetic energy on the TOF axis increases. Because of this variation in field, electrons are bent to the detector. Of the electrons born in the hemisphere nearest the detector, all are eventually collected on the detector even those moving perpendicular to the time of light axis, 50% of generated photoelectrons.

It is important to consider to what extent the strong field effects the time of flight distribution (and thus the resolution) of the photoelectrons. In order to do this, we must take a closer look at the mechanism by which the electrons are bent toward the detector. By setting the Lorentz force equal to the mass times the centripetal acceleration, one arrives at the angular frequency of the spiral, $\omega = qB_i/m_e$, and the cyclotron radius, $r_i = vsin\theta_i/w_i$, where q and m_e are the charge and mass of the electron. By multiplying the two results, the angular momentum is

$$L_i = \frac{m_e^2 v^2 sin^2\theta_i}{qB_i}. \tag{2.4}$$

If the variation of the field in which electron moves changes negligibly over the course of a rotation, (i.e. the electron spirals much faster than it moves along the time of flight axis), then the angular movement can be considered independently of the transverse movement and the quantity above is conserved. Under this assumption, the ratio of the initial to the final angle and radius is given by

$$\frac{r_i}{r_f} = \frac{sin\theta_f}{sin\theta_i} = \left(\frac{B_f}{B_i}\right)^{1/2}. \tag{2.5}$$

By this relation, if the initial field is greater than the final field, the angle of the electron relative to the time of flight axis must become smaller and the radius of rotation must become larger. This results in a bending of off-axis electrons to the detector and a magnification of the electron spot size on the phosphor screen, which we will return to later[6].

It should also be apparent that the larger that B_i is relative to B_f, the better the assumption that the rotational angular momentum is conserved will be. So-called "non-adiabatic" effects will occur when this assumption does not hold and will result in broadening of the TOF distribution. While the effective time of flight considering non-adiabatic effects is not quite a pencil-and-paper problem, numerical simulation using similar fields for a 1 eV electron yields a fundamental limit of $\frac{\Delta t}{t} = 0.56\%$ for an isotropic distribution and 0.17% and 0.89% for parallel and perpendicular type transitions respectively[6]. In practice, again looking at photoionization of Xenon, no significant change in the time of flight resolution was observed with the new instrument.

Since the liquid jet is about 20 μm in diameter, we can assume that the initial cloud of photoelectrons is approximately this size. Using Equation (2.5) and the 1.1 T and 10 G field strengths for our bottle, the expected magnification of the photoelectron cloud is about a factor of 30, a spot size of 0.6 mm on the detector. Since this spot size is on the same order as the size of the skimmer, alignment of the steering magnets is crucial.

2.5.1 Bottle Operating Notes

The solenoid in the magnetic bottle is 26" long and consists of 14 gauge copper wire wrapped at 10 turns per inch. The field inside the solenoid can be found using the equation below:

$$B = \mu nl. \tag{2.6}$$

A Kepco high current power supply is used to supply a current of 1.5 Amps and a voltage drop of 1.5 Volts. This maintains a predicted magnetic field of ~10 Gauss. Data are collected from a chevron stack microchannel plate (MCP) imaging system (Beam Imaging Solutions, BOS-25-IDA-CH-MS). The operating voltage drop across both plates is 2.15 kV yeilding 8 mV of dark counts a full width at half maximum of 8 ns. The detector did have a "burn-in" period. Over the course of the first year, the operating voltage was raised from 2.00 kV to

2.15 kV. The phosphor screen is operated at a voltage of 3.25 kV. In the current detector circuit, the phosphor screen is used both for alignment of the bottle and as an anode from which the capcitively coupled current is measured.

Alignment of the magnetic bottle greatly effects the signal intensity on the detector. The final magnification of the electron cloud from the magnetic bottle is about 400 μm, a factor of twenty, which is very near the size of the 900 μm skimmer. The position of the rare-earth magnets is controlled by a set of picomotor actuators on a 3-axis translation stage. The picomotors are peizo driven and have a minimum step size of 30 nm. The magnet is typically moved in 30 μm steps until the signal, as viewed on an oscilloscope, is highest. The bottle can also be aligned by looking at the image created by the photoelectrons on the phosphor screen. Typically the bias voltage is turned up about 200 V. Then, the stages can be moved until the spot is brightest and smallest. Poor alignment manifests as a dim asymmetric spot on the phosphor.

2.6 Calibration

Calibration of the instrument is performed by three photon photoionization of Xenon atoms. Xenon is pumped into the chamber through a 100 μm gas inlet near the skimmer. Using the second-harmonic sum-frequency signal (SH-SFS) from the TOPAS, we are able to generate 2-5 μJoules of 238-255 nm light, which is used to ionize the Xenon to its $^2P_{1/2}$ and $^2P_{3/2}$ state per the relation below. Using three photons of UV, this gives photoelectron kinetic energies of 1-3 eV.

$$Xe \xrightarrow{h\nu} Xe^+_{^2P_{1/2},^2P_{3/2}} + e^- \tag{2.7}$$

The calibration scheme used for the project has changed somewhat since last described[1, 7, 8]. Originally, Xe and Ar were multiphoton ionized with a single laser wavelength yielding a four point fit. More recently, the tunable UV output fromSH-SFS of the TOPAS has been used to detach Xe alone at 4 to 6 wavelengths creating an 8-12 point fit. This change was motivated by several reasons. First, the tunable UV power was low before the addition of the new femtosecond system, so usable wavelengths were the 266 nm third harmonic of the ultrafast laser or 248.6 nm, a [1+2] resonant photodissociation. Second, the three photon photodetachment cross section for Xenon is much larger than the four photon cross section of Argon.

As with the liquid jet, the Xenon atoms have negligible velocity in the lab frame; therefore, we consider the lab frame velocity to be the photodetachment velocity and neglect to change to center of mass coordinates. The expected velocity of the photelectrons at a known laser wavelength and binding energy is given by the kinetic energy using the equation below. The factor of three is due to the number of photons in the ionization process.

$$v_{known} = \sqrt{\frac{2}{m_e}(3h\nu - eBE)} \tag{2.8}$$

This must also be equal to the length of the flight tube divided by the time of flight relative to the trigger time, t_o, per Equation (2.2). By setting the two formulae for velocity equal to each other and rearranging, one arrives at the following:

$$t = \frac{\ell}{\sqrt{\frac{2}{m_e}(3h\nu_i - eBE)}} + t_o \tag{2.9}$$

By plotting $1/v$ versus time of flight for all laser wavelengths, a straight line can be fit to the calibration points. The slope of that line is the flight tube length, ℓ, and the intercept is time offset due to the delay between the trigger and the time of interaction, t_o. As was mentioned by A. T. Shreve in his thesis[1], the wavelength from the TOPAS and the femtosecond system may change based on the alignment. The wavelenth used for ν_i is measured on a spectrometer. The spectrometer is calibrated on the mercury emission lines with a mercury lamp. The calibrated wavelength is good to the nearest tenth of a nanometer.

The Xenon inlet has changed significantly since the commissioning of the new instrument. A quarter inch stainless steal tube is brought into the bottom of the trap region on an UltraTorr feed through. This is connected to a 1/16" stainless steal pipe connected to an effusive jet nozzle with a 100 μm orifice with the same general design as the liquid jet. Typical pressure in the Trap region while the Xenon jet is running is 10^{-4} Torr. The alignment of the jet nozzle is quite sensitive and must be checked regularly.

2.7 Streaming Potentials

When an electrolyte flows through a tube, electrokinetic charging of the liquid occurs. These streaming currents are generated by charge separation at the liquid-capillary interface. On the glass surface, ions are adsorbed onto the glass subject to the chemical interaction of the ion with the surface, which nucleates an electrical double layer. The current generated is due to the radial variation in flow velocity inside the tube. At the surface of the tube, the liquid flow velocity is slow, whereas in the center of the tube the flow velocity is high. The result is a steady stream of charged ions near the interface flowing past the double layer, which gives rise to a net charge flow within the jet[15–18].

The magnitude and sign of potential driven by the streaming current can vary wildly based on the liquid, ion concentration, flow velocity, and diameter of the jet[15]. Typically streaming currents can be reduced by running at low backing pressure, with relatively high salt concentrations, and with very thin jets[19–21]. Even by taking these precautions, the effect of the streaming potential generated by the liquid jets has a measurable impact on the

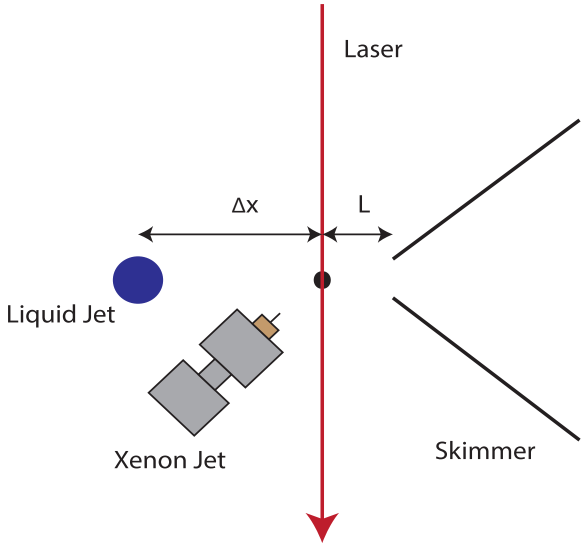

Figure 2.8: Schematic showing the interaction region for a streaming potential measurement. The distance, Δx, between the liquid jet and the interaction point between the laser and the calibration gas is systematically varied and a photoelectron spectrum is taken at each distance.

electron kinetic energy and must be accounted for[7, 22, 23].

Measurement of the microjet streaming potential is a part of a normal calibration procedure. Using the Xenon inlet described in the previous section, it is possible to take Xenon photoionization data in the field of the liquid jet. At a single jet position between the Xenon/laser interaction region, generated photoelectron will slow down or speed up in the field generated by the jet, depending upon the sign of the streaming potential. The change in the kinetic energy of the photoelectrons as a function of jet distance, Δx, is of the form below. This particular functional form is an approximation of the potential due to an infinite line of charge, here, the jet[22, 23].

$$eKE_{meas} = eKE_{field-free} - \frac{L\Phi}{L + \Delta x} \tag{2.10}$$

In this relation, L is the distance between the laser and the skimmer, typically 1 mm, and is considered to be a known quantity. The streaming potential, Φ, is determined from a fit of the function above to a plot of the measured Xe $^2P_{3/2}$ kinetic energy versus jet position. The field free kinetic energy (i.e. with the jet off) is measured during calibration but is used as a fit parameter to check the quality of the fit. A streaming potential measurement is typically taken after the completion of data collection due to difficulties getting the jet to stop and restart. For the experiments presented here, streaming potentials were largely constant of the course of the day; however, live measurement of the streaming potential during data collection would be a major experimental improvement.

2.8 Summary of Changes to Shreve's Drawings

Several changes were made to the vacuum chamber during construction. First, the differential pumping sheath (Fig. B17 p. 106, [1]) was delivered with clearance holes rather than taps on the 10" CF flange. Because of this error, the detector chamber cannot be removed without also removing the sheath and resetting both CF flanges.

Next, the original designs have two different mounting schemes for the grid for the electron detector. During construction, we elected to not use the Kimball-Physics groove grabber system in Fig.s B24-B26[1] but, rather, the "alternate" mounting system shown in Fig. B41[1]. The grid support plate is separated from the detector by insulating spacers and hard grounded to the chamber through the stainless steel screw which attaches it to the detector flange.

The 4.5" CF tee, which houses the "ice breaker", in the original design has also been removed. The enlarged opening for the liquid nitrogen trap allows for a larger solid angle of jet to reach to cold surface of the trap, which has had the effect of greatly reducing the number of jets that freeze up from the bottom of the chamber. The entire ice breaking assembly (part 43) has been removed to making cleaning simpler.

Finally, the largest change to the chamber has been the complete overhaul of the magnet alignment hardware. The flexible drive shafts called for in the original design to turn the alignment screws on the 3-axis translation stage were over their max bend specification and would twist together when the rotary feedthrough was turned. In total, parts 21, 33, 34, 37, 38, and 40 in Figure B.4[1] have all been removed. The new magnet alignment system consists of three picomotor actuators used in place of micrometers in a larger 3-axis stage assembly. Power for the motors is supplied through a four BNC port 2 3/4" CF flange, which replaces the multiplexer (part 21). The motors are controlled through a LabView program on the data acquisition computer.

2.9 Practical Considerations of Ultrafast Spectroscopy

In 2010, the Liquid Photoelectron Spectroscopy project was revamped as the Time-Resolved Liquid Photoelectron Spectroscopy project through the addition of an ultrafast laser. The original ultrafast laser was a Clark-MXR CPA-1000, model year 1998. As one of the first commercial ultrafast systems, this model was once quite revolutionary; however, due to the stability requirements necessary for time-resolved measurements on liquids, this laser system proved to be quite useless for measuring anything other than a streaming potential. In Spring 2012, a new laser system, a Spectra-Physics Spitfire, was gratefully stolen from the Leone Group and replaced the original Clark System. The Spitfire amplifier combined with a Tsunami oscillator regularly create 2.1 mJ pulses at a kilohertz repitition rate with sub 75 fs pulse duration.

A pump-probe experiment requires at minimum two laser pulses and some way of delaying one relative to the other. Splitting laser the beam is trivial. A kind of mirror, aptly called a beam-splitter, is placed in the beam which partially reflects a fraction of the beam and transmits the rest. Creating an optical delay is also not particularly difficult. The speed of light is about a foot per nanosecond or, alternatively, 3.3 femtoseconds per micron. Tunable delays between two ultrafast pulses can be generated by making one pulse travel a longer distance than the other. Typically, this is done by putting one beam on a motorized stage and leaving the other fixed. Our stage is one nanosecond long; therefore, the longest time measurable with this stage is one nanosecond. Then, in this particular experiment, both beams are recombined colinearly with a second beam splitter are run colinearly to the spectrometer. Of course, other higher-order flavors of pump-probe spectroscopy can be done with more complicated pulse trains and non-colinear geometries, which are not discussed here.

2.9.1 Generating a Femtosecond Pulse

The ultrafast pulses for this experiment are generated via a four stage process. Ultrafast pulses are generated in the oscillator through an optical phenomenon called mode-locking. The low power pulses are then temporally stretched. After which the pulses are amplified and then re-compressed. Stretching reduces the peak power of the pulse during the amplification stage. This allows for a much greater amplification without burning the gain medium or other optical components inside the amplifier. The process is called Chirped Pulse Amplification (CPA). Further reading and more complete coverage of ultrafast fundamentals is provided in the texts of Rulliere[24] and Boyd[25].

An ultrafast oscillator is a mode-locked laser, meaning that the longitudinal modes of the cavity are in phase. Conceptually, one can think about a sum of standing waves in the optical cavity, where each wave is an allowed resonator mode with a slightly different frequency. If the waves are all in phase, they constructively interfere on some characteristic frequency creating a pulse train. The width of this pulse train is governed by the number and bandwidth of modes in phase in the cavity. In an ultrafast oscillator, this effect is induced by bumping an optical element within the cavity. This creates a local intensity maximum which bounces between the end mirrors. For this reason, the repetition rate of passively mode locked ultrafast oscillator is always twice the cavity length divided by the speed of light.

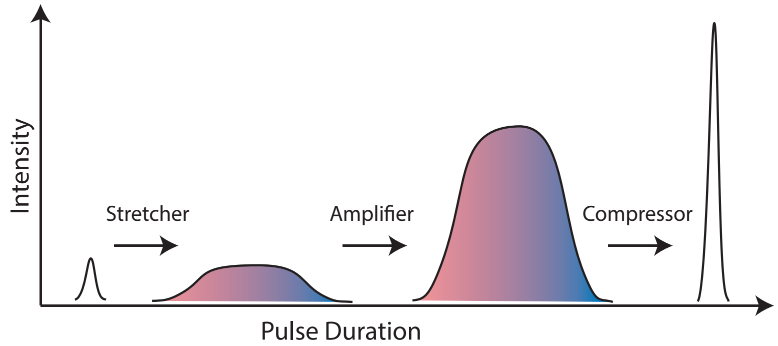

Figure 2.9: Chirped Pulse Amplification: A low-power high repetition rate femtosecond pulse is first temporally steched, then amplified, then compressed.

In a Kerr lens mode locked oscillator, the local intensity maximum created in the cavity is amplified on every pass. In a Kerr Lens active medium, such as Ti:Sapph, the lasing medium acts as a lens. The higher the power of the driving field, the tighter the induced focus. This focusing raises the energy density in the medium and drives up the Einstein B coefficient. In this manner, even with a continuous wave pump laser, pulsed operation is amplified over continuous operation. The result is nanoJoule, 100 megaHertz pulses with femtosecond pulse duration.

The pulse from the oscillator is “chirped” to stretch it before amplification. Then, the low power beam is used as a “seed” for a secondary gain medium. A temporally, chirped pulse has a variation in the optical frequency of the pulse as a function of time. Chirp can be induced such that bluer wavelengths arrive earlier than redder wavelengths or vice versa. Spatial chirp can also occur. In the case of spatial chirp, part of the transverse mode of the laser is a different color than the rest; for example, the top of the laser spot might be bluer than the bottom. This phenomena is generally avoided.

In the stretcher, the pulse is stretched in time to a duration of about 100 picoseconds. This is achieved by making the blue edge of the frequency spectrum travel a longer path through the stretcher relative to the red. While stretchers can be made with prisms, reflective gratings, or even transmission gratings, the stretcher in the Spitfire makes use of a reflection grating. Rather than using many gratings, the beam is reflected back onto the same grating four times in order to reduce cost and save space. This involves folding the beam between the grating, a parabolic mirror, and a zero-degree incidence mirror. The focus of the parabolic mirror is located at the face of the 0° mirror. This helps reduce any spatial chirp of the beam due to the wavefront tilt induced by angling the beam up over the grating.

The stretched beam is then directed into the path of a second gain medium. The Spitfire has a two stage amplification system which comprises of a regenerative amplifier (regen) and a two-pass “ring” amplifier. Without the seed, the regenerative amplifier is a laser in and of itself; therefore, with wide Pockels cell timing and without the seed, the regen cavity will lase. The stretched beam from the oscillator acts as a “seed”. When placed in the lasing cavity of the regen, the seed beam stimulates the cavity to lase with the same characteristics itself. In this manner, with every pass in the regen, the seed gets amplified with little loss in spectral bandwidth.

The optical cavity of the regen is formed by two end mirrors with a Ti:Sapph crystal in the middle. Both amplifier arms are pumped by the same Nd:YLF laser (Photonics Industries DM-30), which is split using a wave plate and a polarizer. The power on each of the various lines can be adjusted by changing the angle of the wave plate. Cavity seeding and dumping is accomplished by two Pockels cells, a wave plate, and a thin film polarizer.

The Pockels cells act like optical switches. Depending on the voltage and the alignment of the cell, the cell can act like a half wave plate, a quarter wave plate, or a window. Pulses enter and exit the regen with vertical polarization, and they lase with horizontal polarization. When the first pockels cell is fired, vertically polarized pulses are rotated to horizontal and allowed into the cavity. When the second pockels cell is fired horizontal pulses are rotated to vertical and are picked off by the polarizer. The time delay between the pockels cell firing dictates the number of passes in the cavity. This delay is chosen such pulses are picked just after the maximum of the gain curve.

The second stage amplifier is substantially simpler. The beam from the amplifier is routed through a two pass loop-d-loop through a third Ti:Sapph crystal. On each pass through the crystal, the intensity increases. The crystal is pumped by the vertically polarized portion of the green pump beam from the entrance polarizer. From here, the beam is expanded (to prevent burning of the optical components) and the polarization is rotated back to horizontal on a periscope (for convenience).

Similar to the stretcher, the compressor also consists of four passes on a single grating; however, rather than tilting the beam up and down, two 90° retro reflectors are used to fold the beam back onto the grating. One retro reflector is placed on a stage so that the induced chirp can be tuned. The angle of the grating in the compressor should have the same angle as in the stretcher. This angle can be fined tuned using a FROG to achieve the best possible compression.

2.9.2 Ultrafast Pulse Characterization

There are countless ways in which an ultrafast pulse can be distorted or destroyed. Residual chirp in the pulse will change the zero overlap time as a function of wavelength yielding diagonals in TRPES traces. A long pulse length reduces the time resolution of the experiment. The central wavelength of the output beam can be changed by the alignment and change

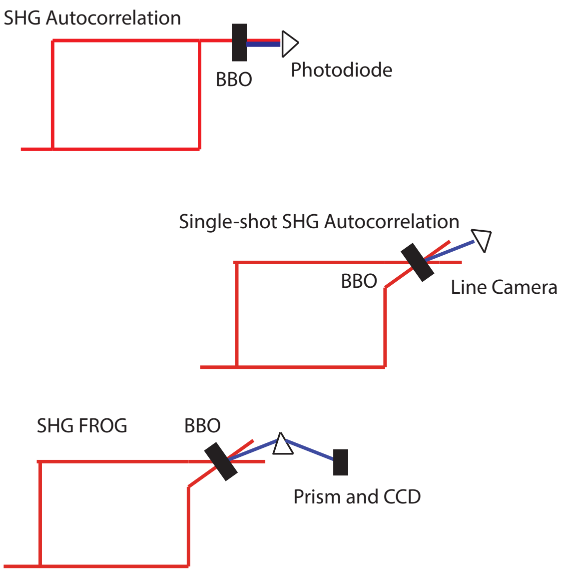

Figure 2.10: Three beam geometries for pulse characterization. Top: second harmonic generation autocorrelation in which the SHG intensity is monitored as a function of the distance in path length between one arm of the interferometer and another. Middle: Single shot autocorrelation in which delay in the interferometer need not be adjusted. Bottom: SHG FROG in which the frequency spectrum of the pulse is measured as a function of optical delay.

the wavelength of the photodetachment pulse, which makes the electrons look more or less tightly bound. Therefore, it is very important to have an accurate understanding of the characteristics of the pulse. There are two ways in which we do this: FROG and cross-correlation. While cross-correlation only allows for the measurement of the intensity envelope of the pulse with time, FROG allows significantly more detailed pulse characterization. In a cross-correlation, a mixing process such as sum-frequency generation for two differently colored beams is performed, usually in a BBO. The third color generated from the crystal is placed on a photodiode, and one color is optically delayed relative to the other before being recombined colinearly. The resultant intensity as a function of time is a convolution of the intensity trace of one pulse relative to the other. The gaussian width of the cross-correlation is related to the width of both pulses by the relation:

$$\sigma_{xcorr}^2 = \sigma_1^2 + \sigma_2^2. \tag{2.11}$$

If both beams are the same color, this process is called an autocorrelation, and the gaussian width of the pulse is the width of the autocorrelation divided by the square root of two. The gaussian width and the full width at half maximum (FWHM) of the pulse are strictly different: $FWHM = 2\sqrt{2ln(2)}\sigma_{xcorr}$.

Frequency-resolved optical gating (FROG) is a variant on the setup above except the beams are recombined non-colinearly. The mixed frequency is generated bisecting the angle of the two beams and is imaged on a spectrometer as a function of delay. The change in the spectrum as a function of delay allows for retrieval of residual chirp, reconstruction of the wavelength and time dependent phase, and of course the temporal duration of the pulse.

The width of the ultrafast pulse governs the time resolution of the instrument. The cross-correlation at the chamber is a measure of the instrument response function. This instrument response function is in turn convoluted with any dynamics that might be observed in the experiment. If the decay dynamics occur on the same time scale as the width of the response function, it may be difficult to extract an accurate lifetime. A good Gaussian width for the 800 nm + 266 nm cross-correlation outside of the chamber is 70 fs.

2.10 References

[1] A. T. Shreve, *Photoelectron Spectroscopy of Solvated Electrons in Liquid Microjets*, Thesis, UC Berkeley (2012).

[2] T. A. Yen, *Anion Photoelectron Spectroscopy of Exotic Species*, Thesis, UC Berkeley (2010).

[3] A. Stolow, A. E. Bragg, and D. M. Neumark, Chem. Rev. **104**, 1719 (2004).

[4] T. Suzuki, Int. Rev. Phys. Chem. **31**, 265 (2012).

[5] M. Faubel, S. Schlemmer, and J. P. Toennies, Zeitschrift Fur Physik D **10**, 269 (1988).

[6] P. Kruit and F. H. Read, Journal of Physics E: Scientific Instruments **16**, 313 (1983).

[7] A. T. Shreve, M. H. Elkins, and D. M. Neumark, Chemical Science **4**, 1633 (2013).

[8] A. T. Shreve, T. A. Yen, and D. M. Neumark, Chem. Phys. Lett. **493**, 216 (2010).

[9] A. Weaver, *Spectroscopy of Transient Neutral Species Via Negative Ion Photoelectron Spectroscopy*, Thesis, UC Berkeley (1991).

[10] J. H. Moore, C. C. Davis, and M. A. Coplan, *Building Scientific Apparatus*, 4th ed. (Cambridge University Press, 2009).

[11] P. Horowitz and W. Hill, *The Art of Electronics*, 3rd ed. (Cambridge University Press, 2015).

[12] H. Gomez, *Anion Photoelectron Spectroscopy of Semiconductor Clusters and Solvated Species*, Thesis, UC Berkeley (2002).

[13] B. J. Greenblatt, *Femtosecond Photoelectron Spectroscopy: A New Tool for the Study of Anion Dynamics*, Thesis, UC Berkeley (1999).

[14] J. D. Jackson, *Classical Electrodynamics*, 3rd ed. (Wiley, 1998).

[15] M. Faubel, B. Steiner, and J. P. Toennies, J. Chem. Phys. **106**, 9013 (1997).

[16] M. Faubel and B. Steiner, Berichte Der Bunsen-Gesellschaft-Physical Chemistry Chemical Physics **96**, 1167 (1992).

[17] W. L. Holstein, L. J. Hayes, E. M. C. Robinson, G. S. Laurence, and M. A. Buntine, J. Phys. Chem. B **103**, 3035 (1999).

[18] A. M. Duffin and R. J. Saykally, Journal of Physical Chemistry C **112**, 17018 (2008).

[19] F. H. J. van der Heyden, D. Stein, and C. Dekker, Phys. Rev. Lett. **95**, 116104 (2005).

[20] F. H. J. van der Heyden, D. J. Bonthuis, D. Stein, C. Meyer, and C. Dekker, Nano Lett. **6**, 2232 (2006).

[21] A. M. Duffin and R. J. Saykally, Journal of Physical Chemistry C **111**, 12031 (2007).

[22] Y. Tang, Y.-i. Suzuki, H. Shen, K. Sekiguchi, N. Kurahashi, K. Nishizawa, P. Zuo, and T. Suzuki, Chem. Phys. Lett. **494**, 111 (2010).

[23] F. Buchner, A. Lübcke, N. Heine, and T. Schultz, Rev. Sci. Instrum. **81**, 113107 (2010).

[24] C. Rullière, ed., *Femtosecond Laser Pulses: Principles and Experiments*, 2nd ed. (Springer, 2004).

[25] R. W. Boyd, *Nonlinear Optics*, 3rd ed. (Academic Press, 2008).

Chapter 3

Analysis of Time-Resolved Data

*Portions of this chapter published as Elkins, M. H., Williams, H. W., Neumark, D. M., Dynamics of Electron Solvation in Methanol: Excited State Relaxation and Generation by Charge Transfer to Solvent, Journal of Chemical Physics, **142**, 234501, (2015). Reproduced with permission.*

The following chapter details the methods by which raw data files are post-processed before analysis and the global fitting routines used to analyze data in Chapters 4 through 7. Post-processing of the raw data files includes: background subtraction, baseline correction, rebinning, and conversion from time of flight to eKE space. The time-resolved data analysis section details: an estimate of a reasonable number of kinetic components using singular value decomposition, the implementation of global lifetime analysis used in Chapters 5 to 7, and a global fitting routine that allows for spectral shifts used to analyze the two pulse methanol data in Chapter 5. All code referred to in this section are included in Appendix D.

3.1 Post-processing of Time-Resolved Data

The raw data files from the data acquisition program are saved in two forms: the "combinedsums" file and as a set of files at individual optical delays. The combined sums file contains summed signal intensities over all laser shots as a function of time of flight and optical delay (stage position). The current implementation of the data acquisition code calls for the entire set of stage positions to be cycled through before a background scan is taken, which equates to a couple minutes of real time. Since it may be necessary in some cases to remove individual scans, the data for each optical delay are saved in the individual delay files.

The post-processing code is shown in Appendix D. This code makes use of the combined-sums file output from the data analysis code and the "config table" which contains the stage positions. There are typically two ways in which background spectra are subtracted: either with and without the pump beam or by subtraction of the the individual one color spectra. In the first line of code, it is necessary to specify how many background scans were taken. The header of the code also contains the last used set of calibration constants, see Section 2.6, which must be entered manually. The values "tau", "IRFFWHM", and "fig", defined in Section 3.3.3, contain initial values for the global fitting code, which can be changed as necessary.

Most often the spectral features that we are interested in measuring are those that change with delay between the various individual laser pulses. However, each individual laser may generate photoelectron signal. These "one-color" photoelectron spectra do not change with delay and are most often subtracted from the photoelectron spectrum. Even at photon energies less than 100 nanoJoules per pulse, very intense one-color signal may generated from two and higher photon processes. The first step in the post-processing code is to subtract these background spectra.

The background spectra are saved in the final columns of the combined sums file, as if they were the last stage positions. The code takes the specified number of background scans, adds them together, and then creates a matrix the length of the number of delays in the config table and subtracts this matrix from the rest of the data matrix.

After background subtraction, the baseline must be leveled. The oscilloscope constantly updates where the zero volt level is defined. For very low voltage measurements, this continually varying voltage offset is a large source of baseline fluctuation and prevents the use of a static "discrimination" level within the data acquisition software. It has been the practice to set the baseline level negative enough such that the PE signal is never clipped negatively by the scope. In the post-processing phase, a zero-slope line is fit to the baseline, and the fitted intercept is then subtracted from the total PE signal.

In the code, this is implemented by a user prompt, which ask the user which delay should be used for baseline leveling. This should be a delay in which very little signal is expected, usually a very negative or very positive delay depending on the system. The data at that delay are then plotted, and the user is prompted with the option to exclude some time of flight range. This allows the baseline to be releveled even if there is still some data in that particular delay.

Next, the data are converted to eKE using the appropriate Jacobian transformation, see Section 2.4. Finally, the photoelectron spectrum is rebinned to 10 ns bins. The maximum resolution, as determined by the width of our dark counts, is 8 ns; however, fit errors on our 800 meV wide photoelectron spectra may be as large as 100 meV, which is up to 30 ns, depending on the energy lane. The effect here is to both adjacent-average smooth the data and reduce the size of the data matrix for global fitting of the time-resolved data.

3.2 Singular Value Decomposition

Singular value decomposition (SVD) is a powerful tool for analyzing large data sets[1, 2]. True integration of this technique into the data analysis has not yet been fully developed. It is relevant to this thesis only as a way of defining what “a minimal basis of kinetic components” means in the next section on global lifetime analysis. The simplest implementation of SVD is as an estimation of how many distinct parts of the dataset are changing.

SVD is a type of matrix decomposition of the form below. If Data is an m by n matrix, U is an n by n matrix of basis vectors in the row space of Data, and V is an m by m matrix in the column space of Data. If Data is energy versus time, as in all data presented here, then U is an orthogonal basis in energy and V is an orthogonal basis in time. S is the m by n matrix of singular values. S is diagonal but not normal, so the singular values are not strictly eigenvalues. Instead, they can be thought of as amplitudes of the various components.

$$Data = [U][S][V]^* \tag{3.1}$$

There are as many values in S as there are dimensions in m or n (which ever is smaller); however, the magnitude of the singular values rapidly decreases going down the diagonal. The dimensionality of the problem can be reduced by discarding the small singular values, which are interpreted as noise. This is a common technique for noise reduction in digital signal processing. In most instances, it is quite obvious when amplitudes of the singular values drop off. In excited state data in the various solvents, only three singular values are significantly non-zero: one constant time part, one rapidly varying, and one slowly varying. When the difference spectra are analyzed, the constant time portion (the ground state) is no longer present, and the dimensionality is further reduced to just two.

SVD is a spectral decomposition method by itself. Analysis of the basis vectors in U and V give insight into the various spectral and temporal components without making any assumptions about the nature of the data set. The generality of the method is its strength but also its fault. An orthogonal basis in time or energy may not the basis that gives the most chemical insight. As a chemist, it is necessary to decide if the kinetics should be fit by exponentials, or the spectral components by Gaussians, or the entire data set by a kinetic mechanism.

3.3 Global Lifetime Analysis

Global lifetime analysis (GLA) is used extensively in this work to separate spectral contributions with differing dynamics but which have significant spectral overlap. This method allows for simultaneous fitting of the entire data set rather than integrating the intensity in specific energy lanes. GLA is predicated on two assumptions: first, that the spectral and temporal components of the spectra are separable and, second, that the dynamics can be accurately modeled by sums of exponentials. [3, 4]. If both assumptions are valid, the data can be represented by sums of exponentials scaled by a constant which depends on energy called the decay associated spectrum (DAS). The assumption of seperability breaks down in the case of spectra that shift on the same time scale as they decay, which makes the DAS markedly more difficult to analyze[5]. A general description of GLA, the generation of DAS, and the relation of the DAS to the species associated spectra (SAS) is presented using the three-pulse methanol data as an example[6].

3.3.1 General Ideas and Assumptions

First, it is assumed that each spectral component is separable into two parts: one which depends only on energy, $S_j(eKE)$, and the other which depends only on pump-probe delay, $S_j(\Delta t)$. Physically, this means that the spectra do not shift on the same timescale over which they change in intensity. This idea is expressed mathematically below, where sigma is the relative photodetachment cross section, :

$$S(eKE, \Delta t) = \sum_{j=1}^{n} \sigma_r S_j(eKE) S_j(\Delta t) \tag{3.2}$$

Second, it is assumed that the data obeys exponential kinetics. The intensity of the features as a function of time then behave as sums of exponentials (Ex: $[A(t)] = Ae^{-k_1 t} - Be^{-k_2 t}$). Based on this assumption, the data can be represented as sums of mono-exponentials (convoluted with the instrument response function, $L(z - \Delta t)$) with coefficients that depend on energy. The coefficients, $DAS_{\tau_i}(eKE)$, are the decay associated spectra (DAS).

$$S(eKE, \Delta t) = \sum_{i=1}^{m} DAS_{\tau_i}(eKE)[e^{z/\tau_i} \cdot L(z - \Delta t)](\Delta t) \tag{3.3}$$

The DAS are quite different from the $S_j(eKE)$'s, the fixed delay spectra of the species of interest. The DAS merely gives the scale of the coefficient in front of a particular exponential in the sum at a particular energy.

Finally, given these assumptions, one can globally fit the data to equation (3.3) using a nonlinear least squares fitting routine. The optimized parameters are the rate constants, the amplitudes $DAS_i(eKE)$, time zero, the width of the cross correlation and a static offset. Care must be taken to assure that the data are fit with a minimum number of kinetic components.

3.3.2 Kinetic Analysis and Species Associated Spectra

Notice that at this point no kinetic mechanism has been assumed. While many systems can be quite complicated, the DAS for each component must be consistent with any kinetic model that is put forward. To generate $S_j(eKE)$ from the DAS, one must first assume a kinetic mechanism, for instance, $I \xrightarrow{\tau_1} II \xrightarrow{\tau_2} III$ with initial condition $I + II + III = 0$, shown below.

$$S_I(\Delta t) = I_0 e^{-k_1 t} \tag{3.4}$$

$$S_{II}(\Delta t) = \frac{I_0 k_1}{k_1 - k_2}[e^{-k_2 t} - e^{-k_1 t}] \tag{3.5}$$

$$S_{III}(\Delta t) = \frac{I_0}{k_1 - k_2}[k_2 e^{-k_1 t} - k_1 e^{-k_2 t}] \tag{3.6}$$

The kinetic equations describing each state are then substituted for $S_i(\Delta t)$ and eqn. (3.2) is set equal to eqn. (3.3). The DAS can then be solved for as a function of $S_j(eKE)$. The result is below.

$$DAS_{\tau_1} = S_I(eKE) - \frac{k_1}{k_1 - k_2}\sigma_{r,II} S_{II}(eKE) + \frac{k_2}{k_1 - k_2}\sigma_{r,III} S_{III}(eKE) \tag{3.7}$$

$$DAS_{\tau_2} = \frac{k_1}{k_1 - k_2}\sigma_{r,II} S_{II}(eKE) - \frac{k_1}{k_1 - k_2}\sigma_{r,III} S_{III}(eKE) \tag{3.8}$$

Note that the intensity of each DAS has the same sign as the coefficient in front of the exponential in the corresponding kinetic equation. The sign of each part in the sum determines the sign of the shape of the DAS. Since the decay associated spectra are known from the fit, a known spectrum for S_{III} can be used to calculate S_I and S_{II}.

3.3.3 The GLA Code in Several Steps:

The copy of the code included in Appendix D is a general Global Lifetime Analysis treatment which allows for kinetic components going in both the positive and negative decay directions.

This particular feature may be necessary in the case that there are dynamics from the probe coming before the pump, the pump before the probe, or when the pump and probe beam are the same color, a degenerate experiment. The current implementation of the code is an adaptation of the work from Adam Chatterly's thesis [7].

The super structure of the code consists of the main function file, "DegenGlobalFit", and the fitting function files. The inner fitting function file, "GeneratePES", contains the convolution of a single kinetic rate component with the instrument response function. This is called by the outer fitting function, "GenerateTRPES", which takes DAS for one kinetic component from the inner file and creates a matrix with as many kinetic components as specified to fit the entire time-resolved spectrum. The main function file calls the nonlinear least squares fitting routine in Matlab, specifies the function file, and formats the output.

The inputs to the code are: tau, IRFFWHM, delays, eKE, TRPES, and fig. Tau is a vector of initial guess for the lifetimes of the kinetic components. If the value is negative, it is treated as a decay in the negative time (probe first) direction. Any number of positive and negative lifetimes can be input. IRFFWHM is a guess at the full width at half maximum of the instrument response function (IRF). Delays and eKE are the delays and energies that the data were taken at. TRPES is the matrix to be fit.

The outputs are: DAS, taus, decays, fit, residuals, t0, FWHM, and y0. Taus are the final lifetimes after convergence of the fit. FWHM is the final width of the response function. y0 and t0 are a scaling factor and the fit zero delay point, respectively. DAS are the decay associated spectra found during the fit. The decays contain the delay dependent intensity of each of the spectral components. Finally, the fit TRPES matrix and the residuals are also made available after fitting.

Lines 47 to 51 create a matrix of initial values for the fitter. These are the variables that will eventually be optimized in the fit. The x0 matrix is as many bins wide as the number of lifetimes and as long as the number of energy bins plus four. The first four rows of the x0 matrix are the lifetimes, t0, y0, and the Gaussian width of the IRF. The remaining rows are the initial guess for the DAS, which are usually all initialized to the same value, y0.

Lines 55 to 65 can be uncommented to specify bounds on the fit parameters. Lines 71 and 72 are used as a weighting factor in the various dimensions. The helps account for the fact that the energy scaling is non-linear by weighting the low eKE region less than the high eKE (by the difference between the adjacent energy lanes). Finally, the weight matrix is multiplied by some order of magnitude in order to scale the residuals in the fit by a large enough number that the Matlab can handle. This has the side effect of increasing or decreasing the fit tolerance.

Lines 74 to 81 call Matlab's native nonlinear least squares fitting function, lsqnonlin.

Line 79 specifies that at each iteration the function outputs be generated. This allows for live monitoring of the progress of the fit but also substantially slows down the fitting routine. This functionality can be disabled by commenting out this line and line 173 to 188, which create the plot that updates at each iteration. Line 77 displays fit details in the Matlab command line at every iteration. This line also slows down the code and can be commented out as necessary.

Once the fit has completed, lines 85 to 93 pick out the fit variables to output. Lines 95 to 171 just plot the data.

Finally, in the last section of code, the inner fitting function, GeneratePES, first takes a single lifetime and creates kinetic trace. This trace is a exponential convoluted with a Gaussian. The function for the kinetics is then scaled by a constant, DAS, for every energy lane. The output of this matrix is length of eKE by length of delays matrix with a single exponential decay. This is then turned into a sum of exponential decays by the outer fitting function, GenerateTRPES.

3.3.4 Error Analysis:

In order to report an error bound, we aimed to develop a confidence interval for the globally fitted lifetimes, considering the impact of the other fit parameters. The method used here is referred to as Support Plane Analysis, but more generally it can be thought of as an F-test. In this analysis, the quality of a fit is judged by the F-statistic, which determines the values of the chi-squared distribution that are above an acceptable value for a given level of confidence (95% here). The values of each variable for which chi-squared is below that generated by the F-statistic yield a confidence interval, which can then be used as error bounds.

To conduct an F-test for a two rate constant global fit, the chi-squared for the best fit (χ^2_{min}) is first calculated. A vector of test lifetimes for each rate is then generated. For example, if the best fit lifetime is 140 fs, a vector of 100 values between 30 fs and 300 fs is generated. A least squares fit is conducted at each test value and the chi-squared value computed. For a two rate constant global fit, this is an n by n matrix of test chi-squared values. The value of the F-statistic is calculated using the equation below, where v_1 is the number of fitted parameters and v_2 is the number of degrees of freedom, χ. The degree of confidence, p, is a number between 0 and 1. Common values are 0.95 for 2σ and 0.32 for σ.

$$\frac{\chi^2_x}{\chi^2_{min}} = 1 + \frac{v_1}{v_2} F_{inv}(p|v_1, v_2) \tag{3.9}$$

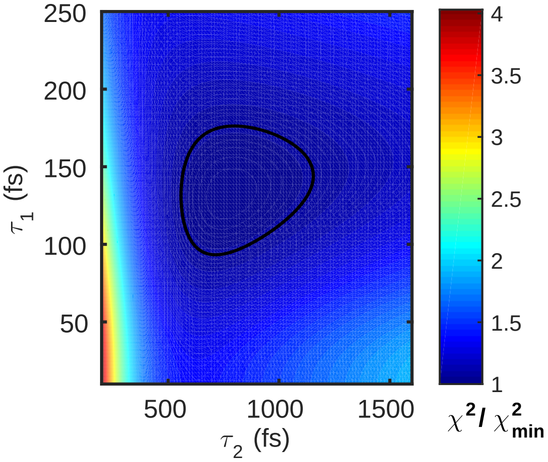

Figure 3.1: Test Chi-squared matrix for the three pulse data. The circle is the limit of the 95% confidence interval calculated from support plane analysis.

The equation above returns a number greater than one. The plane defined by $\chi^2 = \chi_x^2$ intersects the matrix of test chi-squared values at the limits of the confidence interval. Figure 5.10 shows a contour plot of the test chi-squared matrix for the three pulse methanol solvated electron data. The loop inscribed is the limit of the 95% confidence interval. This method is generalizable to any number of lifetimes. For an arbitrary number of lifetimes, the rank of the tensor of test values is equal to the number of lifetimes and is always one rank greater than the confidence interval.

Confidence Interval Code Implementation

The confidence interval code is nested set of for-loops that refit the dataset at an array of initial values. The relevant output from the fits is a comparison of the chi-squared values for each fit. This code is again a reworking of Adam Chatterly's code[7]. Significant improvements to the code have been made by parallelizing the loops such that the parallel computing capabilities of Matlab and a computational machine can be used to both tighten convergence conditions and speed up the code.

Lines 8 to 11 create a space of test lifetimes. The vector of values for each lifetime should be centered around the optimum value and contain enough width such that it samples past the confidence interval. Line 17 generates a value for chi-squared at the optimum set of fit parameters; this becomes the minimum for the test chi matrix. Lines 21 to 27 loop through the test lifetimes and fit the data to a functional form where the lifetimes are not adjustable fit parameters, defined by “DegenGlobalFitFixed”.

When a parfor-loop is called in Matlab, Matlab should automatically start a parallel pool with the default number of workers, 12. Parallelizing the loop takes a significant amount of time, so for small matrices, less than 10 by 10, it may be less efficient to run a parallel for-loop. Variables can not be defined inside of a parallel loop; therefore, the limits on the inner loop must be defined outside of the loop.

The fitting function inside the for-loop is a modified version of the global lifetime analysis code shown in the previous section. The changes to the fixed lifetime version of the code include: removing all lines of code that plot figures, commenting out the outfun and iter options in lsqnonlin, and removing the lifetimes from the matrix of optimized variables.

Finally, lines 36 and 37 count the number of variables used in the fit, and lines 32-33 and 40-43 plot the χ/χ_{min} matrix with a loop drawn at the specified confidence interval.

3.4 Shifting Global Fit:

3.4.1 General Ideas

While no chemistry must be strictly assumed for a GLA type analysis, in a second global fitting model we make some assumptions about the spectral landscape of the problem to gain a better understanding of the nature of spectral shifts. First, Gaussian line shapes have been assumed for all spectral features. This general line shape is seen in all previously published photoelectron spectra on solvated electrons and therefore seems reasonable for our model. The centers, x_i, and widths, w_i, of the Gaussians are allowed to shift with the same exponential time constant, $k_{c,i}$, which is a fit parameter in the model. In addition, each component is allowed to decay with $k_{d,i}$. The general functional form of the fits is below.

$$S(eKE,t) = \sum_{i=1}^{n} \frac{A_i}{w_i\sqrt{2\pi}} e^{-2\frac{\lambda - x_i}{w_i}^2} \int_{-\infty}^{\infty} e^{-k_{d,i}z} L(z-t)dz \tag{3.10}$$

$$w_i(t) = w_{i,\infty} + (w_{i,0} - w_{i,\infty})e^{-(t-t_0)k_{c,i}} \tag{3.11}$$

$$x_i(t) = x_{i,\infty} + (x_{i,0} - x_{i,\infty})e^{-(t-t_0)k_{c,i}} \tag{3.12}$$

3.4.2 Shifting Fit Code

The implementation of the code is a variation on the GLA code with a different set of input variables and a new fitting function. The new input variables are: the initial and final peak centers, the initial and final peak widths, the thermalization and decay lifetimes, and the variables IRFFWHM, delays, eKE, and TRPES as defined in the GLA section. The fitting function is in one part, “GeneratePESshift”, rather than two, but is otherwise similar. An arbitrary number of decaying and shifting features can be included; however, a full set of initial values must be called or the function will crash. A full set includes: one thermalization lifetime, one decay lifetime, and initial and final peak centers and widths.

The fit parameters in the x-matrix are many fewer than in the GLA code. Rather than having the same length as the number of energy bins plus four, there are nine rows of initial values corresponding to the set of initial values described above plus the zero pump-probe delay time, t0, and an initial amplitude, y0. Lines 81 to 87 call the lsqnonlin fitting function with the same options as in the GLA code. Lines 92 through 100 format the optimized variables so that the function will output them. The rest of the code plots the fit results.

3.5 References

[1] R. W. Hendler and R. I. Shrager, J. Biochem. Biophys. Methods **28**, 1 (1994).

[2] J. Shlens, CoRR **arXiv:1404.1100** (2014).

[3] I. H. M. van Stokkum, D. S. Larsen, and R. van Grondelle, Biochim. Biophys. Acta **1657**, 82 (2004).

[4] J. R. Knutson, D. G. Walbridge, and L. Brand, Biochemistry (Mosc.) **21**, 4671 (1982).

[5] H. Marciniak and S. Lochbrunner, Chem. Phys. Lett. **184**, 609 (2014).

[6] M. H. Elkins, H. L. Williams, and D. M. Neumark, J. Chem. Phys. **142**, 234501 (2015).

[7] A. S. Chatterley, *Probing Nonadiabatic Dynamics in Isolated Molecules with Ultrafast Velocity Map Imaging*, Ph.D. thesis, University of Warwick (2013).

Part II

Solvated Electron Relaxation

Chapter 4

Relaxation Mechanism of the Hydrated Electron

*Originally published as Elkins, M. H., Williams, H. W., Shreve, A. T., Neumark, D. M., Relaxation Mechanism of the Hydrated Electron. Science, **342**, 1496, (2013). Reproduced with permission.*

Abstract

The relaxation dynamics of the photoexcited hydrated electron have been subject to conflicting interpretations. Here we report time resolved photoelectron spectra of hydrated electrons in a liquid microjet with the aim of clarifying ambiguities from previous experiments. A sequence of three ultrashort laser pulses (∼100 femtosecond duration) successively created hydrated electrons by charge-transfer-to-solvent excitation of dissolved anions, electronically excited the electrons via the $s \rightarrow p$ transition, and then ejected them into vacuum. Two distinct transient signals were observed. One was assigned to the initially excited p-state with a lifetime of ∼75 fs and the other, with a lifetime of ∼400 fs, was attributed to $s-$state electrons just after internal conversion in a nonequilibrated solvent environment. These results support the nonadiabatic relaxation model.

One Sentence Summary

Time-resolved photoelectron spectroscopy in liquid jets provides new insight into the relaxation dynamics of the hydrated electron, nature's simplest quantum solute.

4.1 Main Text

The hydrated electron e^-_{aq} is a species of fundamental interest in the chemistry of water. It has been implicated in phenomena ranging from aerosol nucleation to radiation damage in DNA [1]. As the simplest quantum solute, with only a single electronic degree of freedom, it has been the focus of many experimental and theoretical studies over the years [2–4]. Nonetheless, many of its key attributes remain controversial. For example, the standard picture [5] of an electron residing in a cavity of radius $< 2.4\mathring{A}$ has been repeatedly questioned [6]. Another unresolved issue concerns the relaxation mechanism of e^-_{aq} subsequent to electronic excitation. This mechanism, which represents a subtle interplay between solute-solvent interactions and electronically non-adiabatic dynamics, is of critical importance in hydrated electron chemistry and radiation biology, given that excited states of e^-_{aq} are considerably more reactive than its ground state [7]. The relaxation dynamics of e^-_{aq} upon excitation have been studied in bulk water using transient absorption (TA) [8–10] and resonance Raman spectroscopy [11]. Complementary studies have also been carried out in size-selected water cluster anions using time-resolved photoelectron spectroscopy (TRPES) [12]. In this work, we connect these very disparate experimental techniques, using TRPES of hydrated electrons in liquid water microjets to resolve key questions regarding the relaxation mechanism of e^-_{aq}.

The hydrated electron has a characteristic electronic spectrum peaking at 720 nm that is attributed to excitation from its ground *s*-state to a manifold of excited *p*-states within the solvent cavity [13]. The proposed relaxation mechanism following $s \to p$ excitation is shown in Fig. 4.1. It comprises solvent relaxation in the *p*-state, $p \to s$ internal conversion, and solvent relaxation in the *s*-state. These three processes are characterized by time constants τ_P, τ_{IC}, and τ_S. In TA experiments by Barbara and coworkers [8], the $s \to p$ transition was excited with a femtosecond pump pulse, and the resulting dynamics were followed by the absorption of a broadband femtosecond probe pulse. Three time scales of 50 to 80 fs, 200 to 400 fs, and 1.1 ps were identified and have been largely reproduced by other laboratories [9, 10]. However, the assignment of these lifetimes to particular physical phenomena has been a matter of some debate. Two basic models (Fig. 4.1) are proposed: the “adiabatic” model and the “nonadiabatic” model [2]. The adiabatic model assigns the rapid timescale (50 to 80 fs) to τ_P, the intermediate time scale to τ_{IC}, and the slow timescale to τ_S. Alternatively, the “nonadiabatic” model assigns the fastest observable time scale to τ_{IC} and the slower two to τ_S. From TA alone, one cannot easily distinguish between the two models, and differing theoretical treatments have favored both models [14, 15].

TRPES of anionic water clusters $(H_2O)^-_n$, provides a different perspective on hydrated electron relaxation dynamics [16–19]. In these experiments, the excess electron is electronically excited with a femtosecond pump pulse and then photodetached with a femtosecond probe pulse. The resulting time-dependent photoelectron spectra show a transient feature clearly associated with the cluster excited state and directly yield τ_{IC} at each cluster size. These experiments show that τ_{IC} decreases from 190 fs to 60 fs with increasing cluster size

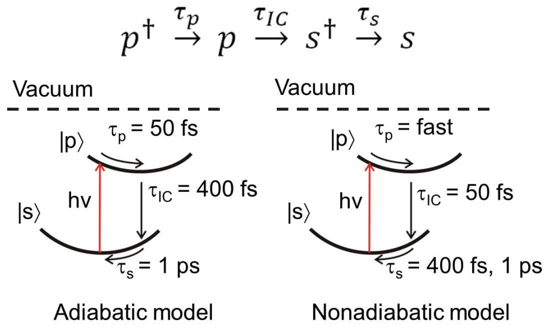

Figure 4.1: Proposed relaxation mechanism of the electronically excited hydrated electron. Initial p-state solvent relaxation is followed by IC and then s-state solvent relaxation. Adiabatic (left) and non-adiabatic (right) models differ primarily in τ_{IC}.

up to 200 water molecules. Extrapolating this trend to the bulk ($n \to \infty$) limit implies $\tau_{IC} =$ 60 fs for e^-_{aq}. This trend suggests that the fastest time constant seen in the TA experiments corresponds to τ_{IC}, consistent with the non-adiabatic relaxation model (Fig. 4.1).

The validity of this conclusion depends on whether water cluster anions are in fact gas phase analogues of e^-_{aq}, a subject of considerable discussion [2, 20, 21]. Recent experiments on liquid water microjets have tested this correspondence directly by using photoelectron spectroscopy to measure the vertical detachment energy (VDE) of hydrated electrons in liquid jets [22–26]. The value obtained, 3.3 to 3.5 eV, agrees well with the extrapolated VDE obtained from photoelectron spectra of water cluster anions [18, 27, 28], and raises the question of whether the cluster dynamics will also extrapolate to an observable bulk quantity. In this paper, we report TRPES experiments on liquid water jets that directly yield the p-state lifetime of e^-_{aq}, resolving which of the two models in Fig. 4.1 is more appropriate. Our results provide the missing link between the time-resolved water cluster anion experiments and the TA work on bulk hydrated electrons.

The principle of the experiment, in which three femtosecond laser pulses interact with a liquid water jet, is outlined in Fig. 4.2 and in Eq. 4.1.

$$A^-_{(aq)} \overset{h\nu_1,\Delta t_{12}}{\longrightarrow} A_{(aq)} + e^-_{(aq)}(s) \overset{h\nu_2,\Delta t_{23}}{\longrightarrow} e^-_{(aq)}(p) \overset{h\nu_3}{\longrightarrow} e^-_{(vac)} \tag{4.1}$$

The first pulse, $h\nu_1$, is centered at 239 nm and generates hydrated electrons via charge transfer to solvent (CTTS) excitation of a precursor anion; results are reported here for a 100 mM solution of I^-, but identical results were obtained using $Fe(CN)_6^{4-}$. The time (Δt_{12}) between $h\nu_1$ and the pump pulse, $h\nu_2$ (800 nm, 1.55 eV, 85 fs), is held at 200 ps to en-

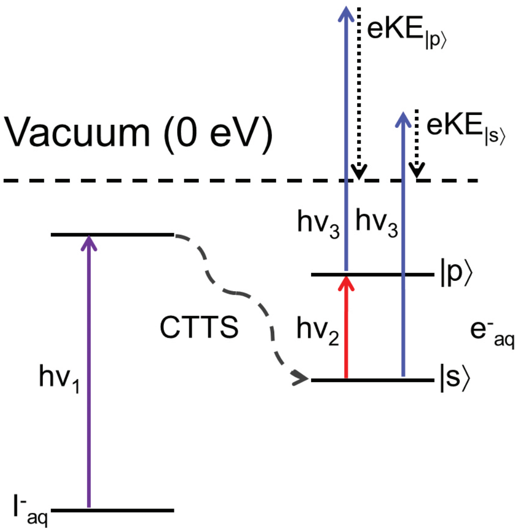

Figure 4.2: Energy diagram of experiment. Three femtosecond laser pulses interact with the liquid jet.

sure a population of equilibrated, ground state hydrated electrons [29]. The pump pulse lies within the $s \to p$ absorption band and excites an electron to the p-state manifold. The probe pulse, $h\nu_3$ (266 nm, 4.65 eV, 125 fs), then detaches the electron to vacuum. The resulting photoelectron kinetic energy (eKE) distribution is measured as a function of Δt_{23}. Because TRPES measures the energy of populated states relative to vacuum, electrons ejected from the p-state will have higher eKE than those ejected from the s-state, which enables us to distinguish between them. The experimental set-up comprises a liquid jet source described elsewhere [25, 30], a 1 kHz femtosecond laser system, and a magnetic bottle electron spectrometer [26, 31].

Shown in Fig. 4.3 are TRPE spectra using two background subtraction schemes. The eKE scale is corrected for the liquid jet streaming potential as described previously.[30, 32] The photoelectron spectrum is shown in Fig. 4.3A, with the individual one-color contributions from $h\nu_1$ and $h\nu_3$ subtracted from the three-pulse spectra. Each ultraviolet beam causes a delay-invariant two-photon signal from detachment of the precursor anion, which we treat as background. A short-lived transient feature above 2.0 eV and a broad, intense feature centered at 1.2 eV are shown in Fig. 4.3A. The latter corresponds to a VDE ($=h\nu_3$-1.2 eV) of 3.45 eV and is readily assigned to detachment of the s-state of e^-_{aq} based on previous work. [23–26] Recent experiments [33, 34] suggest that the escape depth in liquid water for photoelectrons in this eKE range (1-3 eV) is at least 5 nm, which is approximately a factor of 20 larger than the cavity radius of e^-_{aq}. These results imply the detached electrons seen here are not predominantly sampled from the jet surface.

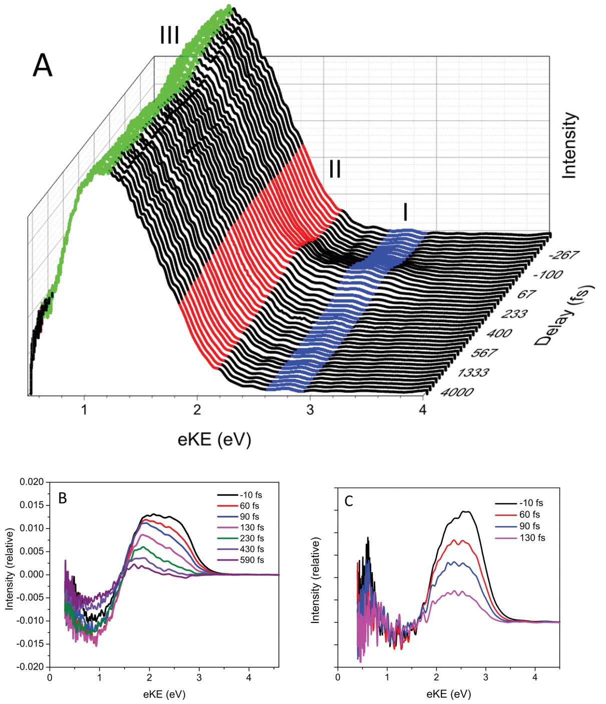

Figure 4.3: Time resolved photoelectron spectra. The plots show three-pulse spectra from which (A) the contribution from each one color spectrum has been subtracted and (B) the ($h\nu_1 + h\nu_3$) two-color spectrum has been subtracted. (C) Spectra from (B) at early times, showing curve at 230 fs subtracted.

The result of subtracting the ($h\nu_1 + h\nu_3$) two-pulse spectrum from the three-pulse spectrum at each delay time is shown in Fig. 4.3B at each delay time. These difference spectra show how the photoelectron signal changes with the addition of the pump pulse, $h\nu_2$. Here, positive signal is induced by $h\nu_2$, while negative-going signal represents depletion by $h\nu_2$. The depleted signal overlaps the ground state feature in Fig 3A. The positive signal in Fig. 4.3B exhibits a shoulder from 2.3 to 2.6 eV at the earliest delays that disappears within 100 fs. By 230 fs (green trace), the signal has evolved into a smaller transient feature peaking around 1.7 eV that continues to decay and shift toward lower eKE on a significantly longer timescale. The early-time behavior of the shoulder at high eKE can be more readily discerned by subtracting the curve at 230 fs from those at earlier times. The result, shown in Fig. 4.3C, is a peak centered around 2.5 eV.

To gain further insight into these dynamics, integrated signal is shown in Fig. 4.4 as a function of delay over three energy intervals indicated in Fig. 4.3A. Data are shown as points, and the solid lines are fitting functions. These regions are well fit by a simple sequen-

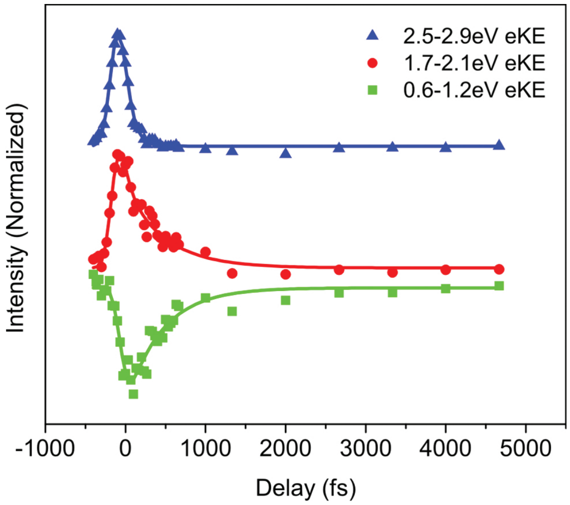

Figure 4.4: Integrated intensity as a function of delay over three eKE intervals. Colors are the same as in Fig. 4.3A.

tial three-step mechanism ($I \xrightarrow{\tau_1} II \xrightarrow{\tau_2} III$) with time constants $\tau_1 = 75 \pm 20$ fs and $\tau_2 = 410 \pm 40$ fs. In Fig. 4.4, the blue curve is associated with I in the mechanism, red with II, and green with III. The fitting functions for each step in the mechanism are a convolution of the measured pump-probe cross-correlation (115 fs) with the kinetic rate equation for each step (supplementary text).

The blue curve in Fig. 4.4 corresponds to eKEs separated from the ground state feature by $h\nu_2$ and is assigned to the initially excited p-state. The green curve indicates that the ground state is initially depleted by the pump pulse but that its population recovers as the p-state relaxes. The existence of an intermediate state II is inferred from the observation that ground state recovery is noticeably slower than decay of the blue curve. With reference to Fig. 4.1, state II can be assigned either to p-state signal subsequent to solvent relaxation in the excited state, or to s-state signal just after IC, in which the electron is surrounded by a non-equilibrium distribution of solvent molecules. This assignment determines whether the decay of the blue signal in Fig. 4.4 corresponds to relaxation within the p-state or to internal conversion to the s-state.

The latter assignment is supported by several factors. First, as shown in Fig. 4.3A., the energy interval corresponding to feature II falls on the high eKE edge of the ground state spectrum but clearly lies within the eKE range of the ground state, just where one would expect to see a contribution from vibrationally hot s-state signal. A close examination of Fig. 4.3B suggests that for Δt_{12} <230 fs, the pump-induced signal shifts toward lower eKE as it loses intensity, as one might expect for signal associated with solvent relaxation on the ground state.

Moreover, assigning the red signal to the relaxed *p*-state signal would indicate an energy shift of around -0.8 eV within the *p*-state subsequent to photoexcitation, as seen from the difference between the blue and red energy windows and the data in Fig. 4.3B. Quantum-classical molecular dynamics simulations of hydrated electron pump-probe signal using various electron-water pseudopotentials do not support such a large energy shift [6, 14]; instead, they find the *p*-state energy remains nearly constant while the *s*-state energy exhibits large fluctuations. It thus appears more reasonable to assign the decay of the blue signal I to IC, and the decay (recovery) of the red (green) signal to solvent relaxation on the *s*-state subsequent to IC. This assignment then yields $\tau_1 = \tau_{IC} = 75 \pm 20$ fs, while $\tau_2 = \tau_s = 410 \pm 40$ fs represents the time constant for solvent relaxation subsequent to internal conversion.

Our value of 75 ± 20 fs for τ_{IC} supports the non-adiabatic relaxation mechanism shown in Fig. 4.1, apparently resolving the ambiguity from the TA experiments (which yielded similar time constants). Moreover, this value is remarkably consistent with the extrapolated τ_{IC} of 60 fs obtained from size-selected water cluster anions, suggesting that both the relaxation dynamics and the VDEs for water cluster anions can be extrapolated to bulk values. The data as interpreted here also yield a measurement of the VDE for the *p*-state of the hydrated electron, 2.2 ± 0.2 eV, taking the center of the eKE distribution in Fig. 4.3C to be 2.5 eV.

We next consider whether our results show any evidence for *p*-state relaxation. Our more recent work on water cluster anions showed the *p*-state photoelectron signal shifting to lower eKE on the same time scale as IC, implying that these the two processes occur in parallel[18]. Similar dynamics are suggested here by Fig. 4.3C, which shows the early-time signal shifting toward lower eKE as it disappears. However, this *p*-state signal overlaps the hot *s*-state signal, which is shifting in the same direction, so the trend in Fig. 4.3C should be viewed with caution. We do not see evidence for the slowest time constant (1.1 ps) seen in the TA experiments, possibly because relatively few data points were taken at long time delays.

The experiments presented here open up the possibility of tracking solvated electron dynamics in methanol and other solvents, in which similar mechanistic issues have been raised from TA experiments [35]. Also, with differing excitation schemes [36] it should be possible to probe the relaxation dynamics of pre-hydrated and conduction band electrons in liquid water jets. These electrons are more highly excited and delocalized than the *p*-state electrons probed here, and their energetics and dynamics have been investigated but are less well-characterized [37–39]. Hence, TRPES in liquid jets offers considerable potential for unraveling electron dynamics in water and other solvents.

References and Notes

4.2 References

[1] B. C. Garrett, D. A. Dixon, D. M. Camaioni, D. M. Chipman, M. A. Johnson, C. D. Jonah, G. A. Kimmel, J. H. Miller, T. N. Rescigno, P. J. Rossky, S. S. Xantheas, S. D. Colson, A. H. Laufer, D. Ray, P. F. Barbara, D. M. Bartels, K. H. Becker, K. H. Bowen, S. E. Bradforth, I. Carmichael, J. V. Coe, L. R. Corrales, J. P. Cowin, M. Dupuis, K. B. Eisenthal, J. A. Franz, M. S. Gutowski, K. D. Jordan, B. D. Kay, J. A. LaVerne, S. V. Lymar, T. E. Madey, C. W. McCurdy, D. Meisel, S. Mukamel, A. R. Nilsson, T. M. Orlando, N. G. Petrik, S. M. Pimblott, J. R. Rustad, G. K. Schenter, S. J. Singer, A. Tokmakoff, L.-S. Wang, and T. S. Zwier, Chem. Rev. **105**, 355 (2005).

[2] L. Turi and P. J. Rossky, Chem. Rev. **112**, 5641 (2012).

[3] B. Abel, Annu. Rev. Phys. Chem. **64**, 533 (2013).

[4] R. M. Young and D. M. Neumark, Chem. Rev. **112**, 5553 (2012).

[5] P. J. Rossky and J. Schnitker, J. Phys. Chem. **92**, 4277 (1988).

[6] R. E. Larsen, W. J. Glover, and B. J. Schwartz, Science **329**, 65 (2010).

[7] E. Alizadeh and L. Sanche, Chem. Rev. **112**, 5578 (2012).

[8] K. Yokoyama, C. Silva, D. H. Son, P. K. Walhout, and P. F. Barbara, J. Phys. Chem. A **102**, 6957 (1998).

[9] M. Assel, R. Laenen, and A. Laubereau, Chem. Phys. Lett. **317**, 13 (2000).

[10] M. S. Pshenichnikov, A. Baltuska, and D. A. Wiersma, Chem. Phys. Lett. **389**, 171 (2004).

[11] M. J. Tauber and R. A. Mathies, J. Phys. Chem. A **105**, 10952 (2001).

[12] D. M. Neumark, Mol. Phys. **106**, 2183 (2008).

[13] E. J. Hart and J. W. Boag, J. Am. Chem. Soc. **84**, 4090 (1962).

[14] B. J. Schwartz and P. J. Rossky, J. Chem. Phys. **101**, 6902 (1994).

[15] A. A. Zharikov and S. F. Fischer, J. Chem. Phys. **124**, 054506 (2006).

[16] J. M. Weber, J. Kim, E. A. Woronowicz, G. H. Weddle, I. Becker, O. Cheshnovsky, and M. A. Johnson, Chem. Phys. Lett. **339**, 337 (2001).

[17] A. E. Bragg, J. R. R. Verlet, A. Kammrath, O. Cheshnovsky, and D. M. Neumark, Science **306**, 669 (2004).

[18] G. B. Griffin, R. M. Young, O. T. Ehrler, and D. M. Neumark, J. Chem. Phys. **131**, 194302 (2009).

[19] D. H. Paik, I.-R. Lee, D.-S. Yang, J. S. Baskin, and A. H. Zewail, Science **306**, 672 (2004).

[20] O. Marsalek, F. Uhlig, T. Frigato, B. Schmidt, and P. Jungwirth, Phys. Rev. Lett. **105**, 043002 (2010).

[21] L. D. Jacobson and J. M. Herbert, J. Am. Chem. Soc. **133**, 19889 (2011).

[22] B. Winter and M. Faubel, Chem. Rev. **106**, 1176 (2006).

[23] K. R. Siefermann, Y. X. Liu, E. Lugovoy, O. Link, M. Faubel, U. Buck, B. Winter, and B. Abel, Nature Chemistry **2**, 274 (2010).

[24] Y. Tang, Y.-i. Suzuki, H. Shen, K. Sekiguchi, N. Kurahashi, K. Nishizawa, P. Zuo, and T. Suzuki, Chem. Phys. Lett. **494**, 111 (2010).

[25] A. T. Shreve, T. A. Yen, and D. M. Neumark, Chem. Phys. Lett. **493**, 216 (2010).

[26] A. Lübcke, F. Buchner, N. Heine, I. V. Hertel, and T. Schultz, Phys. Chem. Chem. Phys. **12**, 14629 (2010).

[27] J. V. Coe, G. H. Lee, J. G. Eaton, S. T. Arnold, H. W. Sarkas, K. H. Bowen, C. Ludewigt, H. Haberland, and D. R. Worsnop, J. Chem. Phys. **92**, 3980 (1990).

[28] L. Ma, K. Majer, F. Chirot, and B. von Issendorff, J. Chem. Phys. **131**, 144303 (2009).

[29] J. A. Kloepfer, V. H. Vilchiz, V. A. Lenchenkov, A. C. Germaine, and S. E. Bradforth, J. Chem. Phys. **113**, 6288 (2000).

[30] A. T. Shreve, M. H. Elkins, and D. M. Neumark, Chemical Science **4**, 1633 (2013).

[31] P. Kruit and F. H. Read, Journal of Physics E: Scientific Instruments **16**, 313 (1983).

[32] T. Horio, H. Shen, S. Adachi, and T. Suzuki, Chem. Phys. Lett. **535**, 12 (2012).

[33] F. Buchner, T. Schultz, and A. Lubcke, Phys. Chem. Chem. Phys. **14**, 5837 (2012).

[34] S. Thürmer, R. Seidel, M. Faubel, W. Eberhardt, J. C. Hemminger, S. E. Bradforth, and B. Winter, Phys. Rev. Lett. **111**, 173005 (2013).

[35] A. Thaller, R. Laenen, and A. Laubereau, J. Chem. Phys. **124**, 024515 (2006).

[36] P. Kambhampati, D. H. Son, T. W. Kee, and P. F. Barbara, J. Phys. Chem. A **106**, 2374 (2002).

[37] A. Migus, Y. Gauduel, J. L. Martin, and A. Antonetti, Phys. Rev. Lett. **58**, 1559 (1987).

[38] X. Shi, F. H. Long, H. Lu, and K. B. Eisenthal, J. Phys. Chem. **100**, 11903 (1996).

[39] C.-R. Wang, T. Luo, and Q.-B. Lu, Phys. Chem. Chem. Phys. **10**, 4463 (2008).

Acknowledgments

This research is supported by the National Science Foundation (NSF) under Grant No. CHE-1011819. The data presented in this paper are available upon request sent to dneumark@berkeley.edu.

4.3 Supplemental Material

Materials and Methods

As depicted in the equation below, hydrated electrons are generated via charge transfer to solvent excitation (CTTS) of a precursor anion in solution with $h\nu_1$, then excited with $h\nu_2$, and detached to vacuum with $h\nu_3$.

$$A^-_{(aq)} \xrightarrow{h\nu_1,\Delta t_{12}} A_{(aq)} + e^-_{(aq)}(s) \xrightarrow{h\nu_2,\Delta t_{23}} e^-_{(aq)}(p) \xrightarrow{h\nu_3} e^-_{(vac)} \tag{4.2}$$

Precursor anions are introduced by dissolving potassium iodide (EMD, ≥99% purity) or potassium hexacyanoferrate (Sigma, ≥99.5% purity) in deionized and filtered water (18MΩ resistivity Milli-Q, Millipore). The concentration of the solution (100mM) is optimized to minimize streaming potentials. Solutions are introduced to vacuum by applying a high backing pressure (115 atm) to the liquid behind a 20 μm ID fused silica capillary. The flow rate is fixed at 0.25 mL/min resulting in a jet velocity of 13 m/s. The jet maintains a laminar flow region for 1 - 4 mm before breaking up in to droplets. Excess solution is collected in a liquid nitrogen cooled trap allowing for running pressures of $1x10^{-4}$ Torr in the liquid jet region.

Femtosecond pulses are generated from a Spectra Physics Spitfire amplifier (2.2 W, 75 fs, 1 kHz). The CTTS excitation pulse ($h\nu_1$, 239 nm, ∼175 nJ) is generated from the second harmonic of the sum-frequency signal output from a Light Conversion TOPAS. The excitation pulse ($h\nu_2$, 800 nm, 85 fs, ∼300 nJ) is recovered from the output of the third harmonic generator used to create the detachment pulse ($h\nu_3$, 266 nm, 125 fs, ∼150 nJ). A 200 ps delay is maintained between $h\nu_1$ and $h\nu_2$. The delay between $h\nu_2$ and $h\nu_3$ is varied to generate time resolved photoelectron spectra. Power dependence of the TR signal on each beam was

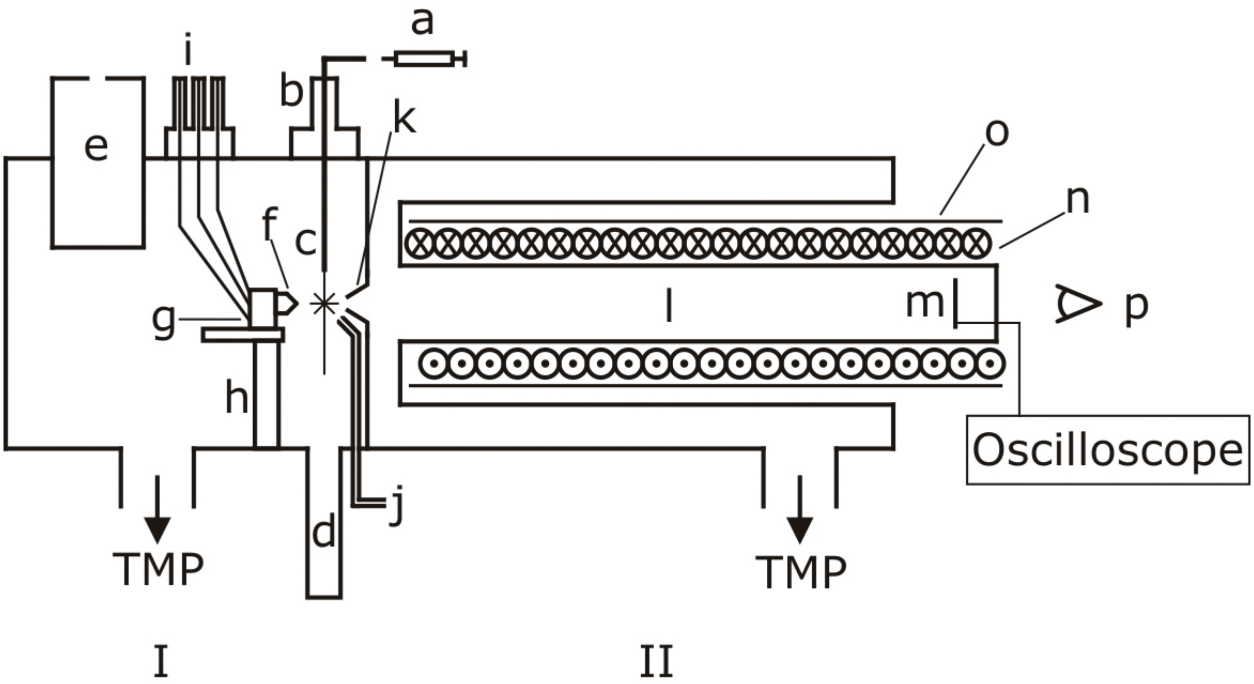

Figure 4.5: (a) Syringe pump, (b) Three-axis translation stage, (c) Microjet assembly, (d) Cryotrap, (e) Liquid nitrogen dewar, (f) Magnets, (g) Three-axis translation stage, (h) Post and platform, (i) Picomotor electrical feed-through, (j) Calibration gas inlet, (k) Skimmer and differential pumping sheath, (l) Flight tube, (m)Detector, (n) Solenoid, (o) Magnetic shielding, (p) Camera, (I) liquid jet region (II) detector region

found to be linear in the experimental regime. The temporal widths reported in the text are the average single pulse durations at the chamber, i.e. the full width at half maximum of the cross-correlation divided by $\sqrt{2}$.

A schematic diagram of the experimental setup is provided in Fig. 4.5. Electrons are sampled through a 500 μm skimmer located 1 mm from the jet. This allows for an operating pressure of $1.5x10^{-6}$ Torr in the detector region. The collection efficiency of generated photoelectrons has been greatly improved since our last publication via the implementation of a magnetic bottle. A strong magnet (1 T, Nd) near the interaction region generates an inhomogeneous magnetic field, which guides electrons into the flight tube, where a solenoid generates a uniform, 50 Gauss, magnetic field. In principle, 50% of generated photoelectrons are collected and impact the chevron stack, microchannel plate (MCP) detector.

The time of arrival distribution of ejected photoelectrons at the MCP is collected on an oscilloscope, and PE spectra are taken at various pump probe delays. To account for any effect from jet fluctuation, background spectra are interleaved and subsequently subtracted.

This background signal from both ultraviolet beams is caused by two-photon detachment of iodide in the microjet and is consistent with results reported elsewhere. The background subtraction is performed in one of two ways: either by subtraction of the $(h\nu_1+h\nu_3)$ two-color spectrum or by subtracting each $h\nu_1$ and $h\nu_3$ spectrum separately. The subtracted spectra are then averaged and converted to eKE using the appropriate Jacobian transformation (t^{-3}). While individually subtracting the one-color contributions clearly shows the ground state and draws a parallel to earlier work in water cluster anions, the subtraction method in Fig. 4.3B more clearly shows the timescales on which the photoelectron spectra change, and as such, both spectra are included.

While potassium iodide was used as the primary solvated electron source in these data, spectra using potassium hexacyanoferrate were taken as a check for precursor effects on the dynamics. No difference in the dynamics was found. Both $h\nu_1$ and $h\nu_3$ are resonant with the CTTS band in hexacyanoferrate; therefore, photodetachment of electrons from the precursor is competitive with the solvated electron signal, which lowers the signal to noise in these spectra. Liquid jet streaming potentials are measured by three-photon ionization of xenon in the presence of the charged jet, and calibration spectra are generated from this same method but in the absence of the jet field. This method is described in more detail elsewhere(28). The TRPE spectra in the text are included with an appropriate correction for the streaming potential for that day (typically 0.175 eV).

Supplementary Text

Fitting functions for TR Spectra

The integrated intensity of the time resolved spectra over the three regions of interest in the text are fit by a simple three-step sequential kinetic model ($I \xrightarrow{\tau_1} II \xrightarrow{\tau_2} III$). The solutions to the differential equations for intensity as a function of time are provided below. H(t) is the Heaviside step function centered at the origin. The leading constants for each step are allowed to float to account for difference intensity in each lane due to the width of the integration lane and the relevant photodetachment cross section for each state. The additive constant in C sets the initial value above zero.

$$A = A_0 e^{-\frac{t}{\tau_1}} * H(t) \qquad B = \frac{B_0}{\tau_1(\frac{1}{\tau_1} - \frac{1}{\tau_2})}[e^{-\frac{t}{\tau_2}} - e^{-\frac{t}{\tau_1}}] \tag{4.3}$$

$$C = C_1 - \frac{H(t) * C_0}{\left(\frac{1}{\tau_1} - \frac{1}{\tau_2}\right)} \left[\frac{e^{-\frac{t}{\tau_2}}}{\tau_1} - \frac{e^{-\frac{t}{\tau_1}}}{\tau_2}\right] \tag{4.4}$$

These kinetic equations are then convoluted with the Gaussian instrumental response function below following the method described in Pederson and Zewail(40). The width of the response function (σ) is generated from the measured cross correlation. The Gaussian also allows for a shift on the time axis (t_0) to account for any mistake in our assignment of the zero delay time.

$$L = \frac{1}{\sqrt{2\pi}\sigma} e^{-\frac{(t-t_0)^2}{2\sigma^2}} \tag{4.5}$$

The results of this convolution for each A, B, and C are given below:

$$A = \frac{A_0}{2} e^{\frac{\sigma^2}{2{\tau_1}^2} - \frac{t-t_0}{\tau_1}} \left[1 + erf\left(\frac{t-t_0}{\sqrt{2}\sigma} - \frac{\sigma}{\tau_1\sqrt{2}} \right) \right] \tag{4.6}$$

$$\begin{aligned} B = \frac{B_0}{\tau_1\left(\frac{1}{\tau_1} - \frac{1}{\tau_2}\right)} \Bigg[& e^{\frac{\sigma^2}{2{\tau_2}^2} - \frac{t-t_0}{\tau_2}} erf\left(\frac{t-t_0}{\sqrt{2}\sigma} - \frac{\sigma}{\tau_2\sqrt{2}} \right) \dots \\ & - e^{\frac{\sigma^2}{2{\tau_1}^2} - \frac{t-t_0}{\tau_1}} erf\left(\frac{t-t_0}{\sqrt{2}\sigma} - \frac{\sigma}{\tau_1\sqrt{2}} \right) \Bigg] \end{aligned} \tag{4.7}$$

$$\begin{aligned} C = C_1 - \frac{C_0}{2\left(\frac{1}{\tau_1} - \frac{1}{\tau_2}\right)} \Bigg[& e^{\frac{\sigma^2}{2{\tau_2}^2} - \frac{t-t_0}{\tau_2}} \left\{ 1 + erf\left(\frac{t-t_0}{\sqrt{2}\sigma} - \frac{\sigma}{\tau_2\sqrt{2}} \right) \right\} \dots \\ & - e^{\frac{\sigma^2}{2{\tau_1}^2} - \frac{t-t_0}{\tau_1}} \left\{ 1 + erf\left(\frac{t-t_0}{\sqrt{2}\sigma} - \frac{\sigma}{\tau_1\sqrt{2}} \right) \right\} \Bigg] \end{aligned} \tag{4.8}$$

The measured cross correlation width for each day of data is treated as a known quantity. Only the scaling factors, both lifetimes, and the zero delay time are fit parameters ($A_0, B_0, C_0, C_1, \tau_1, \tau_2,\ \&\ \ t_0$).

Extended Acknowledgements

M.H.E. and H.L.W. would like to thank Mark Shapero for his work developing data analysis software.

Chapter 5

Dynamics of Electron Solvation in Methanol: Excited State Relaxation and Generation by Charge-Transfer-to-Solvent

*Originally published as Elkins, M. H., Williams, H. W., Neumark, D. M., Dynamics of Electron Solvation in Methanol: Excited State Relaxation and Generation by Charge Transfer to Solvent, Journal of Chemical Physics, **142**, 234501, (2015). Reproduced with permission.*

Abstract

The charge-transfer-to-solvent dynamics (CTTS) and excited state relaxation mechanism of the solvated electron in methanol are studied by time-resolved photoelectron spectroscopy on a liquid methanol microjet by means of two-pulse and three-pulse experiments. In the two-pulse experiment, CTTS excitation is followed by a probe photoejection pulse. The resulting time-evolving photoelectron spectrum reveals multiple time scales characteristic of relaxation and geminate recombination of the initially generated electron which are consistent with prior results from transient absorption. In the three-pulse experiment, the relaxation dynamics of the solvated electron following electronic excitation are measured. The internal conversion lifetime of the excited electron is found to be 130 ± 40 fs, in agreement with extrapolated results from clusters and the non-adiabatic relaxation mechanism.

5.1 Introduction

The solvated electron, an isolated electron in polar solution, is a species of fundamental interest to the physics of solvation and to the understanding of condensed phase reactions in the presence of ionizing radiation.[1] The solvated electron is the simplest quantum solute and is thus a fundamental model system for understanding solute-solvent interactions. As such, it has been the target of much experimental[2–4] and theoretical[5, 6] study in the context of solvation. Nonetheless, many aspects of solvated electron dynamics remain unresolved, even in water and methanol, which have been studied extensively. Recently, it has become possible to couple liquid microjets to photoelectron spectroscopy [7, 8] and to measure the photoelectron spectrum (PES) of excess electrons in high vapor pressure solvents.[9] In particular, by performing time-resolved photoelectron spectroscopy (TRPES) on electrons in liquid water jets, key dynamical issues associated with solvated electrons can be addressed that could not be explored directly by other means.[10–13] Here, this technique is used to investigate the dynamics of solvated electrons in methanol subsequent to (a) their formation by charge-transfer-to-solvent (CTTS) excitation and (b) electronic excitation of the $s \rightarrow p$ transition.

The absorption spectra of solvated electrons in water[14] and methanol[15] exhibit a single broad peak in the near-infrared, 720 nm in water and 630 nm in methanol, associated with a transition from the ground "s-like" state to a quasi-degenerate manifold of "p-like" states.[16] Much of the experimental work on the solvated electron in the two solvents has used this band as a probe of its solvation dynamics, primarily via transient absorption (TA) [17–23] and resonance Raman spectroscopy.[24, 25] In TA experiments, solvated electrons are typically generated by ionization of the solvent or by photodetachment from a precursor anion. Subsequent evolution of the $s \rightarrow p$ band probes the time it takes the photogenerated electron to equilibrate and, depending on the experiment, the relaxation dynamics of the electron from its excited p-state.

Time-resolved experiments on solvated electrons generated by excitation of a precursor anion in solution, such as an atomic halide ion, have been particularly useful for elucidating the dynamics of these species.[2, 26] Gas phase halides have no bound excited states, but in solution these anions have broad charge-transfer-to-solvent (CTTS) bands in the ultraviolet[27, 28] corresponding to short lived excited states that rapidly decay to solvated electrons.[29] In contrast to photoionization or radiolysis of pure solvents, solvated electrons created by this method are generated well below the water conduction band, which can simplify the observed dynamics by limiting the excess energy of the ejected electron.[30] In TA experiments on water[22, 31–33] and methanol[34] aimed at understanding electron solvation subsequent to CTTS excitation, a UV femtosecond laser pulse generates electrons via CTTS excitation, and the subsequent recombination and solvation dynamics of these electrons are interrogated by a second broadband femtosecond pulse that probes the $s \rightarrow p$ absorption band. These experiments have stimulated theoretical efforts aimed at understanding the underlying dynamics.[35–37]

In complementary three-pulse TA experiments, solvated electrons are generated by CTTS excitation in the UV and allowed to equilibrate. The $s \rightarrow p$ transition is then excited by a near infrared (NIR) pulse, and the resulting dynamics are probed by TA with a broadband pulse. These so-called pump-repump-probe measurements were first carried out by Barbara and co-workers[20] in water and, more recently, by Barbara[38] and Thaller et al[39] in methanol. These measurements yield multiple time scales associated with relaxation of the electronically excited electrons. Two competing models describe the p-state relaxation, the "adiabatic" and "non-adiabatic" models, which differ according to whether the fastest time scale seen in TA experiments is assigned to p-state relaxation or $p \rightarrow s$ internal conversion.[20] Identifying the most appropriate model has been the subject of considerable debate despite a large body of theoretical work on solvated electrons in water[6, 40, 41] and methanol.[42–46]

Experimentally, distinguishing between these two mechanisms requires a direct measurement of the p-state lifetime. Extracting this value from TA experiments is not straightforward, but it can be readily obtained from time-resolved photoelectron spectroscopy. [47, 48] In our laboratory, experiments on size-selected $(H_2O)_n^-$ and $(CH_3OH)_n^-$ anion clusters using TRPES yielded p-state lifetimes as a function of cluster size that extrapolated to bulk values of 60 and 150 fs for water and methanol, respectively.[49–51] These results support the non-adiabatic model for both solvents, but one can question the validity of such extrapolations to elucidate bulk phenomena.

Since 2010, several laboratories have carried out photoelectron spectroscopy experiments on electrons in liquid jets of water and other solvents in order to explicitly "bridge the gap" between the cluster and bulk liquid regimes. These experiments have yielded the vertical binding energy of electrons in water, methanol, and acetonitrile.[9, 11, 13, 52–55] Time-resolved PES experiments have been carried out in liquid water jets via the two-pulse and three-pulse schemes outlined by Eqs. (5.1) and (5.2), respectively, in which the second (or third) laser pulse ejects photogenerated electrons from aqueous solution to vacuum and their kinetic energy distribution is measured.

$$I^-_{(aq)} \xrightarrow{h\nu_1} I^*_{CTTS} \xrightarrow{\Delta t_{12}} e^-_{(aq)} \xrightarrow{h\nu_2} e^-_{(vac)} \tag{5.1}$$

$$I^-_{(aq)} \xrightarrow{h\nu_1,\Delta t_{12}} I_{(aq)} + e^-_{(aq)}(s) \xrightarrow{h\nu_2,\Delta t_{23}} e^-_{(aq)}(p) \xrightarrow{h\nu_3} e^-_{(vac)} \tag{5.2}$$

Two-pulse TRPES experiments in water provide complementary information to two-pulse TA experiments.[10, 11] Recent three-pulse TRPES experiments on hydrated electrons in liquid water jets yielded an excited state lifetime of 75 ± 20 fs, which is in agreement with the cluster extrapolation and provides further evidence for the non-adiabatic model of hydrated electron relaxation.[12]

Here, we carry out two-pulse and three-pulse TRPES experiments on methanol liquid jets based on Eqs. (1) and (2). Solvated electrons in methanol formed by CTTS excitation undergo a multistep mechanism consisting of a 550 ± 110 fs decay attributed to decay of the relaxed CTTS state, an 8 ± 3 picosecond thermalization of a "hot" population of electrons, and a partial decay of the ground state electron signal on a time scale of 41 ± 7 picoseconds. The excited state solvated electron, as examined from the three-pulse experiment, is shown to undergo internal conversion to the ground state with a 130 ± 40 fs lifetime. The ground state then re-equilibrates with a lifetime of 800 ± 300 fs. The fast internal conversion lifetime is consistent with the non-adiabatic mechanism along with prior results in water and extrapolated results from methanol cluster anions.

5.2 Methods

The experimental apparatus for carrying out time-resolved photoelectron spectroscopy of liquid jets is shown schematically in Figure 5.1. The design of the liquid jet source is in the style developed by Faubel[56] and is unchanged from our previous work.[53] Iodide is introduced to solution by dissolving potassium iodide (100 mM, EMD, ≥99% purity) in methanol (Fischer, Optima 0.2 μm filtered). This solution is then injected into vacuum at high backing pressure (80 atm) through a fused silica capillary (20 μm orifice diameter). The flow rate for all methanol experiments is held at 0.33 mL/min.

The jet is crossed with a sequence of two or three laser pulses following either Eq. (1) or (2). In the two pulse experiment, the CTTS band of the iodide anion is excited with $h\nu_1$ (238 nm, 5.2 eV), and the generated electrons are detached with $h\nu_2$ (266 nm, 4.67 eV, 125 fs). To generate a time-resolved spectrum, Δt_{12}, the delay between $h\nu_1$ and $h\nu_2$, is systematically varied in order to monitor the ensuing dynamics. In the three pulse experiments, electrons are generated with $h\nu_1$ (238 nm, 5.2 eV), excited with $h\nu_2$ (800 nm, 1.54 eV, 75 fs), and interrogated with $h\nu_3$ (266 nm, 4.67 eV, 125 fs). Δt_{12}, is held fixed at 200 ps so that only fully equilibrated electrons are excited.[22] Δt_{23} is varied, and a photoelectron spectrum is taken at each delay.

Photodetached electrons are sampled through a 500 μm skimmer to a second differentially pumped region containing a microchannel plate (MCP) detector. Typical operating pressures in the interaction and detection regions of our vacuum chamber are $3.7x10^{-4}$ Torr and $1.6x10^{-6}$ Torr, respectively. Photoelectrons are energy analyzed by time-of-flight in a magnetic bottle,[57] which offers greatly improved collection efficiency over a field-free time-of-flight analyzer. A 1.1 T steering magnet (B in Fig. 5.1) and 10 G solenoidal field within the flight tube direct the trajectories of the ejected photoelectrons toward the detector, allowing in principle for ~50% of generated photoelectrons to be collected. Photoelectron flight times are measured by recording the capacitively coupled current off of the phosphor screen as a function of time. This raw photoelectron time of flight spectrum is then converted to electron kinetic energy (eKE) and scaled by the appropriate Jacobian transformation. For ejected photoelectrons in the kinetic energy range expected for this experiment, 1-3

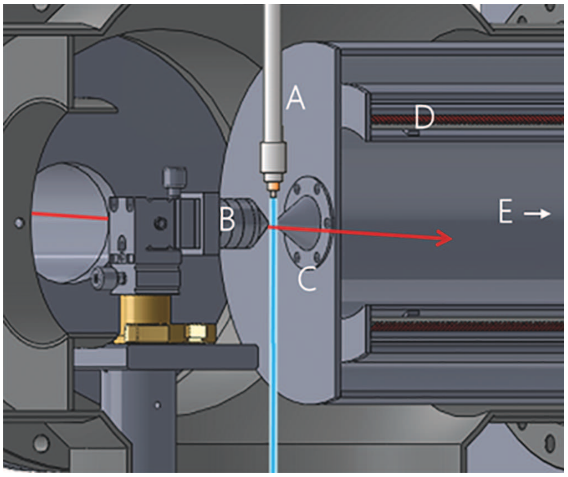

Figure 5.1: Main chamber of liquid microjet photoelectron spectrometer. The liquid jet (A) is crossed with a sequence of laser pulses (red arrow) that generate photoelectrons. Electrons are steered by a 1.1 T magnet (B) through a 500 μm skimmer (C) and then drift through the 10 Gauss solenoid (D) toward the detector (E).

eV, the electron escape depth from the surface of the microjet is a few nanometers[58–60]. Calibration and measurement of the streaming potential associated with the microjet are based on the method developed by Suzuki[10] and are as described in our previous paper.[53]

A Spectra Physics Spitfire laser system comprising a Ti:Sapphire oscillator and regenerative amplifier (2.2 W, <75 fs) is used to generate all ultrafast pulses. Half of the fundamental is used to pump a Light Conversion TOPAS, and the 238 nm CTTS excitation pulse is generated by frequency-doubling the sum frequency of the signal (1175 nm) and NIR pump (800 nm). The 266 nm detachment pulse is generated from the tripled fundamental. Due to bandwidth losses from generating the UV pulses, the pulse duration of the UV beams is lengthened relative to the 800 nm fundamental. The temporal resolution in the three-pulse experiments, 115 fs as defined by the near IR/UV cross correlation ($h\nu_2$ and $h\nu_3$), is therefore much shorter than in the two-pulse experiments, 220 fs, which is determined by the cross-correlation of the two UV beams. These values are given as the average single pulse duration, defined as the full width half maximum of the cross correlation divided by $\sqrt{2}$.

Data are analyzed via two methods: by simple integration of the total signal in specified energy lanes, and by a global fit assuming no spectral line shape but exponential time dynamics. This global fitting method,[61, 62] often referred to as global lifetime analysis (GLA), allows for simultaneous fitting of the entire time resolved data set which may help separate spectral contributions from overlapping features. GLA is predicated on two assumptions. First, it is assumed that the data consists of a sum of spectral components, each of which is separable into two parts: the spectrum of the component, $S_j(eKE)$, which depends only on kinetic energy, and the kinetics, $S_i(\Delta t)$, which depends only on pump-probe delay. This is expressed mathematically in Eq. (5.3) with each component in the sum scaled by the relative photodetachment cross section, σ_r, and where the sum is indexed by the number of spectral components j. Second, the kinetics are assumed to take the form of sums of monoexponentials (ex. $S(\Delta t) = Ae^{-k_1 t} - Be^{-k_2 t}$). If both assumptions are true, the data can be represented as a sum of exponentials scaled by a constant which depends on energy, called the decay associated spectrum (DAS) [62], and indexed by the time constants $\tau_i = 1/k_i$, Eq. (5.4).

$$S(eKE, \Delta t) = \sum_{j=1}^{n} \sigma_{r,j} S_j(eKE) S_j(\Delta t) \tag{5.3}$$

$$S(eKE, \Delta t) = \sum_{i=1}^{m} DAS_{\tau_i}(eKE)[e^{z/\tau_i} \cdot L(z - \Delta t)](\Delta t) \tag{5.4}$$

Physically, assuming energy and time are separable implies that the components do not shift on the same scale of time that they change in intensity. If this assumption is incorrect, more kinetic components than are physical will be necessary to fit the data. Analysis of the data using a method that allows for spectral shifts is detailed in the supplemental material.

To generate a fit, the spectral and temporal dimensions of background subtracted, time resolved photoelectron spectra are fit simultaneously by assuming a minimal number of kinetic rate constants, such that the three dimensional data (energy, delay, and intensity) is fit to Equation (3b) with residuals on the order of our signal to noise. The amplitude, $DAS_{\tau_i}(eKE)$, of each exponential in each energy lane is allowed to float but the rate constants, the width of the instrument response function $L(\Delta t)$, and the zero delay time are held as a single set of fit parameters for the entire data set. The DAS are quite different from the $S_i(eKE)$'s, the delay independent spectra of the species of interest. The DAS merely gives the scale of the coefficient in front of a particular exponential in the sum at a particular energy. The shape of each DAS can be used to predict a kinetic model which can then be used to reconstruct the $S_j(eKE)$'s.

5.3 Results

5.3.1 Two-Pulse Experiment

Time resolved photoelectron spectra using a 238 nm pump and 266 nm probe pulse were recorded at pump-probe delays up to 800 ps. Spectra following the background subtraction scheme $(h\nu_1 + h\nu_2) - h\nu_1 - h\nu_2$ are presented in Figure 5.2. Figs. 5.2a and 5.2b show the photoelectron (PE) spectra over all measured delays and over short delays, respectively. Slices

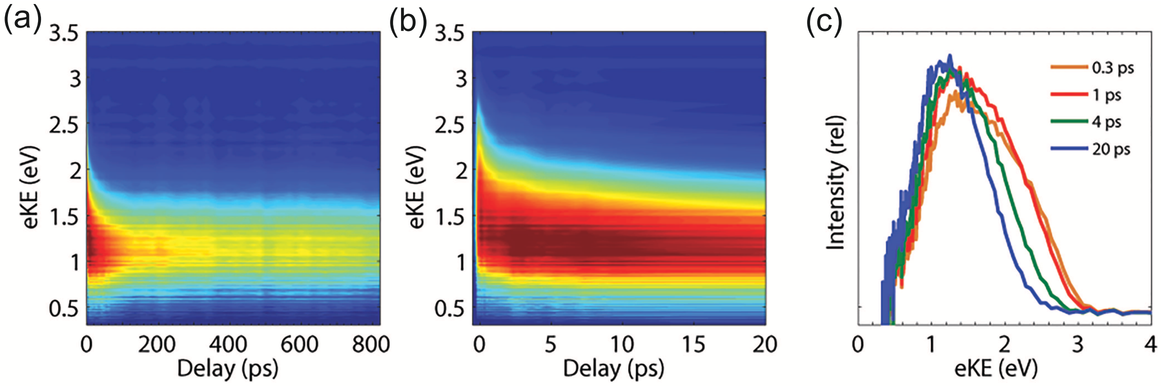

Figure 5.2: TRPE spectra of methanol subsequent to CTTS excitation over two energy ranges: -1 ps to 800 ps (a) and from -1 ps to 20 ps (b). Selected spectra at various delays (c).

through Fig. 5.2a at selected delay times are shown in Fig. 5.2c. Near t_0, the PE spectrum is nearly 2 eV wide, as exemplified in the spectrum at 0.3 ps in Fig. 5.2c. The data show a clear decay in the eKE range of 2.5 - 3.0 eV on a time scale of hundreds of femtoseconds. After this fast decay, the PE spectra are singly peaked near 1.2 eV at all delays. The PE spectrum then shifts and narrows on a few picosecond timescale. Spectral evolution appears to be complete by approximately 20 ps, after which the remaining signal decays to a steady intensity on a timescale of tens of picoseconds. The equilibrated vertical binding energy (VBE), as characterized by the peak of the binding energy spectrum beyond 20 ps, is found to be 3.4 eV ($h\nu_2 - eKE_{max}$), which is in good agreement with values reported previously for the ground state solvated electron in methanol.[54, 55]

Figure 5.3 shows plots of the integrated photoelectron intensity over the entire range of measured delays (Fig. 5.3a) and at delays less than 20 ps (Fig. 5.3b). The black curves in Figs. 5.3a and 5.3b show the integrated intensity across all electron energies, while the blue and red curves are integrated over the eKE ranges of 2.5 - 3.0 eV and 0.5 - 1.0 eV, respectively. The black curve is well fit with a triexponential decay with lifetimes of 480 $\pm$ 40 fs, 45 $\pm$ 3 ps, and $\sim$ 4 ns, with the last decay continuing well past the fitted region. We do not find a more sophisticated functional form to be necessary to fit this data. The blue curve rises with the cross-correlation and decays bi-exponentially with decay constants of 480 $\pm$ 40 fs and 7.4 $\pm$ 0.5 ps. The red curves, representing the low eKE edge of the observed signal, are fit with a cross-correlation limited rise time convoluted with an 8 $\pm$ 1 ps rise and a 45 $\pm$ 3 ps decay. Within our time resolution, nearly 80% of the population between 0.5 - 1.0 eV appears at zero pump-probe delay. The rest is generated from the 7 - 8 ps component. Hence, the fast (blue) signal appears to decay to the slower (red) signal on a time-scale of 7 - 8 ps.

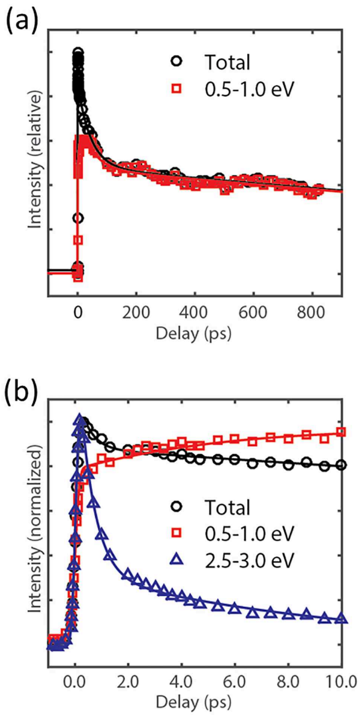

Figure 5.3: Integrated intensity at long pump-probe delays (a) and shorter pump-probe delays (b) for the total photoelectron intensity and band extrema.

The presence of overlapping features can lead to errors in lifetimes extracted from lane integration due to contamination by neighboring spectral components. Global lifetime analysis, as described in the previous section, can be used to extract accurate lifetimes of overlapped spectral features with differing temporal characteristics. The raw two-pulse data, fit and residuals are shown in Figures 5.4a-c. The data are fit using Eq. (5.4) with time constants of 550 ± 110 fs, 8 ± 3 ps, and 41 ± 7 ps, along with a $\sim$4 ns component that survives past the fitted region. The nanosecond lifetime is much longer than our window of measured delays and thus has significant error. The decay associated spectrum (DAS_{k_i}) for each kinetic component calculated from the fits is shown in Fig. 5.4d. A positive going DAS is associated with a feature that decays and a negative going DAS is associated with a feature which rises. Vertical lines in the residuals are caused by noise in the delay space caused by poorer sampling in this dimension.

The three time constants extracted from GLA are in reasonable agreement with lifetimes extracted from lane integration. The DAS of the nanosecond component and the 41 ps decay, which are very similar to one another, reproduce the ground state solvated electron spectrum. The 41 ps and 4 ns time constants from GLA match the long-time decay of the total signal, i.e. the black curve in Fig. 5.3. The DAS of each of the two faster kinetic components shows some decay of a weakly bound (high eKE) feature and a corresponding rise of ground state signal. This trend suggests an exchange of population between the two portions of the spectrum on this timescale. DAS_{8ps} does not deplete the total integral, as the integrated intensity of the DAS is zero within error, but has only a small negative going peak and therefore largely contributes to the fast decay of the total integral by depleting the weakly bound population of photoelectrons.

Because of the assumed separability between spectral and temporal components inherent to GLA, if there is a spectral shift on a similar timescale to the decay of a particular component, GLA gives a somewhat limited picture of the dynamics associated with that component. As a better treatment of the shifting feature, we can use the data from GLA to propose a model that explicitly allows for a shift in one or more features. In the supplemental information[63], we consider the data to comprise of two components, each of which is allowed to shift. We demonstrate that the data is adequately fit by a model with a weakly bound feature that decays without spectral evolution and a second strongly bound feature that shifts on an 8 ps timescale. This analysis is in accord with the model presented in the main text.

5.3.2 Three-Pulse Experiments

The three-pulse experiments follow the excitation scheme in Eq. (5.2). Electrons are generated via CTTS, photoexcited after a 200 ps delay to allow for equilibration, and finally detached to vacuum. The photoelectron spectra at various delays between $h\nu_2$ and $h\nu_3$ are plotted in Figs. 5.5a and 5.5b using two background subtraction schemes, as employed in previous work.[12] The two UV photons, $h\nu_1$ and $h\nu_3$, each contribute a static two-photon photodetachment signal from iodide, which we treat as background. Fig. 5.5a shows results following the background subtraction method $(h\nu_1 + h\nu_2 + h\nu_3) - h\nu_1 - h\nu_3$. The data show a large feature near 1.2 eV eKE and a feature at higher eKE, highlighted in blue, which appears near t_0 and decays shortly thereafter. The feature at 1.2 eV is depleted as the transient feature in the blue lane appears and then recovers on a longer timescale to its initial intensity. The VBE, defined as previously, of the feature at 1.2 eV eKE is 3.4 eV and is readily identified as the ground state of solvated electrons in methanol from prior work and the results in Section IIIA.[52, 54, 55]

A second background subtraction method, shown in Fig. 5.5b, more clearly illustrates the evolution of the PE spectra on the high eKE shoulder of the ground state. When the spectrum without the pump pulse, $h\nu_2$, is subtracted from the three color spectrum, $(h\nu_1 + h\nu_2 + h\nu_3) - (h\nu_1 + h\nu_3)$, the pump-induced transient appears as positive-going and the depleted initial state as negative-going. These difference spectra more clearly demonstrate how the signal changes in the presence of $h\nu_2$. As shown in Fig. 5.5b, the high energy shoulder of the positive-going signal, 3.0 - 3.3 eV eKE, decays on a $\sim$100 fs timescale, and the lower eKE portion of the positive going transient, 2.0 - 2.3 eV, decays on a significantly

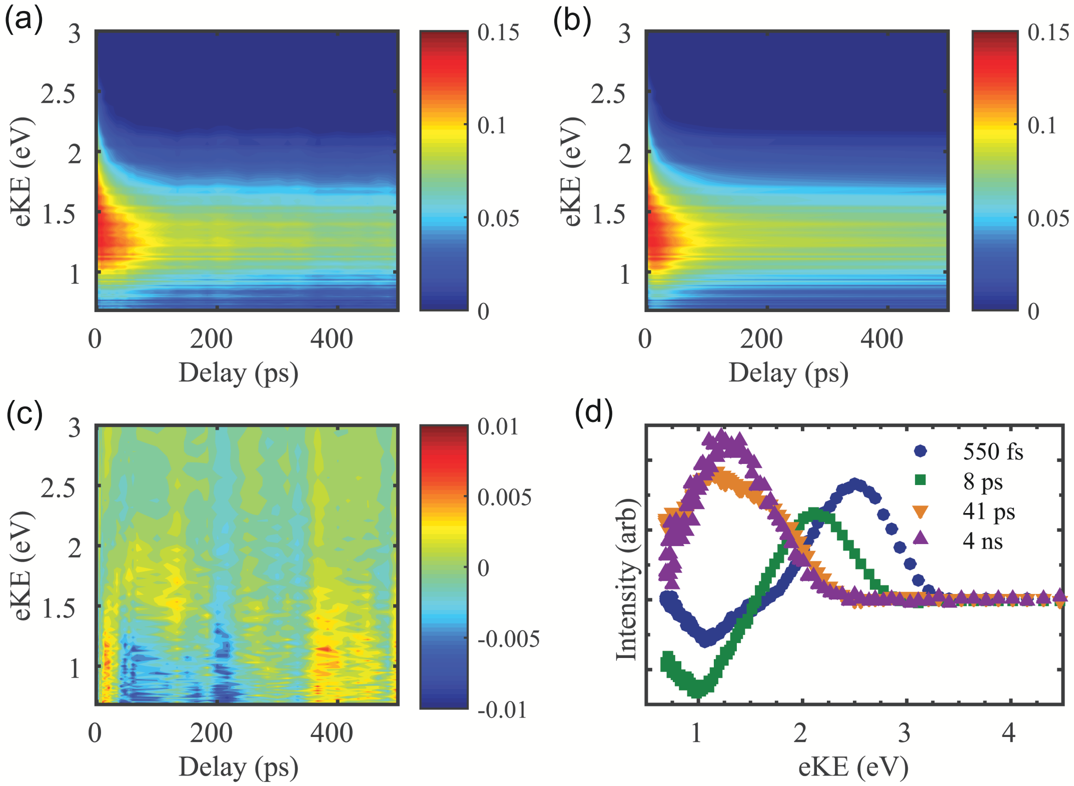

Figure 5.4: TRPE spectra for the two color experiment following the subtraction method $(h\nu_1 + h\nu_2) - h\nu_1 - h\nu_2$: CTTS solvation data (a), four component GLA fit (b), fit residuals magnified x6 (c), and DAS (d).

longer time scale of several hundred fs, during which time it also appears to shift toward lower eKE. The signal in this energy range is designated in red and is indicated in Fig. 5.5a.

Plots of the integrated intensity of the signal as a function of time in the regions of interest highlighted in Figure 5.5a are shown in Figure 5.5c. Integrated intensity in the blue energy lane appears within the cross correlation of the laser and decays on a time scale of 125 ± 50 fs. Above 3.0 eV eKE, the choice of integration region does not alter the lifetime of the blue lane; it thus appears this feature does not shift and that there is little overlap with any longer lived features in this integration lane. Integration between 2.0 eV and 2.3 eV eKE yields a lifetime of 690 ± 100 fs; however, this lifetime varies between ~850 fs and ~550 fs for 0.1 eV lanes between 1.9 and 2.4 eV. This variation may be due to spectral shifting in this region and significant spectral contamination of the integration region due to overlap of the features in the region. Integration of the ground state spectrum is made difficult to fit by noise at low eKE in our spectra; however, depletion and recovery of the ground state

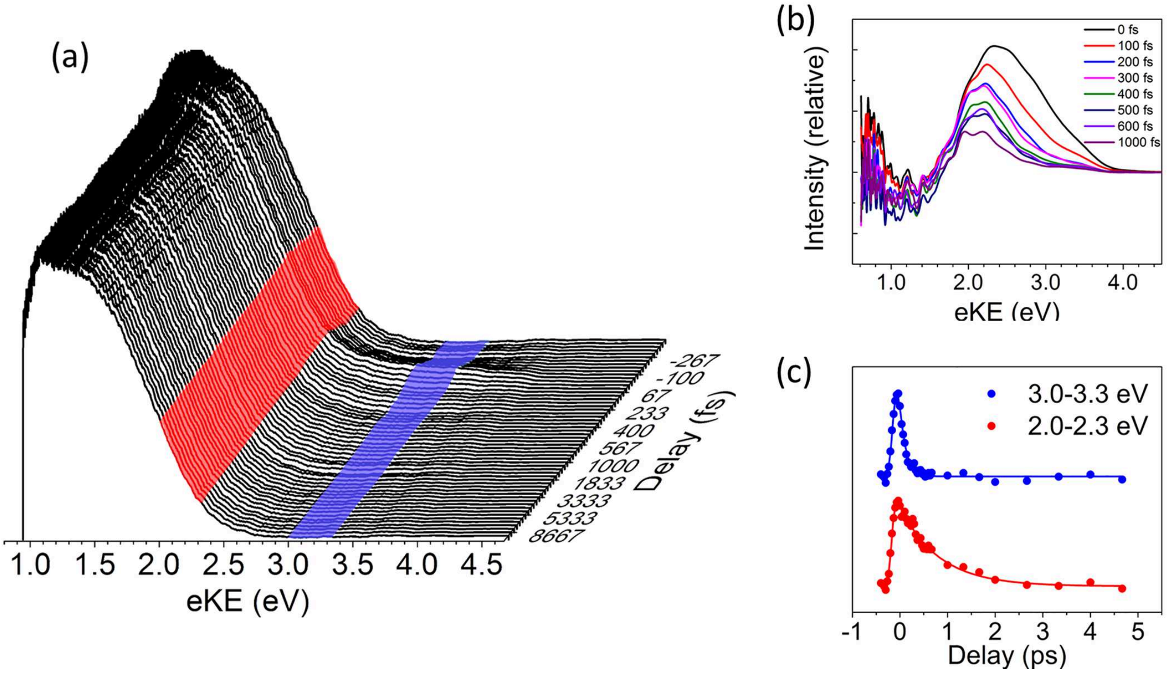

Figure 5.5: TRPE spectra following two background subtraction methods (a). $(h\nu_1 + h\nu_2 + h\nu_3) - h\nu_1 - h\nu_3$, and (b). $(h\nu_1 + h\nu_2 + h\nu_3) - (h\nu_1 + h\nu_3)$. 5 (c) shows integrated intensity vs. time in two regions of interest.

near zero pump-probe delay is clearly visible in Figs. 5.5a and 5.5b.

In order to better separate the spectral contributions from each of the three features, GLA is used to globally fit the entire data set. The raw data, fit, and residuals are pictured in Figures 5.6a, 5.6b, and 5.6c respectively. The two kinetic parameters as generated from the fit are 130 ± 40 fs and 800 ± 300 fs, which reproduce both lifetimes from lane integration to within error bounds. Decay associated spectra are generated for both kinetic components and are pictured in Figure 5.6d. DAS_{130fs} shows two positive going peaks: one centered at 2.7 eV and one at 1.2 eV. DAS_{800fs} has a positive component at 2.1 eV and a negative component at 1.2 eV that approximately mirrors the 130 fs component.

Analysis of the shape of each DAS can provide significant insight into the kinetics of the data being fit. A DAS with positive- and negative- going components suggests an exchange of population from the positive-going feature to the negative-going on the associated timescale. In this case, photoelectron intensity in the region of the red lane, from Fig. 5.5a, exchanges with the ground state on an 800 fs timescale. Interpretation of the two positive-going peaks in DAS_{130} is less obvious. The first peak is in the region of the blue lane and the second in the region of the red lane. In order to relate the DAS to the underlying dynamics, relations

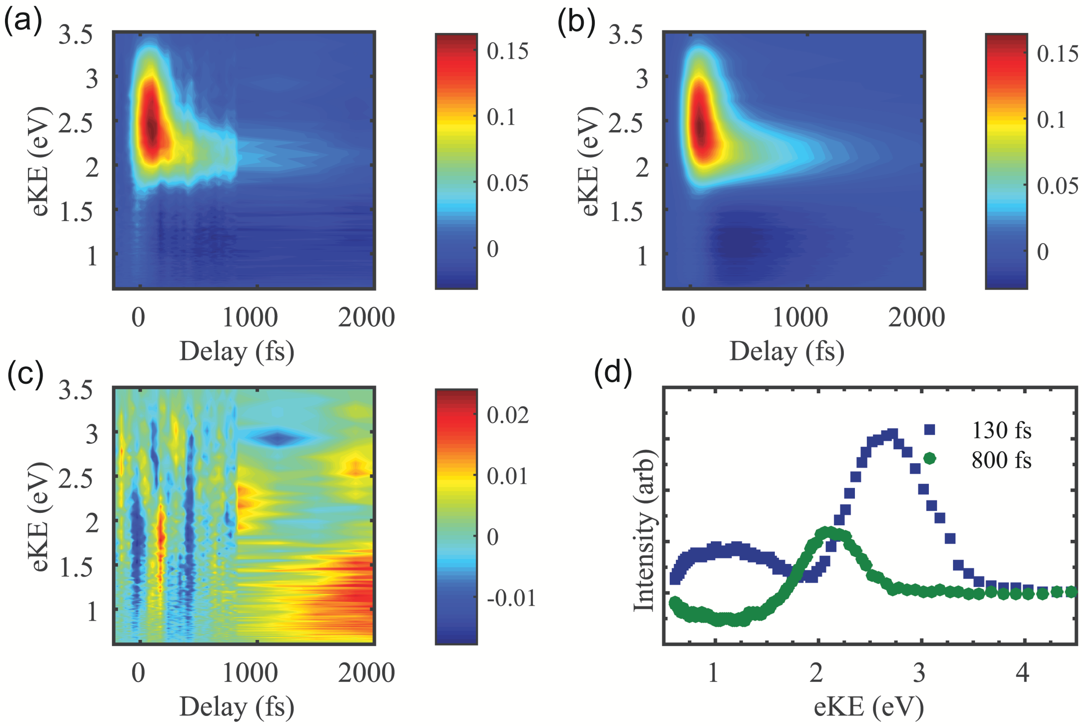

Figure 5.6: GLA fit of the three color experiment showing positive going features in green to red and negative in dark blue: data (a), fit (b), residuals (c), DAS (d).

between the DAS and the static kinetic energy distributions $S_j(eKE)$ can be derived by setting Eq. 5.3a equal to Eq. 5.3b and invoking an explicit kinetic model to generate the expressions for the integrated rate equations, $S_i(\Delta t)$. The simplest case for this is a three step sequential kinetic mechanism ($I \xrightarrow{\tau_1} II \xrightarrow{\tau_2} III$). With the initial condition $I+II+III = 0$, $S_{III}(\Delta t)$ for this mechanism is:

$$S_{III}(\Delta t) = \frac{A_0}{\tau_1 - \tau_2}[\tau_1 e^{-t/\tau_1} - \tau_2 e^{-t/\tau_2}]. \tag{5.5}$$

Assuming $I \xrightarrow{\tau_1} II \xrightarrow{\tau_2} III$ kinetics, expressions relating the DAS_{τ_1} to the spectral components $S_j(eKE)$ are given by Eqs. 5.5a and 5.5b:

$$DAS_{\tau_1} = S_I(eKE) - \frac{\tau_2}{\tau_2 - \tau_1}\sigma_{r,II} S_{II}(eKE) + \frac{\tau_1}{\tau_2 - \tau_1}\sigma_{r,III} S_{III}(eKE) \tag{5.6}$$

$$DAS_{\tau_2} = \frac{\tau_2}{\tau_2 - \tau_1}\sigma_{r,II} S_{II}(eKE) - \frac{\tau_2}{\tau_2 - \tau_1}\sigma_{r,III} S_{III}(eKE) \tag{5.7}$$

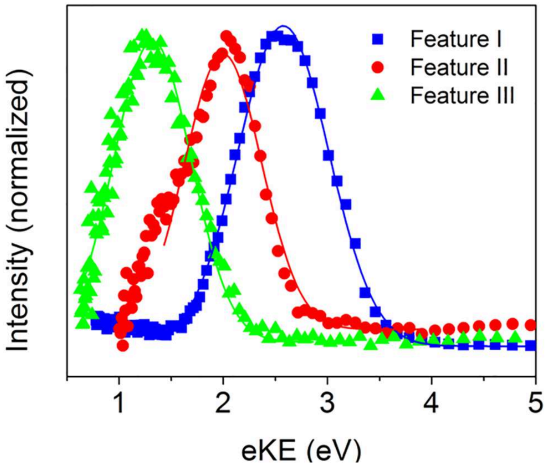

Figure 5.7: Spectra associated with Features I, II and III generated from analysis of the DAS and the known ground state, $DAS_{\tau_1}(eKE)$, and $DAS_{\tau_2}(eKE)$.

We see that DAS_{τ_2} has a positive-going component corresponding to S_{II} and a negative-going component S_{III}. DAS_{τ_1} has positive-going components S_I and S_{III} but negative-component S_{II}. By simply solving for S_I and S_{II} using DAS_{τ_1}, DAS_{τ_2}, and the known S_{III}, spectra for Features I and II are generated. These spectra are shown in Figure 5.7. Feature I peaks at 2.6 eV eKE and has a full width at half maximum of 1.0 eV. Feature II peaks at 2.0 eV and comprises the high energy tail of the main peak in Fig. 5.5a.

Comparing the extracted spectra for Features I and II in Fig. 5.7 with the integration lanes in Fig. 5.5a, we see that the spectra in Fig. 5.7 encompass the integration lanes in Fig. 5.5a. The portion of the extracted spectrum of Feature I which is not spectrally contaminated, i.e. which does not overlap Feature II, is the integration lane for the blue lane. In the absence of a spectrally pure integration lane, the region of highest intensity of the spectrum of Feature II corresponds to the red integration lane. Hence, the energy lanes in Fig. 5.5a, though considerably narrower than the spectral components in Fig. 5.7, pick up the same dynamics as the extracted spectra from global analysis. GLA is thus an equivalent but more complete representation of the underlying dynamics.

5.4 Discussion

5.4.1 CTTS Dynamics

The two-pulse TRPES experiments probe solvation dynamics of the electrons generated by CTTS excitation. The overall picture of these dynamics is believed to comprise several steps: [2, 36, 37] (i) decay of the optically accessible CTTS state to a "contact pair", in which the I atom and electron are confined within the same solvent shell, (ii) evolution of the contact pair to an equilibrium configuration with the surrounding solvent molecules, and (iii) diffusion of the free solvated electron away from the iodine to form a solvent separated electron, which competes with geminate recombination to re-form the I^- anion. Based on previous work, we divide the dynamics into two parts: ejection and cavity formation dynamics in the short time regime, $<$ 20 ps (steps i and ii), and recombination dynamics in the long time regime, $>$ 20 ps (step iii).

While Vilchiz et al.[34] previously studied the CTTS dynamics of iodide in methanol with TA, their work focused on equilibration of the solvated electron and geminate recombination dynamics. Our results probe these steps along with earlier time dynamics. TRPES has been used to study the CTTS process from iodide in water,[10, 11, 13] which provides a strong point of comparison to our results. Also of interest to this discussion are TA experiments of solvated electrons in neat methanol generated by photoionization of the solvent molecule [39, 64, 65]. Although the photoionization scheme in these experiments generate electrons with substantially greater initial energy than in CTTS experiments, they do provide a reference point for solvation times.

5.4.1.1 Short time dynamics

The total photoelectron signal (black curve, Fig. 5.2) and the signal in the high eKE energy lane spanning 2.5-3.0 eV (blue curve, Fig. 5.2) rise within the laser pulse cross correlation time and exhibit fast decay constants of 480 ± 40 fs. GLA yields a DAS spanning 2.0-3.0 eV that decays in 550 ± 110 fs (Fig. 5.4d). It is reasonable to conclude that these fast time constants reflect the same process, which results in rapid depletion of photoelectron signal at high eKE but relatively little rise at low eKE.

Previously published TRPES studies in water microjets identify a 190 - 210 fs lifetime associated with the decay of a weakly bound hydrated electron population[10, 11, 13]. This lifetime is both similar in magnitude and approximate energy range to our 550 fs lifetime in methanol; therefore, we expect these Features to be directly comparable between solvents. Early time CTTS dynamics in water have been studied in a number of laboratories. Fast dynamics on the order of 200 fs are observed in TA, in the form of a rise time in the hydrated electron absorption [22, 33]. In methanol, a rise time for TA data is also reported to be present but a lifetime for the rise is not provided.[34] In time resolved fluorescence monitoring the decay of the iodine fluorescence signal in water, a two-step relaxation of 60 fs and 100 - 400 fs is reported.[66] Finally, using time-resolved x-ray absorption to probe the 2s-5p absorption in aqueous iodine subsequent to CTTS excitation, Galler and co-workers[66] observe a rise time of 80 fs for the neutral iodine absorption but no subsequent decay over a time scale of several hundred femtoseconds.

In water, the few-hundred fs timescale has been variously attributed to the decay of the relaxed CTTS state,[67] trapping of an iodide electron contact pair state from the CTTS state, and recombination of the electron with the iodide. In TRPES in water, Tang et al[10, 13] assigned their observed ∼200 fs timescale to the decay of the CTTS state, which branches to both form the contact pair and recombine with the parent iodine. Lubcke et al.[11] attributed this feature exclusively to a fast recombination of the "hot" electron with the geminate iodine but allowed the possibility of a fast evolution of the photoelectron cross section. However, the absence of a ∼200 fs decay in the iodine transient absorption data[66] provides rather convincing evidence that there is no recombination on this timescale. Therefore, assuming that the fast dynamics seen in methanol have the same origin, we conclude that the apparent decrease in the integrated photoelectron intensity is due to a rapid change in the photodetachment cross section due to evolution of the CTTS state to a solvated electron configuration.

The second lifetime extracted from the data, 6 - 8 ps, is seen as the longer decay component of the blue curve in Fig. 5.2b and the rise time of the red curve in the same panel. Based on the eKE ranges of the two curves, 2.5-3.0 eV and 0.5-1.0 eV, these dynamics appear to reflect exchange between the population on the weakly bound edge of the ground state spectrum with the equilibrated ground state, i.e. relaxation of the solvated electron. A similar 8 ± 3 ps timescale is observed in GLA corresponding to a DAS with decaying population centered at 2.0 eV and rising at 0.9 eV. No picosecond decay of the total signal (black curve, Fig. 5.2) is observed; supporting the assignment of these dynamics to solvent relaxation and not population decay.

The lifetimes for the ground state relaxation generated from lane integration and GLA, 6.0 ± 1.5 ps and 8 ± 3 ps respectively, are in reasonable agreement despite the presence of spectral shifting. There is a clear shifting behavior in the few picosecond regime as shown in Fig. 5.2b, and the residuals from GLA are highest in this region. As noted previously, shifting behavior is not well treated by GLA, and we expect significant error bounds in this lifetime. A second fitting routine which allows for spectral shifts is discussed in the supplemental material and agrees well with the few picosecond timescale from GLA and lane integration.

In methanol, similar timescales to our 8 ps thermalization have been reported for decay of the "hot" ground state electron from TA following methanol photoionization.[39, 64, 65] After CTTS excitation, Vilchiz et al.[34] found the spectral evolution of the solvated electron to be complete within 20 ps, in overall accord with our results. In water, Lubcke et al.[11] found an approximately one picosecond shift of the "hot" electron population and a corresponding sub-picosecond decay which they attributed to a fast recombination of the "hot" electron with the geminate iodine. Also in water, Tang et al.[10] identified a 1.3 ps timescale which they associated with an exchange between two intermediate solvation states centered at 200 meV and 20 meV above the ground state. The general trend for these solvation times show methanol and ethanol relaxing 3-4 times slower than water. An 8 ps solvation time for the solvated electron in methanol is therefore quite reasonable in light of prior results.

5.4.1.2 Long Time Dynamics

After $\sim$20 ps, the population between 0.5 and 1.0 eV eKE (red curve in Fig. 5.3a) decays on a 41 ps timescale to a stable intensity for the rest of the window of measured pump-probe delays. The DAS for the nanosecond and 41 ± 7 ps kinetic components each reproduce the relaxed ground state. Both kinetic components are also seen in the decay of the total photoelectron signal, the black curve in Fig. 5.3a. Therefore, we can conclude that the 41 ps component represents a uniform depletion of the ground state photoelectron population.

In methanol, Vilchiz et al.[34] have approached the recombination problem from a number of avenues of increasing sophistication. They conclude that the total decay of the absorption signal is best fit with the numerical model allowing for an attractive potential between pairs rather than using a sum of exponentials; however, we found their simpler "competing kinetics" model to be adequate.[22] In this model, the longtime behavior is represented by a branched mechanism balancing diffusive pair dissociation, k_d, and non-adiabatic (geminate) recombination with the parent, k_n. Though both the iodine-electron solvent-separated pair and the free solvated electron have the same spectrum, the geminate recombination rate can be estimated from the surviving fraction of electrons, $k_d/(k_d + k_n)$. Assuming this kinetic model and that both species have equivalent photodetachment cross sections, the fraction of electrons that survive geminate recombination is 0.71, from which we calculate $k_d = 1/(57ps)$ and $k_n = 1/(146ps)$. Vilchiz et. al. find the fractional survival of electrons using the competing kinetics model to be 0.7. The 41 ps lifetime from our DAS analysis is equivalent to $1/(k_d + k_n)$. Using their exponential components to calculate a comparable rate constant yields 35 ps, which is in reasonable agreement with our reported lifetime of 41 ± 7 ps.

In water, a similar time constant was measured in TRPES experiments monitoring the CTTS excitation from iodide. Both Suzuki and coworkers[10, 13] and Lubcke et al.[11] measured a $\sim$20 ps decay of the total photoelectron signal. Lubcke assigned this process to geminate recombination. Suzuki and coworkers calculate a pair diffusion lifetime of 84 ps and a recombination lifetime of 28 ps. Further, their study indicated that the decay affects a population of electrons very near the ground state binding energy, in agreement with our findings in methanol.

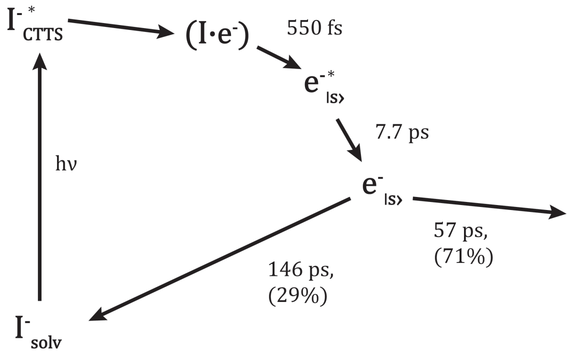

Figure 5.8: Summary of charge-transfer-to-solvent dynamics from I^- to methanol after 238 nm excitation. The dynamics include: a fast evolution of the photodetachment cross section, thermalization of the electron, and competitive diffusion and recombination of the relaxed electron.

A summary of the solvation scheme is presented in Figure 5.8. After CTTS excitation, electrons are formed in a range of configurations in relative proximity to the geminate iodide. The earliest process measurable with our time resolution is the 550 ± 110 fs decay of a weakly bound population. This decay is likely due to decay of the relaxed CTTS state to a solvated electron configuration and is accompanied by a decrease in the photodetachment cross section. The solvated electron spectrum then shifts toward the equilibrated spectrum on an 8 ± 3 picosecond timescale as excess energy is redistributed into the solvent modes. Dynamics after this point do not affect the binding energy spectrum and consist solely of a decrease in the solvated electron population to a stable long term value. The lifetime of the decay of the total population is 41 ± 7 ps. 71% of generated solvated electrons survive geminate recombination, and thus presumably become free solvated electrons. The geminate recombination lifetime, assuming branched exponential kinetics, is 146 ps and the pair diffusion lifetime, 57 ps.

5.4.2 Excited State Dynamics

The relaxation mechanism of the solvated electron after excitation to its *p*-state is expected to comprise three steps, as summarized in Figure 5.9: relaxation on the excited state, τ_P, internal conversion to the ground state, τ_{IC}, and solvent relaxation on the ground state, τ_S. Prior work on this system has been conducted by a number of groups using TA in methanol.[38, 39] From these experiments, three lifetimes were extracted ∼100fs, ∼700fs, and 5-6 ps, but conclusive assignment of these lifetimes to a particular physical process has been a matter of some debate.[6] The relaxation process is expected to follow one of two proposed mechanisms[20]. In the adiabatic mechanism, τ_P is expected to occur on a ∼100 fs timescale, τ_{IC} occurs on a ∼700 fs timescale, and τ_S on a few picosecond timescale. In the non-adiabatic mechanism, τ_{IC} occurs on a ∼100 fs timescale, and the longer time constants

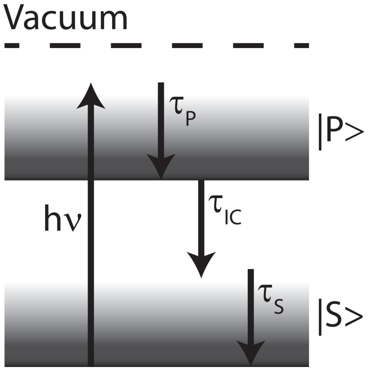

Figure 5.9: Schematic relaxation mechanism for the solvated electron subsequent to electronic excitation.

involve solvent relaxation after internal conversion.

As was the case with water, the two mechanisms can be distinguished by pinning down the internal conversion lifetime. From the perspective of the work presented here, resolving this issue depends on the assignment of Features I and II in the three-pulse experiments in Fig. 5.7. If Feature I is the unrelaxed *p*-state and II is the relaxed *p*-state, then the mechanism is best described as adiabatic, but if Feature II is best assigned to the ground state, then the relaxation mechanism is non-adiabatic. We note that features analogous to I and II were seen in our three-pulse experiments on water liquid jets; the latter assignment in favor of the non-adiabatic mechanism was made there.[12]

Similar arguments are invoked herein. Features I and II in Fig. 5.7 overlap but their maxima differ by 0.6 eV. Comparison of the red energy lane in Fig. 5.5a and Feature II in Fig. 5.7 shows that the 800 fs relaxation affects a population on the hot edge of the ground state feature as would be expected from *s*-state relaxation. As mentioned in reference to Fig. 5.5b, the pump-induced signal, shown in the curves from 200 - 600 fs, does appear to be shifting toward lower electron kinetic energy. Such a shift could also explain the relatively large error bars on the 800 fs lifetime extracted from GLA. A shift is suggestive of electrons in a non-equilibrated solvent environment, as would be expected for *s*-state electrons just after internal conversion. Conversely, electrons in the blue lane do not appear to shift, as evidenced by the independence of the fitted lifetime from integration lane; therefore, it is not likely the result of a shift on the excited state. Finally, if 800 fs was the internal conversion time, we would expect to observe some ground state solvation on a longer timescale; however, we find no evidence for a 5-6 ps lifetime within our 10 ps observation window. Therefore, it is logical to assign Feature I to the *p*-state and its lifetime to internal conversion. The internal conversion lifetime of the solvated electron is then 130 ± 40 fs, as extracted from GLA. The spectrum of Feature I as shown in Fig. 5.7 is centered at 2.57 eV eKE, yielding a vertical binding energy of 2.1 eV for the *p*-state. The lifetime of the "hot" *s*-state, Feature II, is 800 fs.

Our value of 130 fs for the internal conversion lifetime and 800 fs for the ground state relaxation lifetime are in good agreement with the reported values of 105 ± 25 fs and 670 ± 100 fs by Thaller et. al.[39] They narrowed the assignment of the 670 fs relaxation to either the internal conversion lifetime or ground state relaxation. Silva et al.[38] also performed TA studies of the equilibrated solvated electron in methanol. They report an internal conversion lifetime of ∼300fs; however, this discrepancy may be due to the limitations of their 300 fs time resolution, which would have made the first time constant unresolvable.

The values and assignments reported here are also in good agreement with extrapolated results from solvent cluster anions (157 ± 25 and 760 ± 25 fs)[50]. It is interesting to note that the extrapolated results from clusters produce reasonable lifetimes considering the extrapolated ground state binding energy of 2.6 eV[68] is well off the measured value of 3.38 eV[54] in the bulk. It has been speculated that the phase of these methanol clusters may more closely resemble solids than liquids[69]. In light of the difference from the predicted binding energy, the correspondence between the extrapolated lifetime and the bulk measurement requires future consideration.

We next turn to a comparison of the results here to those measured in water. The solvated electron in water was shown by TRPES to sequentially undergo internal conversion and relaxation on the ground state on 75 ± 25 and 410 ± 100 fs timescales respectively[12]. Methanol shows identical excited state dynamics to water, albeit at a slower rate by nearly a factor of two for both solvents. Our results are in qualitative agreement with the results of Borgis et. al.[70] who predict non-adiabatic transition times of $< 160fs$ depending on the model. The 150 fs internal conversion time in methanol predicted by Zharikov and Fischer[45] also agrees well with our reported value, as it similarly does in water.

5.5 Conclusion

In the two pulse experiment, the solvated electron generated from CTTS excitation in methanol undergoes similar dynamics to the hydrated electron. The earliest dynamics include contact pair formation followed by ultrafast depletion of a weakly bound electron population centered at 2.4 eV eKE with a lifetime of 550 ± 110 fs, which we attribute to rapid evolution and decay of the CTTS state. The photoelectron spectrum then shifts on an 8 ± 3 ps timescale to the ground state solvated electron spectrum. Two exponential decays are necessary to fit the data: an ultrafast decay of 550 ± 110 fs, which exclusively depletes the weakly bound population and which we assign to decay of the CTTS state to a solvated electron accompanied by rapid decrease in the photodetachment cross section, and a longer 41 ±7 ps time constant which depletes the ground state population. Solvated electrons survive well past the measured delays. Approximately 70% of the ground state signal survives the 41 ps recombination step. Using the surviving electron fraction and the 41 ps decay, we find a 57 ps pair diffusion lifetime and 146 ps geminate recombination lifetime.

From the three pulse experiments, relaxation of the excited *p*-state electron in methanol is attributed to the non-adiabatic mechanism. Global lifetime analysis yields spectra associated with the *p*-state and hot *s*-state of the solvated electrons, yielding internal conversion and ground state relaxation timescales of 130 ± 40 fs and 800 ± 300 fs respectively. This interpretation is in accord with measurements in water. The lifetimes of both solvation processes are shown to be in agreement with results from TA, and the internal conversion lifetime agrees with extrapolated results from methanol cluster anions.

Acknowledgements

This work was funded by the National Science Foundation under grant CHE-1361412 and by the Air Force Office of Scientific Research as part of Multidisciplinary University Research Initiative #9 award number 24086151-06. The data presented here are available on request sent to dneumark@berkeley.edu.

References

5.6 References

[1] B. C. Garrett, D. A. Dixon, D. M. Camaioni, D. M. Chipman, M. A. Johnson, C. D. Jonah, G. A. Kimmel, J. H. Miller, T. N. Rescigno, P. J. Rossky, S. S. Xantheas, S. D. Colson, A. H. Laufer, D. Ray, P. F. Barbara, D. M. Bartels, K. H. Becker, K. H. Bowen, S. E. Bradforth, I. Carmichael, J. V. Coe, L. R. Corrales, J. P. Cowin, M. Dupuis, K. B. Eisenthal, J. A. Franz, M. S. Gutowski, K. D. Jordan, B. D. Kay, J. A. LaVerne, S. V. Lymar, T. E. Madey, C. W. McCurdy, D. Meisel, S. Mukamel, A. R. Nilsson, T. M. Orlando, N. G. Petrik, S. M. Pimblott, J. R. Rustad, G. K. Schenter, S. J. Singer, A. Tokmakoff, L.-S. Wang, and T. S. Zwier, Chem. Rev. **105**, 355 (2005).

[2] X. Y. Chen and S. E. Bradforth, Annu. Rev. Phys. Chem. **59**, 203 (2008).

[3] B. Abel, Annu. Rev. Phys. Chem. **64**, 533 (2013).

[4] R. M. Young and D. M. Neumark, Chem. Rev. **112**, 5553 (2012).

[5] P. J. Rossky and J. Schnitker, J. Phys. Chem. **92**, 4277 (1988).

[6] L. Turi and P. J. Rossky, Chem. Rev. **112**, 5641 (2012).

[7] M. Faubel, B. Steiner, and J. P. Toennies, J. Chem. Phys. **106**, 9013 (1997).

[8] B. Winter and M. Faubel, Chem. Rev. **106**, 1176 (2006).

[9] K. R. Siefermann, Y. X. Liu, E. Lugovoy, O. Link, M. Faubel, U. Buck, B. Winter, and B. Abel, Nature Chemistry **2**, 274 (2010).

[10] Y. Tang, Y.-i. Suzuki, H. Shen, K. Sekiguchi, N. Kurahashi, K. Nishizawa, P. Zuo, and T. Suzuki, Chem. Phys. Lett. **494**, 111 (2010).

[11] A. Lübcke, F. Buchner, N. Heine, I. V. Hertel, and T. Schultz, Phys. Chem. Chem. Phys. **12**, 14629 (2010).

[12] M. H. Elkins, H. L. Williams, A. T. Shreve, and D. M. Neumark, Science **342**, 1496 (2013).

[13] K. Suzuki, Y. Ohmori, and E. Ratel, Plant Cell Physiol. **52**, 1697 (2011).

[14] E. J. Hart and J. W. Boag, J. Am. Chem. Soc. **84**, 4090 (1962).

[15] F.-Y. Jou and G. R. Freeman, J. Phys. Chem. **81**, 909 (1977).

[16] J. Schnitker, K. Motakabbir, P. J. Rossky, and R. A. Friesner, Phys. Rev. Lett. **60**, 456 (1988).

[17] A. Migus, Y. Gauduel, J. L. Martin, and A. Antonetti, Phys. Rev. Lett. **58**, 1559 (1987).

[18] X. Shi, F. Long, H. Lu, and K. Eisenthal, J. Phys. Chem. **99**, 6917 (1995).

[19] Y. Kimura, J. C. Alfano, P. K. Walhout, and P. F. Barbara, J. Phys. Chem. **98**, 3450 (1994).

[20] K. Yokoyama, C. Silva, D. H. Son, P. K. Walhout, and P. F. Barbara, J. Phys. Chem. A **102**, 6957 (1998).

[21] A. Hertwig, H. Hippler, A. N. Unterreiner, and P. Vohringer, Berichte Der Bunsen-Gesellschaft-Physical Chemistry Chemical Physics **102**, 805 (1998).

[22] J. A. Kloepfer, V. H. Vilchiz, V. A. Lenchenkov, A. C. Germaine, and S. E. Bradforth, J. Chem. Phys. **113**, 6288 (2000).

[23] A. Thaller, R. Laenen, and A. Laubereau, Chem. Phys. Lett. **398**, 459 (2004).

[24] M. J. Tauber and R. A. Mathies, J. Am. Chem. Soc. **125**, 1394 (2003).

[25] C. M. Stuart, M. J. Tauber, and R. A. Mathies, J. Phys. Chem. A **111**, 8390 (2007).

[26] F. H. Long, X. L. Shi, H. Lu, and K. Eisenthal, J. Phys. Chem. **98**, 7252 (1994).

[27] J. Frank and G. Scheibe, Zeitschrift Fur Physikalische Chemie A **139**, 22 (1928).

[28] M. J. Blandamer and M. F. Fox, Chem. Rev. **70**, 59 (1970).

[29] J. Jortner, M. Ottolenghi, and G. Stein, J. Phys. Chem. **68**, 247 (1964).

[30] V. H. Vilchiz, J. A. Kloepfer, A. C. Germaine, V. A. Lenchenkov, and S. E. Bradforth, J. Phys. Chem. A **105**, 1711 (2001).

[31] J. A. Kloepfer, V. H. Vilchiz, V. A. Lenchenkov, X. Y. Chen, and S. E. Bradforth, J. Chem. Phys. **117**, 766 (2002).

[32] J. A. Kloepfer, V. H. Vilchiz, V. A. Lenchenkov, and S. E. Bradforth, Chem. Phys. Lett. **298**, 120 (1998).

[33] H. Iglev, A. Trifonov, A. Thaller, I. Buchvarov, T. Fiebig, and A. Laubereau, Chem. Phys. Lett. **403**, 198 (2005).

[34] V. H. Vilchiz, X. Chen, J. A. Kloepfer, and S. E. Bradforth, Radiat. Phys. Chem. **72**, 159 (2005).

[35] W.-S. Sheu and P. J. Rossky, J. Phys. Chem. **100**, 1295 (1996).

[36] A. Staib and D. Borgis, J. Chem. Phys. **104**, 9027 (1996).

[37] S. E. Bradforth and P. Jungwirth, J. Phys. Chem. A **106**, 1286 (2002).

[38] C. Silva, P. K. Walhout, P. J. Reid, and P. F. Barbara, J. Phys. Chem. A **102**, 5701 (1998).

[39] A. Thaller, R. Laenen, and A. Laubereau, J. Chem. Phys. **124**, 024515 (2006).

[40] B. J. Schwartz and P. J. Rossky, J. Chem. Phys. **101**, 6902 (1994).

[41] B. J. Schwartz and P. J. Rossky, J. Chem. Phys. **101**, 6917 (1994).

[42] K. Fueki, D. F. Feng, and L. Kevan, Chem. Phys. Lett. **10**, 504 (1971).

[43] P. Mináry, L. Turi, and P. J. Rossky, J. Chem. Phys. **110**, 10953 (1999).

[44] A. A. Mosyak, O. V. Prezhdo, and P. J. Rossky, J. Chem. Phys. **109**, 6390 (1998).

[45] A. A. Zharikov and S. F. Fischer, J. Chem. Phys. **124**, 054506 (2006).

[46] J. Zhu and R. I. Cukier, J. Chem. Phys. **98**, 5679 (1993).

[47] T. Suzuki and B. J. Whitaker, Int. Rev. Phys. Chem. **20**, 313 (2001).

[48] A. Stolow, A. E. Bragg, and D. M. Neumark, Chem. Rev. **104**, 1719 (2004).

[49] A. E. Bragg, J. R. R. Verlet, A. Kammrath, O. Cheshnovsky, and D. M. Neumark, Science **306**, 669 (2004).

[50] A. Kammrath, G. B. Griffin, J. R. R. Verlet, R. M. Young, and D. M. Neumark, J. Chem. Phys. **126**, 244306 (2007).

[51] D. M. Neumark, Mol. Phys. **106**, 2183 (2008).

[52] H. Shen, N. Kurahashi, T. Horio, K. Sekiguchi, and T. Suzuki, Chem. Lett. **39**, 668 (2010).

[53] A. T. Shreve, T. A. Yen, and D. M. Neumark, Chem. Phys. Lett. **493**, 216 (2010).

[54] A. T. Shreve, M. H. Elkins, and D. M. Neumark, Chemical Science **4**, 1633 (2013).

[55] T. Horio, H. Shen, S. Adachi, and T. Suzuki, Chem. Phys. Lett. **535**, 12 (2012).

[56] M. Faubel, S. Schlemmer, and J. P. Toennies, Zeitschrift Fur Physik D **10**, 269 (1988).

[57] P. Kruit and F. H. Read, Journal of Physics E: Scientific Instruments **16**, 313 (1983).

[58] F. Buchner, T. Schultz, and A. Lubcke, Phys. Chem. Chem. Phys. **14**, 5837 (2012).

[59] S. Thürmer, R. Seidel, M. Faubel, W. Eberhardt, J. C. Hemminger, S. E. Bradforth, and B. Winter, Phys. Rev. Lett. **111**, 173005 (2013).

[60] Y.-i. Yamamoto, Y.-I. Suzuki, G. Tomasello, T. Horio, S. Karashima, R. Mitríc, and T. Suzuki, Phys. Rev. Lett. **112**, 187603 (2014).

[61] I. H. M. van Stokkum, D. S. Larsen, and R. van Grondelle, Biochim. Biophys. Acta **1657**, 82 (2004).

[62] J. R. Knutson, D. G. Walbridge, and L. Brand, Biochemistry (Mosc.) **21**, 4671 (1982).

[63] See Supplemental Materials .

[64] P. K. Walhout, J. C. Alfano, Y. Kimura, C. Silva, P. J. Reid, and P. F. Barbara, Chem. Phys. Lett. **232**, 135 (1995).

[65] C. Pepin, T. Goulet, D. Houde, and J. P. Jay-Gerin, J. Phys. Chem. **98**, 7009 (1994).

[66] A. Galler, (Private Communication, 2015).

[67] F. Messina, O. Bräm, A. Cannizzo, and M. Chergui, Nat Commun **4**, 2119 (2013).

[68] A. Kammrath, J. R. R. Verlet, G. B. Griffin, and D. M. Neumark, J. Chem. Phys. **125**, 171102 (2006).

[69] R. M. Forck, I. Dauster, U. Buck, and T. Zeuch, J. Phys. Chem. A **115**, 6068 (2011).

[70] D. Borgis, P. J. Rossky, and L. Turi, J. Chem. Phys. **125**, 064501 (2006).

5.7 Supplemental Material

5.7.1 Global Lifetime Analysis Implementation

General Ideas and Assumptions

First assume that each spectral component is separable into two parts: one which depends only on energy and the other which depends only on pump-probe delay. Physically, this means that the spectra do not shift on the same timescale over which they change in intensity. This idea is expressed mathematically below, where sigma is the relative photodetachment cross section:

$$S(eKE, \Delta t) = \sum_{j=1}^{n} \sigma_r S_j(eKE) S_j(\Delta t) \tag{5.8}$$

Second, assume that the data obeys exponential kinetics. The intensity of the features as a function of time then behave as sums of exponentials. Ex: $[A(t)] = Ae^{-k_1 t} - Be^{-k_2 t}$. Based on this assumption, the data can be represented as sums of mono-exponentials (convoluted with the instrument response function) with coefficients that depend on energy.

$$S(eKE, \Delta t) = \sum_{i=1}^{m} DAS_{\tau_i}(eKE)[e^{z/\tau_i} \cdot L(z - \Delta t)](\Delta t) \tag{5.9}$$

The coefficients of each exponential for each component are referred to as the Decay Associated Spectrum (DAS). These are quite different from the $S_j(eKE)$'s, the fixed delay spectra of the species of interest. The DAS merely gives the scale of the coefficient in front of a particular exponential in the sum at a particular energy.

3rd given these two assumptions, globally fit the data to eqation (5.9) using a nonlinear least squares fitting routine. The optimized parameters are the rate constants, the amplitudes $DAS_i(eKE)$, time zero, the width of the cross correlation and a static offset. Care must be taken to assure that the data is fit with a minimum number of kinetic components.

Kinetic Analysis

Notice that at this point no kinetic mechanism has been assumed. While many systems can be quite complicated, the DAS for each component must be consistent with any kinetic model that is put forward. To generate $S_j(eKE)$ from the DAS, one must first assume a kinetic mechanism, for instance, $I \xrightarrow{\tau_1} II \xrightarrow{\tau_2} III$ with initial condition $I + II + III = 0$

as is presented in the main text.

$$S_I(\Delta t) = I_0 e^{-k_1 t} \tag{5.10}$$

$$S_{II}(\Delta t) = \frac{I_0 k_1}{k_1 - k_2}[e^{-k_2 t} - e^{-k_1 t}] \tag{5.11}$$

$$S_{III}(\Delta t) = \frac{I_0}{k_1 - k_2}[k_2 e^{-k_1 t} - k_1 e^{-k_2 t}] \tag{5.12}$$

The kinetic equations describing each state are then substituted for $S_i(\Delta t)$ and eqn. (5.8) is set equal to eqn. (5.9). Next, the DAS are solved for as a function of $S_j(eKE)$. The result for the three component rate is below.

$$DAS_{\tau_1} = S_I(eKE) - \frac{k_1}{k_1 - k_2}\sigma_{r,II} S_{II}(eKE) + \frac{k_2}{k_1 - k_2}\sigma_{r,III} S_{III}(eKE) \tag{5.13}$$

$$DAS_{\tau_2} = \frac{k_1}{k_1 - k_2}\sigma_{r,II} S_{II}(eKE) - \frac{k_1}{k_1 - k_2}\sigma_{r,III} S_{III}(eKE) \tag{5.14}$$

Note that the shape of each DAS has the same sign as the coefficient in front of the exponential in the corresponding kinetic equation. The sign of each part in the sum determines the sign of the shape of the DAS. DAS_{k_2} has a negative going part that looks like S_{III} and a positive going part that looks like S_{II}. Similarly, DAS_{k_1} has two positive going regions and one negative. The negative part is small k_1 is faster than k_2. Since the decay associated spectra are known from the fit, a known spectrum for S_{III} can be used to calculate S_I.

Error Analysis:

In order to report an error bound, we aimed to develop a confidence interval for the fitted lifetimes considering the impact of the other fit parameters. The method used here is referred to as Support Plane Analysis, but more generally it can be thought of as an F-test. In this analysis, the quality of a fit is judged by the F-statistic, which determines the values of the chi-squared distribution that are above an acceptable value for a given level of confidence (95% in this paper). The values of each variable for which chi squared is below that generated by the F-statistic yield a confidence interval which can then be used as error bounds.

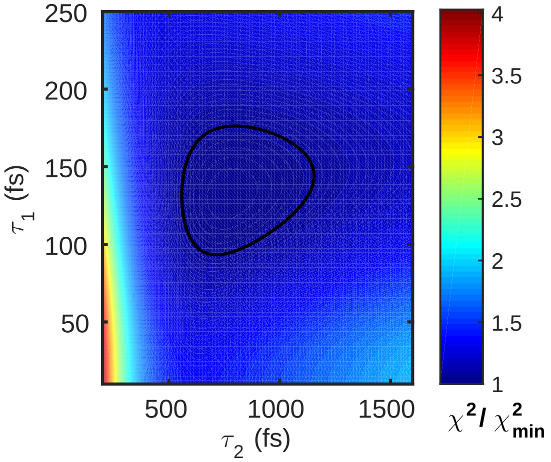

Figure 5.10: Test Chi-squared matrix for the three pulse data. The circle is the limit of the 95% confidence interval calculated from support plane analysis.

To conduct an F-test for a two rate constant global fit, the chi-squared for the best fit (χ^2_{min}) is first calculated. A vector of test lifetimes for each rate is then generated. For example, if the best fit lifetime is 140 fs, a vector of 100 values between 30 fs and 300 fs is generated. A least squares fit is conducted at each test value and the chi-squared value computed. For a two rate constant global fit, this is a matrix of test chi-squared values. The value of the F-statistic is calculated using the equation below where v_1 is the number of fitted parameters and v_2 is the number of degrees of freedom, χ. The degree of confidence, p, is a number between 0 and 1. Common values are 0.95 for 2σ and 0.32 for σ.

$$\frac{\chi^2_x}{\chi^2_{min}} = 1 + \frac{v_1}{v_2} F_{inv}(p|v_1, v_2) \tag{5.15}$$

The equation above returns a number greater than one. The plane defined by $\chi^2 = \chi^2_x$ intersects the matrix of test chi-squared values at the limits of the confidence interval. The figure below shows a contour plot of the test chi-squared matrix for the three pulse data. The loop inscribed is the limit of the 95% confidence interval. This method is generalizable to any number of lifetimes. For an arbitrary number of lifetimes, the rank of the tensor of test values is equal to the number of lifetimes and is always one rank greater than the confidence interval.

5.7.2 Shifting Global Fit:

General Ideas

While no chemistry must be strictly assumed for a GLA type analysis, in a second global fitting model we make some assumptions about the spectral landscape of the problem to gain a better understanding of the nature of spectral shifts. First, Gaussian line shapes have been assumed for all spectral features. This general line shape is seen in all previously published photoelectron spectra on solvated electrons and therefore seems reasonable for our model. The centers, x_i, and widths, w_i, of the Gaussians are allowed to shift with the same exponential time constant, $k_{c,i}$, which is a fit parameter in the model. In addition, each component is allowed to decay with $k_{d,i}$. The general functional form of the fits is below.

$$S(eKE,t) = \sum_{i=1}^{n} \frac{A_i}{w_i\sqrt{2\pi}} e^{-2\frac{\lambda - x_i}{w_i}^2} \int_{-\infty}^{\infty} e^{-k_{d,i}z} L(z-t)dz \tag{5.16}$$

$$w_i(t) = w_{i,\infty} + (w_{i,0} - w_{i,\infty})e^{-(t-t_0)k_{c,i}} \tag{5.17}$$

$$x_i(t) = x_{i,\infty} + (x_{i,0} - x_{i,\infty})e^{-(t-t_0)k_{c,i}} \tag{5.18}$$

Results from two color experiment

In order to better understand how shifting contributes to the dynamics, the data are fit using a model that explicitly allows for shifting of the various spectral features of interest. The spectrum in this time range is assumed to be composed of two shifting Gaussians, one weakly bound and one strongly bound, e^-_{wb} and e^-_{sb}. Both e^-_{wb} and e^-_{sb} are allowed to shift and narrow with time constants $t_{c,sb}$ and $t_{c,wb}$ according to equations (5.10) and (5.13). The weakly bound population, e^-_{wb} is allowed to decay with time constant $t_{d,wb}$. The fraction of the population of e^-_{wb} that populates the ground state is a fit parameter. The strongly bound population, e^-_{sb}, is populated at zero time and by e^-_{wb} and decays on time $t_{d,sb}$. Fits using a model that allows for three spectral features showed no significant improvement over the two state model; further, no single state model with multi-exponential shift parameters fully captures the dynamics above 2.5 eV eKE.

Despite imposing no constraint on e^-_{wb}, $t_{d,wb}$ was found to be 570 fs, and is many orders of magnitude shorter than $t_{c,wb}$, 600 ps. Therefore, it is unnecessary for e^-_{wb} to shift. The spectrum of e^-_{wb} is centered at 2.4 eV, which is consistent with the shortest time constant derived from GLA. The thermalization of the nascent electron population is instead entirely taken up by e^-_{sb}, which is found to shift 0.3 eV to the equilibrated ground state spectrum on a ∼8 ps timescale. Though the lifetime of e^-_{wb} found to be 570 fs, e^-_{sb} persists past the fitted region.

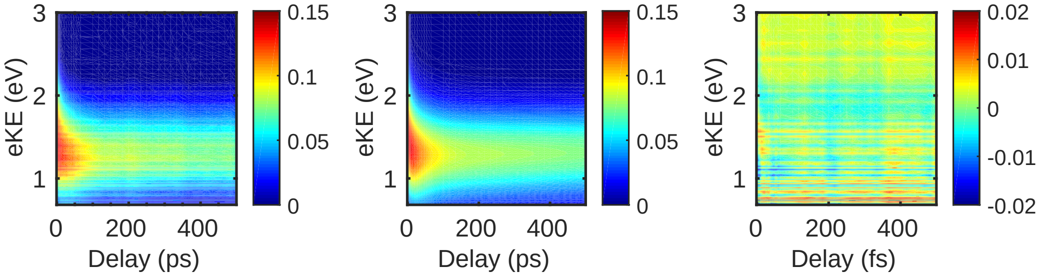

Figure 5.11: Global fit to the two pulse data allowing for spectral shifts: data (a), fit output (b), and residuals (magnified x5) (c).

Comparison to GLA

The bulk of the residuals in the fit are caused by a poor fit to the low electron kinetic energy portion of the spectrum, < 1 eV. The assumption of a spectral shape for this fit leads to horizontal bars in the residuals but relatively little other structure. This is due to the fact that the fit errors from the assumed kinetics are smaller than the error caused by assuming strictly Gaussian line shape. The magnitude of the error is no more than a factor of two worse than GLA. This fitting method best picks up the picosecond dynamics on the ground state due to solvation shift. While this particular fitting method is more physically motivated, in the absence of a better line shape, its utility is somewhat limited. The reported lifetime for the spectral shift is 8 ps from this method in comparison to 8 ps from GLA and 7.4ps from lane integration. Within our ability to fit the data, all fitting methods perform similarly well.

Chapter 6

Isotope Effect of the Internal Conversion Lifetime of Photoexcited Solvated Electrons in Water and Deuterium Oxide

M. H. Elkins, H. L. Williams, and D. M. Neumark. In preperation.

The excited state relaxation dynamics of the solvated electron in water and deuterium oxide are investigated using time-resolved photoelectron spectroscopy in a liquid microjet. The time-evolving photoelectron spectra shows evidence for an isotope effect of 1.3 ± 0.2 in the internal conversion lifetime of the hydrated electron following deuteration. Both H_2O and D_2O exhibit fast internal conversion lifetimes of <100 fs followed by a ∼400 fs lifetime characteristic of solvent relaxation on the ground state. These lifetimes are in agreement with prior work in transient absorption and the non-adiabatic mechanism.

6.1 Introduction

Hydrated electrons, free-electrons in water, were first identified in 1962 by their absorption spectrum at 720 nm by Hart and Boag[1]. Since then, electrons solvated in water and other solvents have been implicated in fields as far reaching as the photochemistry of DNA[2–4] to the nature of the coulomb explosion following the addition of sodium metal to water[5]. Because the solvated electron lacks internal degrees of freedom, it can be thought of as a model solute for studying solvation phenomena. Here, the electron is used both as a probe of solvation dynamics and the solute itself to study a fundamental process, solvent relaxation after electronic excitation of the solute. Specifically, the effect of isotopic substitution on the excited state dynamics of the hydrated electron is investigated using time-resolved photoelectron spectroscopy (TRPES) on liquid jets of H_2O and D_2O.

The spectrum of the solvated electron in water and deuterium oxide consists of an "*s*-like" ground state and a quasi-degenerate manifold of "*p*-like" excited states. The absorption band connecting these two bound states gives rise to the spectrum measured by Hart and Boag[1]. A wealth of prior experiments on the hydrated electron have used the evolution of this same band to study the ultrafast relaxation dynamics of the electron after generation by charge-transfer-to-solvent excitation[6–9] and subsequent to electronic excitation to the *p*-state[10–16].

In prior work, transient absorption (TA) has been to study the relaxation dynamics of the electron after *p*-state excitation[10–13, 15, 16]. In these experiments, three lifetimes were measured: <100 fs, 300-400 fs, and 1.1 ps. Similar results were also obtained in D_2O and yielded an isotope effect for the fast lifetime of 1.1 to 1.5[11, 15, 16]. Despite prior theoretical and experimental work on the subject, the assignment of these lifetimes is still contested[17].

Two general relaxation mechanisms have been proposed, the "adiabatic" and "non-adiabatic" mechanisms[11, 17]. In the adiabatic mechanism, the fastest lifetime is assigned to solvent relaxation on the excited state, τ_p. The 300-400 fs lifetime is assigned to internal conversion (IC) from the excited state to the ground state, τ_{IC}, and the 1.1 ps lifetime corresponds to solvent relaxation on the ground state, τ_s. In the "non-adiabatic" mechanism, the fastest lifetime is assigned to internal conversion, and both longer lifetimes are assigned to relaxation on the ground state.

Results from experiments using gas-phase solvent cluster anions provide additional insight into the relaxation dynamics of the solvated electron in the bulk[18, 19]. In anionic cluster experiments in water and D_2O, clusters of solvent molecules with an excess electron of increasing cluster size up to 200 are generated and studied using TRPES[20–27]. These experiments show a clear separation between the s and p states, allowing for conclusive identification of the internal conversion lifetime. In the cluster anion experiments, the IC lifetime was measured as a function of cluster size and then extrapolated to a bulk value of 63 fs in water and 160 fs in D_2O. This method has been repeated tested in our lab and others using measurements in liquid jets. Though extrapolation from clusters accurately predicts the IC lifetimes of water[28] and methanol[29] and the vertical binding energy (VBE) of water[30–34], the extrapolated solvated electron binding energy in methanol and acetonitrile are notably not well predicted. Experiments on solvated electrons in the liquid jets provide an important connection to this gas phase work.

Identification of the relaxation mechanism hinges on the assignment of the IC lifetime, which can be greatly aided by a measurement of the effect of isotopic substitution on the relaxation dynamics. An isotope effect was predicted in the internal conversion rate from theoretical work by Schwartz et. al.; however, the lack of an experimental isotope effect in the 300-400 fs lifetime in TA, which Schwartz et. al. assigned as the IC lifetime, was conspicuous[35]. Further, an isotope effect is found in the internal conversion lifetime in water and deuterium oxide cluster anions[21, 25]. A TRPES measurement of the relaxation dynamics of the solvated electron in D_2O would provide further insight and conclusive evidence as to the nature of the relaxation mechanism.

Here, solvated electrons in water and deuterated water are generated by charge-transfer-to-solvent (CTTS) excitation with a first photon[9]. The nascent photoelectrons are allowed to equilibrate with the solution, and after a 200 ps delay, a second photon excites the $s \rightarrow p$ absorption band of the solvated electron. At a variable delay, a third photon detaches the excess electron to vacuum, and the ensuing dynamics are monitored by measuring the binding energy of the electron as a function of delay $\Delta\tau_{23}$. The excitation scheme is summarized in Eq. 6.1.

$$I^-_{(aq)} \overset{h\nu_1,\Delta t_{12}}{\longrightarrow} I_{(aq)} + e^-_{(aq)}(s) \overset{h\nu_2,\Delta t_{23}}{\longrightarrow} e^-_{(aq)}(p) \overset{h\nu_3}{\longrightarrow} e^-_{(vac)} \tag{6.1}$$

The relaxation dynamics of solvated electrons in water and deuterated water upon $s \rightarrow p$ excitation are monitored using TRPES in a liquid microjet. Electrons in both solvents are found to relax non-adiabatically with internal conversion lifetime of 69 ± 11 fs for water and 96 ± 9 fs for deuterated water, a factor of 1.3 ± 0.2 longer. The excited state lifetime for water is in excellent agreement with both the cluster extrapolation and prior work from our group on water. Using TRPES, we present first measurement of the binding energy of the excited state of the solvated electron in D_2O. As in water, the excited state lifetime for D_2O is in agreement with results from transient absorption. Associated spectra are presented for solvated electrons in both solvents yielding excited state binding energies of ∼2.1 eV.

6.2 Methods

The liquid microjet photoelectron spectrometer used for these experiments has been described previously[29]. Briefly, a solution of potassium iodide (100mM, Fischer) in water (18 MΩ, Millipore) or deuterium oxide (99.98% Cambridge Isotope Laboratories) is injected at high backing pressure, 80-130 atm, through a 20 μm fused silica capillary in to vacuum. The flow rate is held at 0.33 mL/min for both water and heavy water, resulting in a jet velocity of ∼13 m/s. The liquid is then crossed with a series of femtosecond laser pulses following the excitation scheme in Eq. 6.1.

The final photon detaches the excess electron to vacuum, which is then sampled through a 900 μm skimmer. Photoelectrons are generated in these experiments with 1-3 eV of kinetic energy and have an escape depth of a few nanometers[36–38]. The photodetached electrons are energy-analyzed with a magnetic bottle consisting of a 1.1 Tesla SmCo magnet and a 10

Gauss solenoid. This technique allows for, in principle, a 50% collection efficiency of generated photoelectrons[30, 39].

The photoelectron signal is collected on a chevron stack of microchannel plates. Data is recorded in the form of the capacitively coupled current off of the detector as a function of time between the laser interaction with the jet and arrival at the detector. This time-of-flight is converted to electron kinetic energy (eKE), and the photoelectron intensity is scaled with the appropriate Jacobian transformation (t^{-3}). Calibration of the instrument and measurement of the streaming potential are as described in our previous paper[40].

Ultrafast pulses are generated from the 800 nm output from a commercial ultrafast system (Spectra Physics Spitfire, 2.2W, <75 fs). Approximately half the output is directed into an OPA (Light Conversion TOPAS). The second harmonic of the sum of the signal and pump is used to generate the tunable ultraviolet wavelength used for CTTS excitation (240nm, $h\nu_1$). The rest of the output from the femtosecond system is either used directly to form $h\nu_2$ (800 nm) or tripled to form the probe (266 nm, $h\nu_3$). Improvements to the optical layout since our previous work have allowed for a shorter cross-correlation at the chamber, 65 fs (Gaussian width) measured in the chamber.

The data analysis methods used here are described more fully in our previous paper[28]. Two methods are implemented. First, using global lifetime analysis (GLA), the entire time resolved data is iteratively fit using a minimal set of exponential kinetic components [41, 42]. Second, the integrated intensity in several regions of interest are fit as a function of delay to an exponential decay convoluted with the instrument response function, which is approximated by a Gaussian. GLA is implemented in order to help separate spectral contributions from overlapping features. Two sets of spectra extracted from global fitting are presented: first, the decay associated spectrum/spectra (DAS) for each kinetic component and, second, a reconstructed spectrum for the feature of interest. The DAS is the amplitude for each kinetic component as a function of kinetic energy and is an output from the fit. The extracted spectra are calculated from the DAS using a particular kinetic model.

6.3 Results

Following the excitation scheme in Eq. 6.1, a UV pulse at 240 nm, $h\nu_1$, is used to generate solvated electrons, and after a 200 ps delay, the electrons are excited with 800nm, $h\nu_2$, and detached to vacuum with 266 nm $h\nu_3$. Data were recorded at pump-probe delays, $\Delta\tau_{23}$, from -1 ps to 10 ps. The TRPE spectrum as a function of $\Delta\tau_{23}$ for D_2O is shown in Figure 6.1A and for H_2O is shown in Fig. fig:isotopefig1B. Both $h\nu_1$ and $h\nu_3$ contribute static, single color photoelectron intensity which is treated as background. Rather than subtracting the signal from each beam individually, the spectra in Fig. 6.1A and 6.1B show the spectra with and without $h\nu_2$, $(h\nu_1+h\nu_2+h\nu_3)-(h\nu_1+h\nu_3)$. These difference spectra show how the presence of

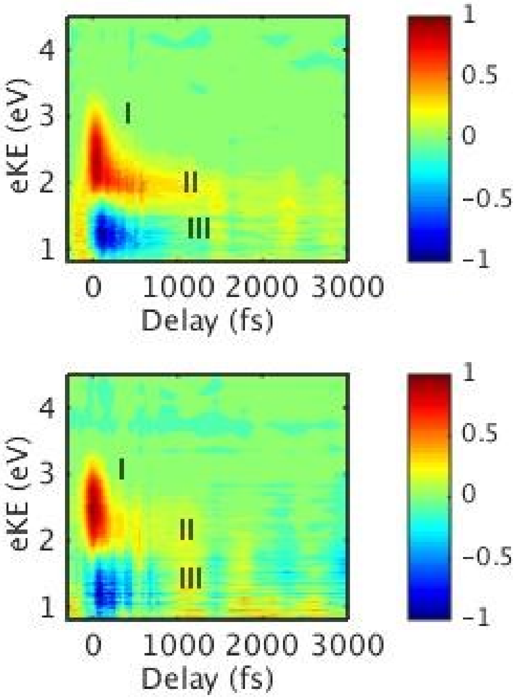

Figure 6.1: Time Resolved data for H_2O and D_2O following the subtraction method $(h\nu_1 + h\nu_2 + h\nu_3) - (h\nu_1 + h\nu_3)$. Three regions of interest are labeled. Red indicates increased intensity with hν2 and blue indicates decreased intensity.

$h\nu_2$ changes the spectrum. Features that are populated by excitation pulse are shown in red, features that are depleted are shown in blue, and green represents regions that are unchanged.

Each spectrum shows three main features numbered I to III from highest kinetic energy, I, to lowest kinetic energy, III. Region III, centered at 1.2V, is depleted at near $\Delta\tau_{23} = 0$ and recovers on a several hundred femtosecond timescale. The region of increased photoelectron intensity, shown in red, decays on two timescales, labeled I and II. The high eKE edge of the excited region, region I, decays significantly more quickly than the slower edge, region II. Finally, region II and region III appear to exchange on a similar timescale in both solvents.

The delay dependent dynamics are more clearly shown in fig. 6.2. Fig. 6.2A shows normalized plots of the integrated intensity in three regions of interest for D_2O. The specific choice of electron kinetic energy intervals for the three regions is discussed in Section 6.4. The decay of the blue curve, an integration on the high eKE edge of region I, is complete within the first hundred femtoseconds. The decay of the red curve, an integration of region II, is several hundred fs. A comparison of the green curve, the low eKE edge of region III,

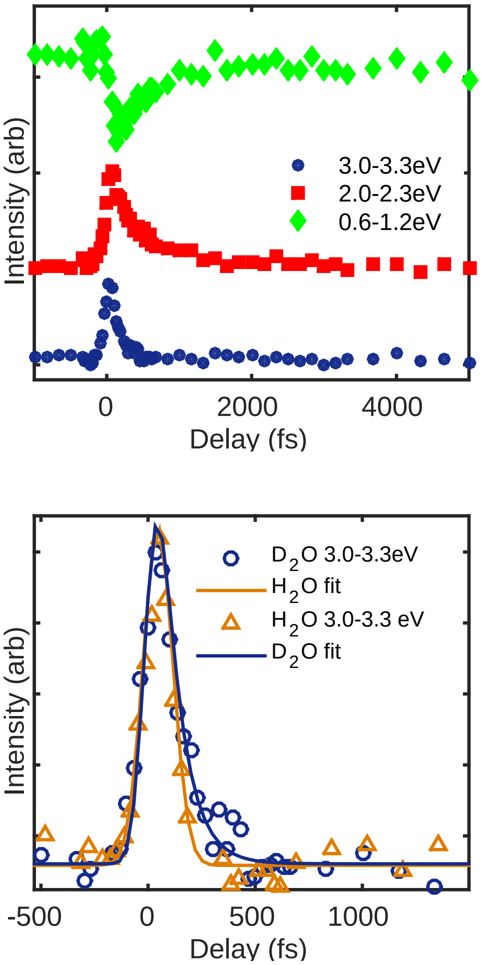

Figure 6.2: Integration of the TR spectra in selected energy lanes for both solvents. A, the three regions of interest for D_2O. B, a comparison of region I in H_2O and D_2O.

with the red curve clearly shows the exchange of II with III on a several hundred fs lifetime. These results are typical for both isotopes.

The change due to isotopic substitution is shown in fig. 6.2B. In these normalized integrated intensity plots, an equivalent spectral energy “lane” for region I is used in both solvents. The decay of region I in water, the gold curve, is noticeably faster than the decay of feature I in D_2O, the blue curve. Details of the fitting procedure to both curves are described in Section 6.4. The decay dynamics of region II are somewhat less obvious. The lifetime generated from a fit to the integrated intensity of region II depends strongly on the choice of the energy region. This effect was observed in water, D_2O, and in methanol[29].

Without further interpretation, we can understand the dynamics in Figure 6.1 in the following manner. The depletion of III represents the pump-induced depletion of the initial state. In water and heavy water, this feature is identified as a depletion of the ground state photoelectron intensity. This assignment is made based upon prior work in water and by the characteristic vertical binding energy (VBE) of the hydrated electron, 3.4 eV[30, 33, 34], where $h\nu_3 - eKEmax = VBE$. Similarly, the ground state VBE in deuterated water is known to be 3.47 eV[34]. The decay of regions I and II reflect the relaxation of the population excited after the pump pulse as it repopulates the ground state. Though these phenomena have been discussed previously in water[28] and in methanol[29], the new results presented here include more detailed spectral analysis of the TR data, discussed in Sec. 6.4, and the isotope effect on the internal conversion dynamics, Sec. 6.5.

6.4 Analysis

In order to gain a more quantitative understanding of the time resolved data, two general data analysis methods are employed, Global Lifetime Analysis (GLA)[41, 42] and fitting of the time-dependent integrated intensity of regions highlighted in Figure 6.2. The latter presents a simpler method of data analysis with few fit parameters; however, the method suffers when multiple features overlap in the same spectral region. GLA has proven to be particularly advantageous for decomposing the spectral contributions from overlapping features in congested spectra. This allows for a spectral identification of the features, but the method suffers in the presence of dynamic spectral shifts, which are typical of solvent relaxation processes[43]. Here, both methods provide complementary information on the TR data.

The fit, residuals, and decay associated spectra generated from global lifetime analysis of the D_2O time-resolved data is shown in Fig. 6.3B-D. In D_2O, two kinetic components are found to fit the spectra, 80 ± 30 fs and 380 ± 90 fs. DAS features that are positive going are associated with features that decay and features that are negative going are associated with features that rise. DAS_{80fs} shows two peaks: one centered at 0.9 eV eKE and one at 2.5 eV eKE. The peak at 0.9 eV is readily identifiable as the ground state spectrum from prior work[34]. DAS_{380fs} also has two peaks, one positive and one negative. The H_2O data shows similar trends but with slightly different lifetimes <75 fs and 420 ± 90 fs. The shape of DAS_{380fs} suggests that population is directly exchanging from the positive going feature to the negative going feature. The negative going feature mirrors that from DAS_{80fs} and is also readily identifiable as the ground state.

In order to interpret DAS_{80fs}, one must consider possible mechanisms that might contribute two peaks to the spectrum. In an appropriate kinetic model with these DAS, the integrated rate equation for feature III must contain e^{-t/τ_1} with a positive leading coefficient. The simplest possible mechanism that includes this condition is a three-step sequential kinetic mechanism. In the case of a sequential mechanism, the integrated rate law for feature

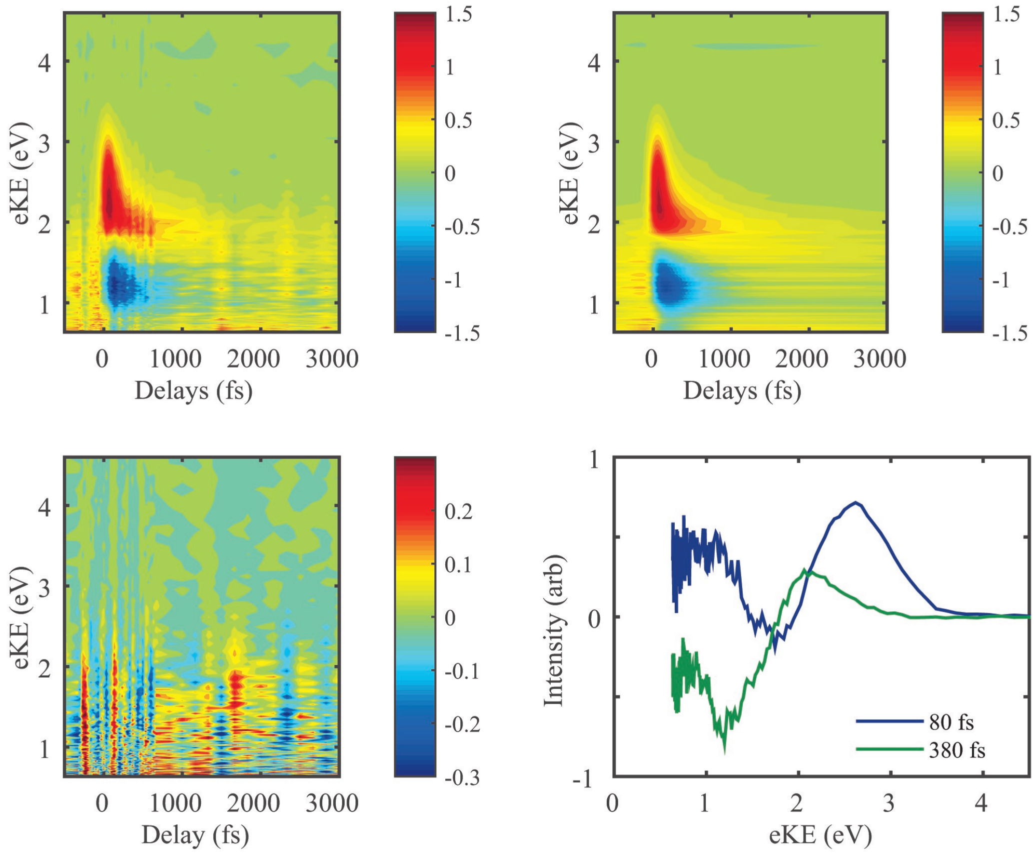

Figure 6.3: Global lifetime analysis of D_2O data. A, raw TR data. B, global fit. C, residuals. D, decay associated spectra.

III is $S_{III}(\Delta t) = \frac{A_0}{\tau_2 - \tau_1}\left[\tau_1 e^{-t/\tau_1} - \tau_2 e^{-t/\tau_2}\right]$. Assuming these kinetics, an expression for the predicted DAS for each kinetic component can then be calculated.

For a $I \xrightarrow{\tau_1} II \xrightarrow{\tau_2} III$ kinetic model with initial condition $I + II + III = 0$, expressions relating the DAS to the associated spectrum of the feature are given by Eqs. 6.2 and 6.3:

$$DAS_{\tau_1} = S_I(eKE) - \frac{\tau_2}{\tau_2 - \tau_1}\sigma_{r,II}S_{II}(eKE) + \frac{\tau_1}{\tau_2 - \tau_1}\sigma_{r,III}S_{III}(eKE) \tag{6.2}$$

$$DAS_{\tau_2} = \frac{\tau_2}{\tau_2 - \tau_1}\sigma_{r,II}S_{II}(eKE) - \frac{\tau_2}{\tau_2 - \tau_1}\sigma_{r,III}S_{III}(eKE) \tag{6.3}$$

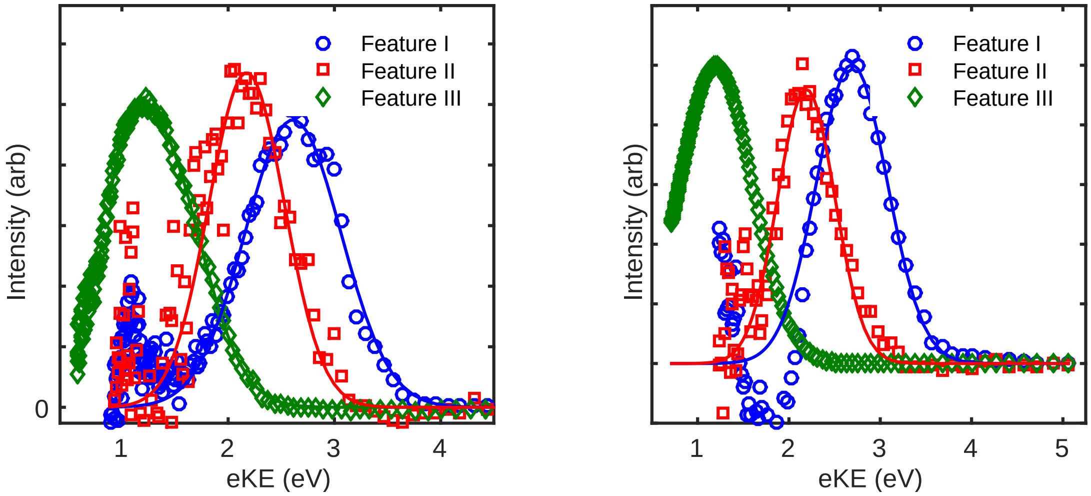

Figure 6.4: Extracted spectra for Features I, II, and III in water and heavy water.

As shown in Equation 6.2, DAS_{τ_2} has a positive going component associated with feature II and a negative going component associated with feature III. Also, DAS_{τ_1} contains positive going components associated with feature I and III. Using the equations above, spectra for features I and II can be generated by solving for S_{II} and S_{III} using the DAS from the fit and the known ground state. For both solvents, these spectra are shown in Figure 6.4. The extracted spectra for both solvents show very similar spectra. In D_2O, the ground state, feature III, is found to have a VBE of 3.38 ± 0.05, and in H_2O, this feature has a VBE of 3.40 ± 0.05 eV. Feature I has a VBE of 2.1 ± 0.2 in heavy water and in water. Feature III shows little overlap with feature I. Feature II in both solvents has a VBE of about 2.5 eV.

Because of the number of optimizable dimensions inherent to GLA, the calculated error bounds on the kinetic components are quite broad. We turn to a data analysis method with fewer optimizable parameters, integration of intensity in selected energy windows, in order to directly compare the dynamics in specific spectral regions and thus to assess the effect of isotopic substitution on the kinetics in the regions of interest. We improve upon the integrated intensity windows in our last presentation of the water data by using the associated spectra from GLA to motivate regions in which to fit the integrated intensity. These integrations are shown in Fig. 6.2B. The spectrally pure region of feature III, shown in green, lies below 1.2 eV. Feature I, the blue curve, does not overlap with feature II at kinetic energies greater than 3.0 eV. Feature II, the red curve, overlaps with both I and III, so the most reasonable place to integrate is the region of maximum intensity between 2.0 and 2.3 eV eKE.

Typical fit results from the integrated intensity in the energy regions of interest are shown in Fig. 6.2. Fit results from Fig 6.2A yield lifetimes of 96 ± 9 fs for the blue curve, 380 ±

40 fs for the red curve, and 410 ± 60 fs for the green curve. The error bounds are somewhat larger on the green curve due to non-linear noise scaling at low kinetic energy. Though the noise is equivalent for all time of flight bins, the magnitude of the noise becomes larger at low kinetic energy when scaled by the Jacobian transformation. As observed in fig. 6.1B, the lifetimes for the rise of the green curve and the decay of the red are the same to within error. Further, integration in these energy lanes reproduces the lifetimes extracted from the GLA.

As shown in Fig. 6.2B, the lifetime of region I in D_2O is longer than the lifetime in H_2O. A fit to the integrated intensity in this region yields a lifetime of 69 ± 11 fs for H_2O and 96 ± 9 fs for D_2O. The lifetime of the water data has a slightly larger error bound due to the fact that, as in our previous work, the lifetime of region I in water is very near the limits of the time resolution of the experiment, even in spite of improvements to the resolution. Using the lifetimes from lane integration, the isotope effect for this transition, $\tau_{IC}(\mathrm{D2O})/\tau_{IC}(\mathrm{H2O})$, is found to be 1.3 ± 0.2.

In summary, from GLA we find that there are two kinetic components in each solvent whose associated spectra are well explained by a three-step sequential kinetic mechanism. Also, the shape of the associated spectra for features I, II and III are similar in both solvents, and both solvents exhibit one lifetime shorter than 100 fs and one lifetime of ∼380 fs. Using GLA to motivate energy regions in which to fit the intensity, we are able to report substantially narrower error bounds without imposing a bias on the selection of energy lanes. Finally, we conclude that the <100 fs lifetime exhibits an isotope effect of 1.3 ± 0.2.

6.5 Discussion

As detailed in the introduction, the relaxation mechanism of the solvated electron after electronic excitation is expected to comprise three steps: relaxation on the excited state, internal conversion to the ground state, and solvent relaxation on the ground state. Prior work in water using transient absorption identified three lifetimes, <100 fs, ∼400 fs, and ∼1.1 ps, and the assignment of the mechanism was narrowed to one of two possibilities [11, 13, 15]. In the adiabatic mechanism, the fastest lifetime is assigned to τ_p, τ_{IC} is ∼400 fs, and τ_s is 1.1 ps. In the non-adiabatic mechanism, the <100 fs lifetime is assigned to τ_{IC} and the ground state relaxes by a two-step mechanism[17].

$$\begin{aligned} \text{Experiment:} \quad & \mathrm{I} \xrightarrow{\text{100fs}} \mathrm{II} \xrightarrow{\text{380fs}} \mathrm{III} \\ \text{Adiabatic:} \quad & \left|\mathrm{p}^*\right\rangle \xrightarrow{\tau_{\mathrm{p}^*}\text{100fs}} \left|\mathrm{p}\right\rangle \xrightarrow{\tau_{\mathrm{IC}}=\text{380fs}} \left|\mathrm{s}^*\right\rangle \xrightarrow{?} \left|s\right\rangle \\ \text{Non-Adiabatic:} \quad & \left|\mathrm{p}\right\rangle \xrightarrow{\tau_{\mathrm{IC}}\text{100fs}} \left|\mathrm{s}^*\right\rangle \xrightarrow{\tau_{\mathrm{s}^*}=\text{380fs}} \left|\mathrm{s}\right\rangle \end{aligned} \tag{6.4}$$

As in our previous work [28, 29], much of the argument presented here hinges on the identification of τ_{IC}. If τ_{IC} is <100 fs then the relaxation mechanism is non-adiabatic, but if τ_{IC} is ~400 fs, the mechanism is adiabatic. In prior work in water and methanol, the mechanism was assigned in favor of the non-adiabatic mechanism. Here, new results including the isotope effect for the various relaxation times and improved data fitting routines provide considerable insight regarding the assignment of the mechanism.

Similar arguments in favor of the non-adiabatic mechanism are appropriate here. First, by examining Fig. 6.4, the energy interval which spans feature II has clear overlap with the weakly bound edge of the ground state as would be expected from the unrelaxed ground state. Feature II then exchanges directly with the ground state on a 400 fs timescale as shown in both the GLA and lane integrated data. The energy interval for feature I, shown in Fig. 6.4, is well separated from the ground state. Further, a shift of 0.5 eV, which separates feature I from feature II, is rather large for a shift on the excited state potential.

Next, as seen in Fig 6.1A and B, there appears to be shift in the range of 2.0 to 2.3 eV in the raw TRPES data. Spectral shifts are typical for solvation processes as one would expect for solvent reorganization after internal conversion. Also, we observe no picosecond relaxation time within our 10 ps observation window. If the ~400 fs lifetime were τ_{IC}, some solvent relaxation lifetime for the ground state would be expected; therefore, it is unlikely the τ_{IC} is ~400 fs.

The presence of a strong isotope effect provides further evidence for the non-adiabatic mechanism. The lifetimes presented here imply an isotope effect $\tau_{IC}(\mathrm{D2O})/\tau_{IC}(\mathrm{H2O})$ of 1.3 ± 0.2. This bears close similarity to the factor of $\sqrt{2}$ predicted from a ratio of the deuterium oxide to water vibrational frequencies. A strong isotope effect on the IC rate of up to 3.5 is predicted from theory [35, 44]. Schwartz and et. al. report that the isotope effect for τ_{IC} is due to the contribution of the solvent nuclear coordinates to the non-adiabatic coupling during internal conversion. The lack of an isotope effect for the ground state equilibration time may imply the importance of solvent translational modes on the relaxation process[35].

Therefore, we assign the 69 ± 11 fs lifetime in water 96 ± 9 fs in D_2O to internal conversion and conclude that the relaxation mechanism for both solvents is non-adiabatic. The associated spectrum for feature I in both solvents is therefore assigned to spectrum of the *p*-state and has a VBE of 2.5 eV in D_2O. The ~400 fs lifetime in both solvents is then assigned to solvent relaxation on the ground state.

Our results are in good agreement with the fastest lifetimes measured in TA in water 30-80 fs[11, 15] and in D_2O 70-120 fs. Also, τ_2 is in good agreement with the 200-400 fs lifetime reported from TA in both water and D_2O. Further, the isotope effect measured from TA experiments range from 1.2-1.6[11, 15, 16], also in agreement with results presented here. The 380 fs ground state lifetime exhibits no isotope effect as was also observed in TA experiments.

Extrapolation of the τ_{IC} for water and deuterated water clusters of size 70 to 200 molecules yields an internal conversion lifetime for water of 63 ± 6 and for D_2O 160 ± 18 fs, an isotope effect of 2.8[25]. The choice to include only the larger solvent clusters into the fit was motivated by a discontinuity in the detachment energy as a function of cluster size at n=70. This discontinuity was explained by the disappearance at large cluster size of "double acceptor" water molecules, in which a single water molecule binds a diffuse electron on the water surface[45]; therefore, the larger clusters sizes should be more representative of the internally solvated state of the bulk. Including sizes 13 to 100 for water and sizes 25 to 50 in D_2O yields lifetimes of 54 ± 30 and 72 ± 22 for water and D_2O respectively, an isotope effect of 1.2[23].

Interestingly, the lifetime for D_2O, 96 ± 8 fs, and the isotope effect measured here are in better agreement with extrapolated results which do not include large cluster sizes. In water, Young et. al. showed a variation in τ_{IC} but not the detachment energy with clustering temperature in cluster anions, with faster IC times in warmer source conditions[46]. Even though the extrapolated binding energy for D_2O clusters is the same as that in H_2O and is in agreement with results in the bulk, colder cluster temperatures could slow the observed IC time relative to the bulk. The internal conversion lifetime for water reported here of 69 ± 11 fs is in agreement with either extrapolation method.

6.6 Conclusion

Time-resolved photoelectron spectroscopy measurements have been performed on solvated electrons in water and deuterium oxide solutions. After excitation of the s→p absorption band, the relaxation dynamics of the excited electron are monitored as a function of pump-probe delay. In both solvents, the electron is found to relax via the non-adiabatic mechanism, in agreement with our prior work in water, methanol, and extrapolation from solvent cluster anions. The isotope effect of the internal conversion lifetime upon deuteration of the solvent is found to be 1.3 ± 0.1. No change in the ground state solvation lifetime in D_2O is found by comparison to H_2O.

Acknowledgements

This work was funded by the National Science Foundation under the grant CHE-1361412 and by the Air Force Office of Scientific Research under grant number 24086151-06. The data presented here are available on request sent to dneumark@berkeley.edu.

References and Notes

6.7 References

[1] E. J. Hart and J. W. Boag, J. Am. Chem. Soc. **84**, 4090 (1962).

[2] B. Boudaïffa, P. Cloutier, D. Hunting, M. A. Huels, and L. Sanche, Science **287**, 1658 (2000).

[3] B. C. Garrett, D. A. Dixon, D. M. Camaioni, D. M. Chipman, M. A. Johnson, C. D. Jonah, G. A. Kimmel, J. H. Miller, T. N. Rescigno, P. J. Rossky, S. S. Xantheas, S. D. Colson, A. H. Laufer, D. Ray, P. F. Barbara, D. M. Bartels, K. H. Becker, K. H. Bowen, S. E. Bradforth, I. Carmichael, J. V. Coe, L. R. Corrales, J. P. Cowin, M. Dupuis, K. B. Eisenthal, J. A. Franz, M. S. Gutowski, K. D. Jordan, B. D. Kay, J. A. LaVerne, S. V. Lymar, T. E. Madey, C. W. McCurdy, D. Meisel, S. Mukamel, A. R. Nilsson, T. M. Orlando, N. G. Petrik, S. M. Pimblott, J. R. Rustad, G. K. Schenter, S. J. Singer, A. Tokmakoff, L.-S. Wang, and T. S. Zwier, Chem. Rev. **105**, 355 (2005).

[4] J. Gu, J. Leszczynski, and H. F. Schaefer, Chem. Rev. **112**, 5603 (2012).

[5] P. E. Mason, F. Uhlig, V. Vaněk, T. Buttersack, S. Bauerecker, and P. Jungwirth, Nat Chem **7**, 250 (2015).

[6] J. A. Kloepfer, V. H. Vilchiz, V. A. Lenchenkov, and S. E. Bradforth, Chem. Phys. Lett. **298**, 120 (1998).

[7] J. A. Kloepfer, V. H. Vilchiz, V. A. Lenchenkov, A. C. Germaine, and S. E. Bradforth, J. Chem. Phys. **113**, 6288 (2000).

[8] J. A. Kloepfer, V. H. Vilchiz, V. A. Lenchenkov, X. Y. Chen, and S. E. Bradforth, J. Chem. Phys. **117**, 766 (2002).

[9] X. Y. Chen and S. E. Bradforth, Annu. Rev. Phys. Chem. **59**, 203 (2008).

[10] C. Silva, P. K. Walhout, P. J. Reid, and P. F. Barbara, J. Phys. Chem. A **102**, 5701 (1998).

[11] K. Yokoyama, C. Silva, D. H. Son, P. K. Walhout, and P. F. Barbara, J. Phys. Chem. A **102**, 6957 (1998).

[12] A. Baltuška, M. F. Emde, M. S. Pshenichnikov, and D. A. Wiersma, J. Phys. Chem. A **103**, 10065 (1999).

[13] M. Assel, R. Laenen, and A. Laubereau, Chem. Phys. Lett. **317**, 13 (2000).

[14] M. J. Tauber and R. A. Mathies, J. Phys. Chem. A **105**, 10952 (2001).

[15] M. S. Pshenichnikov, A. Baltuska, and D. A. Wiersma, Chem. Phys. Lett. **389**, 171 (2004).

[16] A. Thaller, R. Laenen, and A. Laubereau, Chem. Phys. Lett. **398**, 459 (2004).

[17] L. Turi and P. J. Rossky, Chem. Rev. **112**, 5641 (2012).

[18] D. M. Neumark, Mol. Phys. **106**, 2183 (2008).

[19] R. M. Young and D. M. Neumark, Chem. Rev. **112**, 5553 (2012).

[20] J. M. Weber, J. Kim, E. A. Woronowicz, G. H. Weddle, I. Becker, O. Cheshnovsky, and M. A. Johnson, Chem. Phys. Lett. **339**, 337 (2001).

[21] A. E. Bragg, J. R. R. Verlet, A. Kammrath, O. Cheshnovsky, and D. M. Neumark, Science **306**, 669 (2004).

[22] D. H. Paik, I.-R. Lee, D.-S. Yang, J. S. Baskin, and A. H. Zewail, Science **306**, 672 (2004).

[23] A. E. Bragg, J. R. R. Verlet, A. Kammrath, O. Cheshnovsky, and D. M. Neumark, J. Am. Chem. Soc. **127**, 15283 (2005).

[24] O. T. Ehrler, G. B. Griffin, R. M. Young, and D. M. Neumark, J. Phys. Chem. B **113**, 4031 (2009).

[25] G. B. Griffin, R. M. Young, O. T. Ehrler, and D. M. Neumark, J. Chem. Phys. **131**, 194302 (2009).

[26] J. V. Coe, G. H. Lee, J. G. Eaton, S. T. Arnold, H. W. Sarkas, K. H. Bowen, C. Ludewigt, H. Haberland, and D. R. Worsnop, J. Chem. Phys. **92**, 3980 (1990).

[27] L. Ma, K. Majer, F. Chirot, and B. von Issendorff, J. Chem. Phys. **131**, 144303 (2009).

[28] M. H. Elkins, H. L. Williams, A. T. Shreve, and D. M. Neumark, Science **342**, 1496 (2013).

[29] M. H. Elkins, H. L. Williams, and D. M. Neumark, J. Chem. Phys. **142**, 234501 (2015).

[30] A. Lübcke, F. Buchner, N. Heine, I. V. Hertel, and T. Schultz, Phys. Chem. Chem. Phys. **12**, 14629 (2010).

[31] A. T. Shreve, T. A. Yen, and D. M. Neumark, Chem. Phys. Lett. **493**, 216 (2010).

[32] Y. Tang, Y.-i. Suzuki, H. Shen, K. Sekiguchi, N. Kurahashi, K. Nishizawa, P. Zuo, and T. Suzuki, Chem. Phys. Lett. **494**, 111 (2010).

[33] K. R. Siefermann, Y. X. Liu, E. Lugovoy, O. Link, M. Faubel, U. Buck, B. Winter, and B. Abel, Nature Chemistry **2**, 274 (2010).

[34] T. Horio, H. Shen, S. Adachi, and T. Suzuki, Chem. Phys. Lett. **535**, 12 (2012).

[35] B. J. Schwartz and P. J. Rossky, J. Chem. Phys. **105**, 6997 (1996).

[36] F. Buchner, A. Lübcke, N. Heine, and T. Schultz, Rev. Sci. Instrum. **81**, 113107 (2010).

[37] S. Thürmer, R. Seidel, M. Faubel, W. Eberhardt, J. C. Hemminger, S. E. Bradforth, and B. Winter, Phys. Rev. Lett. **111**, 173005 (2013).

[38] Y.-i. Yamamoto, Y.-I. Suzuki, G. Tomasello, T. Horio, S. Karashima, R. Mitríc, and T. Suzuki, Phys. Rev. Lett. **112**, 187603 (2014).

[39] P. Kruit and F. H. Read, Journal of Physics E: Scientific Instruments **16**, 313 (1983).

[40] A. T. Shreve, M. H. Elkins, and D. M. Neumark, Chemical Science **4**, 1633 (2013).

[41] J. R. Knutson, D. G. Walbridge, and L. Brand, Biochemistry (Mosc.) **21**, 4671 (1982).

[42] I. H. M. van Stokkum, D. S. Larsen, and R. van Grondelle, Biochim. Biophys. Acta **1657**, 82 (2004).

[43] H. Marciniak and S. Lochbrunner, Chem. Phys. Lett. **184**, 609 (2014).

[44] E. Neria and A. Nitzan, J. Chem. Phys. **99**, 1109 (1993).

[45] N. I. Hammer, J.-W. Shin, J. M. Headrick, E. G. Diken, J. R. Roscioli, G. H. Weddle, and M. A. Johnson, Science **306**, 675 (2004).

[46] R. M. Young, M. A. Yandell, S. B. King, and D. M. Neumark, J. Chem. Phys. **136**, 094304 (2012).

Part III

Attosecond Dynamics in Liquid Jets

Chapter 7

Attosecond Auger Electron Spectroscopy in Bulk Liquid

While the timescale of a molecular vibration is on the order of hundreds of femtoseconds, the motion of electrons ranges from hundreds of femtoseconds into the attosecond regime. As the experimentally achievable duration of ultrafast pulses decreases, the study of electron motion in real time becomes possible. With this resolution, fundamental phenomena such as quantum beating, valence level electronic relaxation, and the real-time dynamics of Auger processes can be observed.

While experiments with attosecond resolution in the gas phase are increasingly common, condensed phase systems have become the new frontier of the attosecond community. Attosecond phenomena in the condensed phase include many and varied processes. In the solid phase, the band gap evolution in silicon following valence to conduction band excitation occurs on a timescale faster than 500 as[1]. In the liquid phase, a class of Auger decay processes called intermolecular coloumbic decay (ICD) appear [2]. These are unique to soft matter systems and clusters, which is where efforts here will be focused. In this section, a discussion of principles, designs, and first experiments for a liquid jet photoelectron spectrometer with attosecond resolution is proposed.

7.1 Attosecond Pulse Generation and Pump-Probe

The techniques by which an attosecond pulse is generated and isolated are discussed at length in the doctoral theses of Annelise Beck[3], Justine Bell[4], and Mark Abel [5]; however, for the purposes of readability, a short discussion of this is included here. First, high harmonic generation (HHG) is used to generate extreme ultraviolet pulses with durations of less than one femtosecond[6]. Next, attosecond pulses can be isolated with one of a several techniques including: double optical gating[7], polarization gating [8], intensity gating[9], etc. Finally, characterization of the pulse is done using a streaking measurement.

As a consequence of the uncertainty principle, generating pulses with very short time durations requires a large energy bandwidth. High harmonic generation is the technique by which the frequency of a driving field can be unconverted to higher energy, integer multiples of the fundamental frequency. In this case, a few cycle 800 nm pulse is focused into a rare gas target yielding only odd order harmonics. The process by which harmonics are made can be understood using Corkum's Three Step Model [6]. First, near a maximum in the driving laser field electrons can be tunnel ionized from the rare gas atom. After the electron escapes the atom, it moves in the driving field of the laser, which reverses direction and slams the electron back into the parent atom. This results in a burst of attosecond XUV photons at every half cycle of the field.

Because the driving field has a few complete optical cycles, several bursts of attosecond light are generated, resulting in an attosecond pulse train. In order to perform a pump-probe experiment, it is ideal to have only a single attosecond pulse. There are a number of ways to accomplish this, but the typical method used in the Leone and Neumark groups is double optical gating (DOG)[7]. This method exploits the fact that linearly polarized light has a much greater HHG efficiency than circular or elliptically polarized light[8]. A set of quartz plates are used to create two counter rotating circularly polarized pulses. This method, also called polarization gating, has the effect of creating a pulse with linear polarization in a very narrow window. In DOG, polarization gating is used with addition of the second harmonic, used to shape the IR driving field. This breaks the symmetry of the electric field such that there is only enough intensity for HHG every half cycle. This lengthens the gate width by a factor of two and allows for HHG at both even and odd harmonics.

Once an attosecond pulse has been generated, it is necessary to characterize the bandwidth, chirp, and temporal duration of the pulse. Characterization of the spectrum of the pulse is relatively easily accomplished with an XUV grating and camera. The temporal profile of the pulse is characterized by an attosecond streaking measurement. Annelise Beck's thesis has an excellent chapter on the reconstruction of attosecond pulses by streaking[3].

Briefly, streaking takes advantage of the ability of the strong electric field of an intense IR pulse to shift the momentum of an electron. First, the attosecond pulse ionizes a gas target, generating photoelectrons. These photoelectrons then experience the field of an IR pulse at a variable time delay and are accelerated or decelerated toward the detector, depending on the sign of field. The photoionization of the gas target is assumed to be instantaneous; therefore, the distribution of photoelectrons is a copy of the attosecond pulse. Chirp in the attosecond pulse appears as an asymmetry in the streak trace. A pre- or post- pulse manifests as modulation in the kinetic energy spread.

Typically, ultrafast pulse characterization is done by splitting the pulse in half to create

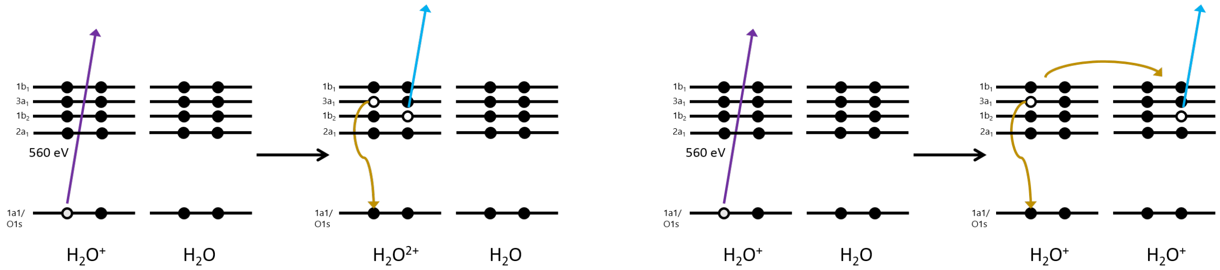

Figure 7.1: Schematic: Auger Emission (left) and Intermolecular Coulombic Decay (right).

an interferometer a process called auto-correlation, for identical pulses, or cross-correlation, if one arm of the interferometer has been modified in some way. Due to the relatively low power of the attosecond beam and the lack of good UV beam splitters, splitting the pulse in half is typically not feasible. This is also true of attosecond pump probe experiments.

Due to the difficulty of attosecond pump - attosecond probe experiments, the majority of attosecond time resolved experiments have been done with one femtosecond pulse and one attosecond pulse. Achieving resolution below the duration of one cycle of the femtoseond pulse is done by exploiting in some fashion the variation in the electric field of the femtosecond pulse with time. A streaking measurement is one way of accomplishing this. If, rather than using a target without observable dynamics, a streaking measurement were done on a system with few-femtosecond dynamics, the decay of the photoelectron population generated by the attosecond pulse would appear as interference pattern in the streaking spectrogram. Such a method has been experimentally realized in gas phase systems [10].

7.2 Auger Emission and Intermolecular Coulombic Decay

When a core level electron is ejected from an atom or molecule, it leaves behind a vacancy. A higher level electron may fill that vacancy; however, in order to conserve energy, energy must be released. This is most often done in the form of an emitted photon, but in some cases, a second electron can be released, leaving a second, more weakly bound vacancy. The emitted electron is called an Auger electron. Auger decay is a relatively common occurrence, especially for low atomic number elements from the inner-most core levels.

Shown in Fig 7.1 is a schematic diagram of an Auger emission process. Auger transitions are generally named by the convention, $core - B - C$, “core” is the state of the ionized core electron and B and C are valence states from which an electron falls to fill the vacancy and from which an electron is emitted, respectively. The core levels of the atoms are named using X-ray notation. The 1s orbital becomes K_1, 2s becomes L_1, $2p_{1/2}$ becomes L_2, $2p_{3/2}$ becomes L_3, 3s becomes M_1, etc. The process shown in Fig. 7.1 reflects an ionization from oxygen 1s, which is filled by the valence water $2a_1$ level and causes an emission from $1b_2$. This Auger line would therefore be called $K3a_11b_2$.

The kinetic energy of the emitted electron is approximated by the equation $E_{kin} = Ecore - E_b - E_c$. Where E_{core} is the binding energy of the core level, and E_b and E_c are the outer valence levels. The kinetic energy of the emitted electron for the process in Fig. 7.1 is then approximately $532 - 24 - 7 = 501$ eV. Notice the original photon energy does not appear here as it does in the energy balance for primary ionization processes. Since the kinetic energy is independent of photon energy, Auger and other secondary electron emissions appear as constant kinetic energy features, rather than constant binding energy features. The intensity of the Auger line competes with X-ray fluorescence. Auger emission is more likely for lower atomic number atoms and more likely for the K shell than the L.

The energy balance above is a rather crude approximation. A more accurate energy balance might include relaxation effects within the atom, the hole-hole interaction energy, and, especially in the condensed phase, an energetic shift due to the chemical environment of the medium. Because of this sensitivity to the chemical environment, Auger electron spectroscopy is particularly useful as an atom-specific probe of surface chemistry.

In the condensed phase, the neighboring atoms or molecules may participate in filling the core hole, and several new phenomena become possible. If the relaxing electron comes from another molecule or atom, the processes is referred to as electron transfer mediated decay (EMTD). More specifically, if the relaxing electron leaves from the same molecule or atom but the emitted electron leaves from a neighboring molecule or atom, the process is then called intermolecular(atomic) coulombic decay (ICD), shown schematically in Fig. 7.1. The first successful ICD experiments were performed in 2003 and 2004, and in certain systems, ICD has been shown to be the dominant relaxation channel over other Auger processes.

The chemical equation of an ICD process involving molecular valence orbitals is shown below. The ICD process is identifiable in several ways: monitoring the emitted ICD electron, the newly generated cation, or lifetime broadening of the ionized level.

$$2H_2O + h\nu \rightarrow H_2O + H_2O^+(1s^{-1}) + e^- \rightarrow H_2O^+(1b_1^{-1}) + H_2O^+(1b_1^{-1}) + e^-_{ICD} \tag{7.1}$$

The natural linewidth for very short lived states is given by the uncertainty principle, $\Delta\Gamma\Delta\tau \geq \frac{\hbar}{2}$. For example, if the Lorentzian width Γ of the line is 0.21 eV, the lifetime of the core-hole in a minimum uncertainty case is 3.1 fs. Lifetimes extracted from fits to the width of the ionized species are fundamentally an indirect measure of the lifetime and are an upper bound on the ICD lifetime. This method, the so-called “core-hole clock” method, has been used to predict ICD lifetimes on few femtosecond timescales depending upon the system. The ICD rate depends on several factors including: the matrix element connecting the ionized and valence state, distance between the two molecules, and number of nearest neighbors. For this reason, we can expect that the rate of ICD to increase with the strength of the solvation interaction and, thus, use core-hole lifetimes as a probe of the solvent network.

7.3 Proposed Experiments

While ICD has been identified in a number systems, the field is still young and open questions remain. Of principal interest to our group is a measurement of the timescales in various systems in which ICD occurs. These lifetimes are fundamentally difficult to get at for a number of reasons. Principally, laser sources with sufficient time resolution are a still a rarity. Next, relatively high energy photons are necessary, depending on the binding energy of the ionized state, for example: the oxygen K edge requires over 550 eV. Finally, even with a stable attosecond source of sufficient energy, successful coupling of the attosecond source to a liquid jet has yet to be demonstrated. In the following sections, three experiments are proposed, two for use with the existing attosecond source at UC Berkeley and one for use with a new high energy attosecond source at the University of Central Florida.

7.3.1 Intermolecular Coulombic Decay in Neat Water at >100 eV

With an attosecond source available at UC Berkeley, high harmonics can be readily generated with energies greater than 100 eV. Using this source, the first liquid jet experiments at Berkeley will observe ICD dynamics in neat water. The expected excitation scheme is as pictured below. With the XUV pulse, the water $2a_1$ state is ionized. A outer valence (ov) level electron drops down to fill the hole in $2a_1$ state, and finally, conserving energy, an electron from the valence band is emitted from a neighboring water molecule.

$$2H_2O + h\nu \rightarrow H_2O + H_2O^+(2a_1^{-1}) + e^- \rightarrow H_2O^+(ov^{-1}) + H_2O^+(ov^{-1}) + e^-_{ICD} \tag{7.2}$$

ICD has been observed previously in gas phase water clusters. [11] While these experiments did not have the time resolution to measure the dynamics of the decay process, they were able to conclusively demonstrate that ICD had occurred by measuring both the primary photodetached electron and the secondary, low energy ICD electron.

This particular experiment is a convenient first experiment for a number of reasons. First, the water $2a_1$ state is bound by 30 eV and is easily accessible using the >100eV attosecond

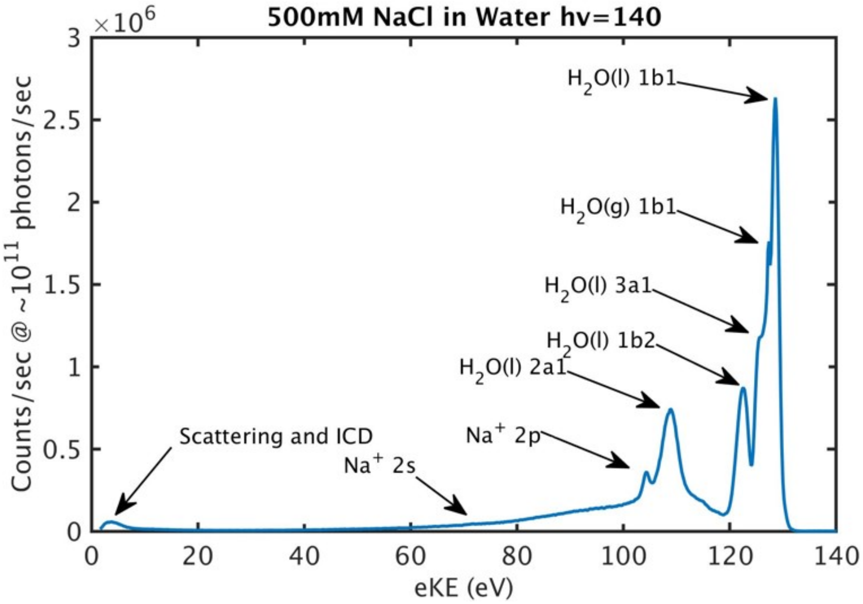

Figure 7.2: Raw X-Ray Photoelectron Spectra taken with a 140 eV beam on $50\mu m$ water jet with 500mM sodium chloride.

radiation available at UC Berkeley. Second, the experimental target density of a neat water sample is very high, especially by comparison to experiments on solutes in water. Finally, the secondary electrons, which should be generated at kinetic energies less than 10 eV, should be well-separated from the primary electrons.

As a test of the feasibility of the experiment, a series of non-time-resolved XPS experiments were performed at ALS beamline 11.0.2. XPS spectra of water at 140 eV are shown in Fig 7.2. The water has 500 mM of sodium chloride dissolved in it to mitigate any effects due to streaming potentials. The sodium ^2S and ^2P lines as well as the water valence lines are labeled in the figure. The flux from the beam line at the appropriate wavelength, exit slit width, and ring current was estimated to be $\sim 10^{11}$ photons/sec.

As shown in Fig. 7.2, the $1b_1$ line from water vapor does appear in the spectra; however, the liquid signal dominates the spectrum. The intensity of the lines shown in the figure have been used to generate a predicted count rate for the attosecond experiment assuming a typical flux of 10^7 photons per shot or 10^{10} photons per second with a magnetic bottle detector. An expected count rate for ICD events under these conditions is 25 counts/shot, which may be feasible.

7.3.2 Intermolecular Coulombic Decay in Neat Water at <550 eV

As part of the collaboration with the Institute for Frontier Attosecond Science and Technology, IFAST, the liquid jet photoelectron spectrometer will be moved to Orlando as an end station to the <550 eV, approaching 10 attosecond, source currently under construction by the Chang Group. With this photon energy, Carbon K-shell ionization and Oxygen K-edge absorption start to open up as experimental targets, which allows for a wide range of new experiments to be performed. The probability that ICD will occur increases when moving from an L-shell to a K-shell core-hole; therefore, starting with a K-shell core-hole should increase the number of ICD events and thus our ability to observe them. As a part of the collaboration with UCF, the <550 eV source will be used to measure ICD rates in water originating from oxygen $1s$ to water $4a_1$ absorption.

A schematic for the proposed experiment is shown as an equation below. This experiment is similar as to that proposed in the previous section; however, the core-hole is formed in the oxygen 1s orbital by absorption of the <550 eV beam to the water valence levels. The onset of the K-shell absorption edge is at 535 eV, and O K-shell ionization starts at $\sim$ 560 eV. K-shell ionization may or may not be accessible depending on the final characteristics of the source. Due to the exceptionally broad bandwidth predicted from the source, the x-ray pump pulse will span much of the oxygen x-ray absorption spectrum. Therefore, separating contributions from the various features may present some difficulty.

$$2H_2O + h\nu \rightarrow H_2O + H_2O^+(1s^{-1}) + e^- \rightarrow H_2O^+(vo^{-1}) + H_2O^+(vo^{-1}) + e^-_{ICD} \tag{7.3}$$

Spectra from ALS beamline 11.0.2 are shown in figure 7.3. These were taken with approximately 10^{10} photons/sec at 535 eV, the oxygen absorption pre-edge, on a sample of 500 mM sodium bicarbonate in water. The spectra clearly show peaks from ionization of the water valence levels, and several types of Auger process, all from electrons emitted from the water valence after filling a hole in the K-shell from the water valence levels. The $O_{K-1b_1,ov}$ band, especially its weakly bound edge, is the primary region of interest.

Since a significant fraction of the excited electrons will not be detached to vacuum, the Auger spectrum is further complicated by the effects of the excited electrons left in the system. If the electron initially excited from the core remains localized in a high lying valence orbital of water, the Auger electrons undergo a "spectator shift" to faster kinetic energy[12]. If the excited electron from the core delocalizes from the parent, the energy of the emitted Auger electrons is unchanged. This delocalization can occur on a less than 500 as timescale. These delocalized electrons are a precursor to the solvated electron. These dynamics may be a source of a wealth of interesting dynamics in and of itself; however, dynamics occurring on a less than one femtosecond timescale may be difficult to resolve with a streaking measurement.

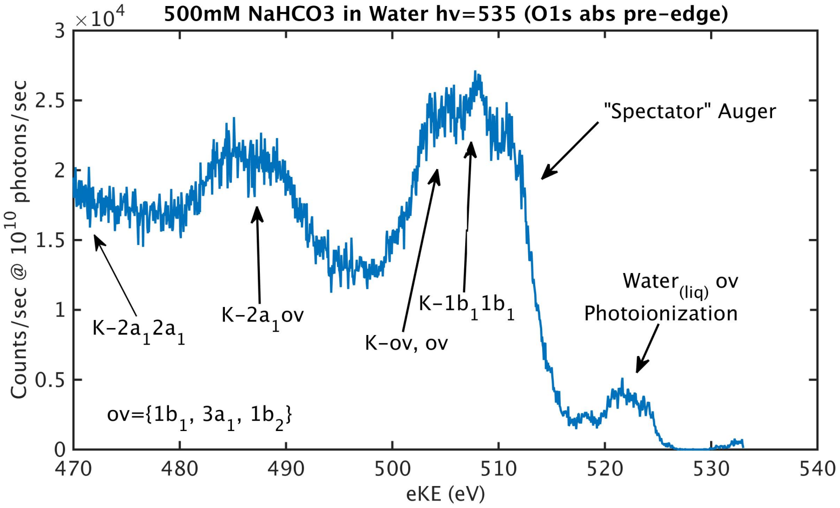

Figure 7.3: X-Ray Photoelectron Spectra taken with a 535 eV beam on 50μm water jet with 500mM sodium bicarbonate.

Recently, Thürmer et. al. were able to demonstrate the existence of fast nuclear dynamics, including ICD and proton transfer mediated (PTM) ICD, in solution[13]. Though their experiment had no time resolution, the evolution of the fast edge of the spectrum at 510 eV as a function of excitation energy and deuteration provides significant evidence for the generation of cationic water pairs in solution by either variant of ICD. They predict that the proton transfer step and subsequent energy shift in the final states occur on a 4 fs timescale, which should be resolvable with a streaking measurement.

Expected count rates here are a bit difficult to calculate as the source is unbuilt and its intensity is unknown. The ICD probability is somewhat higher when filling an K shell core-hole rather than a L-shell; however the ionization cross section is an order of magnitude lower at 500 eV than at 100 eV, so a similar count rate for Auger events is predicted in this experiment as at 100 eV for a given intensity.

7.3.3 Intermolecular Coster-Kronig Decay in Solutions at <100 eV

In addition to probing Auger processes in neat water, investigations into dissolved ions in solution may prove to be an interesting target. ICD processes which couple the ion in solution to the surrounding water molecules have been predicted to occur; however, the impact of ICD has only been inferred. Specifically, Öhrwall, et. al measured photoelectron spectra of the sodium, magnesium and aluminum 2s and 2p states[14]. In all three cases, the width of the 2s line is broader than the 2p. The 2p line is in actuality a sum of two possible spin-orbit

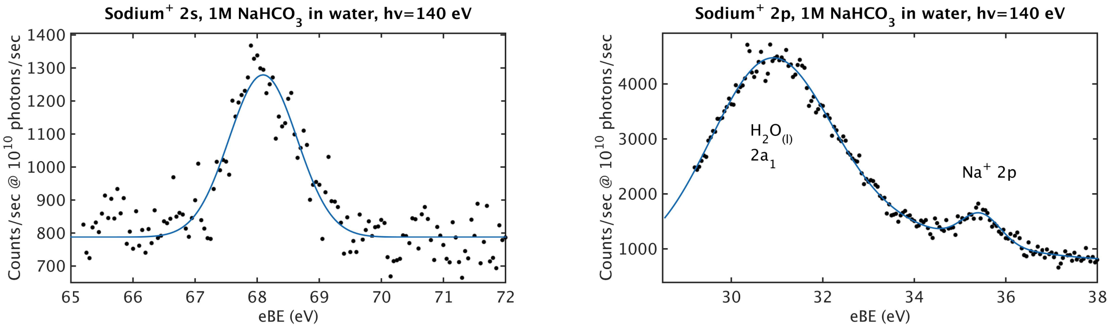

Figure 7.4: X-Ray Photoelectron Spectra of the sodium 2s (left) and 2p (right) lines taken with a 140 eV beam on $50\mu m$ water jet with 1M sodium bicarbonate.

states of the neutral. This splitting is known, and, if both features were lifetime broadened by the same amount, the 2p line would be predicted to be wider than the 2s line. The authors interpreted this as evidence for a shorter lived 2s state as compared to 2p. The authors attribute this shorter lifetime to Intermolecular Coster-Kronig Decay, a similar process to ICD in which the intermediate state core-hole is in the same shell as one of the final-state holes. The predicted process is shown schematically for sodium below.

$$H_2O + Na^+ + h\nu \rightarrow H_2O + Na^{2+}(2s^{-1}) + e^- \rightarrow H_2O^+(vo^{-1}) + Na^{2+}(2p^{-1}) + e^-_{ICD} \quad (7.4)$$

The authors show that the broadening of the 2s line, and thus the lifetime of the core-hole, tracks with the strength of the ion-solvent interaction. Specifically, lifetimes of 3.1 fs, 1.5 fs, and 0.98 fs were predicted for sodium, magnesium and aluminum ions respectively. If Intermolecular Coster-Kronig decay were occurring, it would be possible to watch the decay of the 2s core-hole and a corresponding rise of the ICD-like electrons, which should be shifted to a few eV in kinetic energy slower than the normal Auger lines.

In order to get an idea of how feasible this experiment might be, several quick experiments were done at ALS beamline 11.0.2. These experiments were done first to reproduce the data from Öhrwall et. al and second to get an idea of what kind of electron signal one might get as a function of photon flux. Due to time restrictions, only spectra of the sodium ion were taken. The target was a 1 Molar sodium bicarbonate solution which was injected at high backing pressure into vacuum through a $50\mu m$ fused silica capillary. The XPS spectra were taken with a 140 eV beam, which was the lowest energy that we were able to tune the beam. The flux from the beam line at the appropriate wavelength, exit slit width, and ring current was estimated to be $\sim 10^{11}$ photons/sec.

The XPS spectra for the sodium 2s and 2p lines are shown in Fig. 7.4. The intensity of the lines as shown in the figure have been scaled to reflect the predicted count rate of the attosecond beam at a typical flux of 10^7 photons per shot, or 10^{10} photons per second with a magnetic bottle detector. Shown on the left, the 2s line is identified by its 68.2 eV binding energy. On the right, the sodium 2p line, 35.5 eV, is shown next to the water $2a_1$ feature, 31 eV. The width of the 2s and 2p lines are found to reproduce those from Öhrwall et. al to within error. The predicted count rate for dissociation of the sodium 2s line with a lower flux beam is 1400 counts/second on a 800 counts/second baseline. This baseline is largely due to dissociation of the water $2a_1$ band, which is quite broad and extends into this region. The count rate per laser fire is the rate in counts per second divided by the repetition rate, 1000 Hz (single to few electrons per shot).

Single ionization events per shot should result in even fewer ICD events per shot. If the primary decay mechanism of the sodium core-hole were ICD, the ICD electrons would still be a relatively small peak on top of the Auger electron signal created from neat water, which is a factor of 5 larger in our overview spectrum. The reduced count rate compared to the neat water experiment is to be expected. Water is 55 molar and the sodium is one molar; therefore, the water signal should be quite large. While this experiment may be feasible, one would expect only a small change on top of a large background.

7.4 Liquid Mircrojet Photoelectron Spectrometer for an Attosecond XUV source

The apparatus designs for the new end-station are included in Appendix C. These designs are a modification of the instrument described for the femtosecond work in Chapter 2 and used to take the data in Chapters 4 to 7. The implementation of the time of flight region and the magnetic bottle are exact duplicates of Alexander Shreve's original designs[15]; however, the trap region has been entirely redesigned and has been adapted for coupling to the attosecond beamline at UC Berkeley.

A diagram of the complete end-station design, which has not been built yet, is shown in Fig. 7.5. There are four chambers shown in the design: the toroidal mirror chamber, the trap chamber, the detector chamber, and the XUV grating chamber. The toroidal mirror chamber shown is a shell with similar dimensions to the one already in existence at UC Berkeley. The existing chamber will need to be modified with a new port at the appropriate angle to allow for grazing incidence on a second toroidal mirror. A set of movable mounts will be used to switch the attosecond beam between end-stations.

The toroidal mirror chamber is connected to the end-station by a beam tube. This beam tube can be isolated by a set of valves, one manual and the other pneumatic on either end of the tube. The pneumatic valve is connected to a port on the new trap chamber and can be interlocked to protect the rest of the vacuum system in the event of a frozen jet. The manual valve on the other end of the beam tube will contain a silica plate with a metal film center, rather than a metal gate. The metal film in the center of the plate can be tuned to allow for transmission of a selected wavelength range of the XUV beam, and the silica plate transmits the IR. Since the IR streaking pulse is much larger than the XUV near the toroidal mirror, both beams can pass through the plate but gas from the trap chamber cannot. This arrangement will allow for both wavelength tuning and differential pumping of the two chambers.

The newly designed trap chamber is significantly reduced in size relative to the current femtosecond setup but maintains most of the same features plus a few new additions, including a slide valve for the detector region. The femtosecond apparatus consists of two 10 conflat 6-way crosses, while the new chamber consists of a custom designed chamber on a single 12 ID central tube. On the horizontal plane of the new trap chamber, there are two 10” CF flanges one with a door for easy access for cleaning the chamber and one which connects to the detector vacuum chamber. Also on the horizontal plane is an 8” CF port for a 450 L/sec turbo and both 2 3/4” CF flanges, which allow the laser beam to pass into the interaction region and out into the XUV grating chamber. The cryogenic pumping for this region is provided by a custom designed dewar attached on an off axis ISO 160 flange. Finally, a 1 1/3” rotary feedthrough allows for control of the slide valve. The combination of lower chamber volume and increased pumping capacity should allow for fast pump down and lower ultimate pressures.

The bottom flange allows for the attachment of the liquid trap, which is cooled by a liquid nitrogen dewar, and the Ultratorr feedthrough for the calibration gas inlet. Like in the femtosecond apparatus, the diameter of the trap is quite large so as to mitigate jet freezing by removing ice nucleation points from near the jet. Owing to the success of the larger trap on the current setup, this diameter has been increased slightly. Also, in order to simplify and speed up removal and emptying of the trap, the liquid trap has been switch from a CF flange to an ISO flange.

The top trap flange contains ports for the pressure gauge, electrical, and the jet feedthrough. An ion gauge is currently pictured in the designs; however, if the budget allows, a cold cathode gauge may be more appropriate. The electrical feedthrough is a 4-port BNC, which provides electrical for three-axis manipulation of the steering magnets for the bottle. Finally, the liquid jet design is unchanged from previous instruments and is controlled by a three-axis manual feedthrough.

The trap and detector chambers are separated by a differential pumping sheath and skimmer. The sheath has been redesigned for the new instrument to allow for the use of a slide valve between the two chambers. The valve will allow the detector chamber to remain under vacuum at all times while the trap chamber is vented and cleaned. A prior field-free instrument, which was used before the femtosecond instrument was built, also had a valve between the two chambers. The ultimate pressure in the detector region on the field-free instrument was a factor of two better than the femtosecond instrument; therefore, a similar improvement is expected for attosecond instrument. The new valve design consists of two rails, a car, the cover slip, a screw, and a skimmer. The car slides between the two rails on top of an o-ring and is held down by the cover slip on which the skimmer is mounted. The car has a thread in which a half threaded rod can be turned by a rotary feed through outside of vacuum. Since the screw is machine fixed, as the screw turns, the car moves back and forth to open and close the valve.

The detector chamber is an almost exact duplicate of the current femtosecond instrument, which has a 10" CF 6-way cross for the detector flange. The new end-station is designed around custom flange designed by Harry Gomez for the original anion PES instrument[16]. This flange is in lab, unused, and has ports for a single 1100 L/s turbo and an ion gauge as well as the necessary 10" CF flanges for the detector and sheath. The internals of this chamber are exact duplicates of the instrument described in Chapter 2.

The final chamber, the XUV grating chamber, is a first draft of a movable chamber to be used with both end-stations. A set of two gate valves, one manual and one pneumatic separate the grating chamber from the trap chamber. The pneumatic valve is used to isolate the two chambers, and the manual valve contains a thin metal filter in place of a thick steal gate. The filter allows for transmission of the XUV beam but blocks the NIR. Having filtered out the NIR, the XUV beam is then dispersed on to a grating to an XUV camera. The XUV grating chamber is based on a 8" CF 6-way cross and has it's own 450 L/sec turbo and pressure gauges.

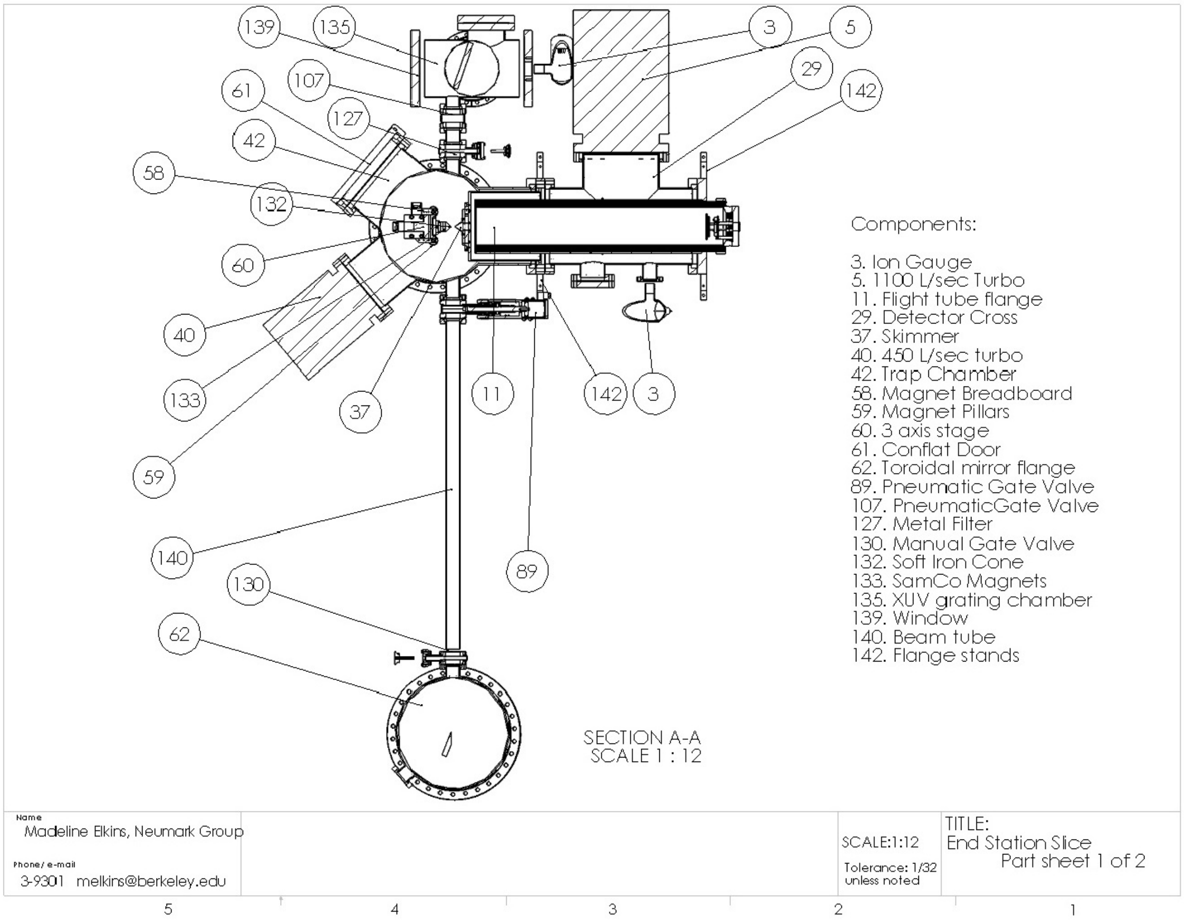

Figure 7.5: Horizontal slice through attosecond end station showing interior of the various chambers.

7.5 References

[1] M. Schultze, K. Ramasesha, C. D. Pemmaraju, S. A. Sato, D. Whitmore, A. Gandman, J. S. Prell, L. J. Borja, D. Prendergast, K. Yabana, D. M. Neumark, and S. R. Leone, Science **346**, 1348 (2014).

[2] U. Hergenhahn, Journal of Electron Spectroscopy and Related Phenomena **184**, 78 (2011).

[3] A. Beck, *Attosecond Spectroscopic Studies of Aromic and Molecular Dynamics*, Ph.D. thesis, UC Berkeley (2014).

[4] M. J. Bell, *Transient Absorption Spectroscopy With Isolated Attosecond Pulses*, Ph.D. thesis, UC Berkeley (2013).

[5] M. J. Abel, *Attosecond X-Ray Pulses For Molecular Electronic Dynamics*, Ph.D. thesis, UC Berkeley (2010).

[6] P. B. Corkum, Phys. Rev. Lett. **71**, 1994 (1993).

[7] H. Mashiko, S. Gilbertson, C. Li, S. D. Khan, M. M. Shakya, E. Moon, and Z. Chang, Phys. Rev. Lett. **100**, 103906 (2013).

[8] O. Tcherbakoff, E. Mével, D. Descamps, J. Plumridge, and E. Constant, Phys. Rev. A **68**, 043804 (2003).

[9] M. Drescher, M. Hentschel, R. Kienberger, G. Tempea, C. Spielmann, G. A. Reider, and F. Krausz, Science **291**, 1923 (2001).

[10] M. Drescher, M. Hentschel, R. Kienberger, M. Uiberacker, V. Yakovlev, A. Scrinzi, T. Westerwalbesloh, U. Kleineberg, U. Heinzman, and F. Krausz, Nature **419**, 803 (2002).

[11] M. Mucke, M. Braune, S. Barth, M. Förstel, T. Lischke, V. Ulrich, T. Arion, U. Becker, A. Bradshaw, and U. Hergenhahn, Nature Physics **6**, 143 (2010).

[12] D. Norlund, H. Ogasawara, H. Bluhm, O. Takahashi, M. Odelius, M. Nagasono, L. G. M. Pettersson, and A. Nilsson, Phys. Rev. Lett. **99**, 217406 (2007).

[13] S. Thürmer, M. Oncak, N. Ottosson, R. Seidel, U. Hergenhahn, S. E. Bradforth, P. Slavicek, and B. Winter, Nature Chemistry **5**, 590 (2013).

[14] G. Öhrwall, N. Ottosson, W. Pokapanich, S. Legendre, S. Svensson, and O. Björneholm, J. Phys. Chem. B **114**, 17057 (2010).

[15] A. T. Shreve, *Photoelectron Spectroscopy of Solvated Electrons in Liquid Microjets*, Thesis, UC Berkeley (2012).

[16] H. Gomez, *Anion Photoelectron Spectroscopy of Semiconductor Clusters and Solvated Species*, Thesis, UC Berkeley (2002).

Appendices

Appendix A

Tunable UV by Four-Wave Mixing

Sum-frequency and difference-frequency mixing in a crystal such as β-Barium Borate (BBO) are simple, cheap, and convenient methods of frequency conversion for most laser applications. Specifically, for the ultrafast community, the use of thin mixing crystals allows for high transmission and limits chirp of the incident beam and group velocity walk-off. However, the use of BBO to generate new frequencies becomes increasingly difficult as the generated frequency goes deeper into the ultraviolet. First, transmission through BBO drops precipitously after 250 nm, so what light is generated may be absorbed by the material. Second, the required mixing angle in BBO rapidly becomes non-physical (ex: doubling 400 nm to form 200 nm in BBO has a mixing angle of 90^o). Finally, the efficiency of sum- and difference-frequency mixing drops off as the mixing angle gets larger. Increasing the path length inside the crystal does increase the efficiency, but it also negatively effects the temporal profile of the pulse. Four-wave mixing (FWM) presents an alternative for generating tunable near UV pulses while preserving, or even improving, the time duration of the pulse.

Principles

The basic formula for a FWM process requires two photons of one frequency and a third photon of a lower frequency to generate a fourth color, hence four-wave.

$$\omega_4 = \omega_1 + \omega_1 - \omega_2 \tag{A.1}$$

In the implementation presented here, ω_1 is 400 nm and ω_2 is either the 800 nm fundamental of our Ti:Sapphire amplifier or infrared output from an OPA. Rather than a crystal, the mixing is carried out in a capillary filled with a rare gas, such as argon or neon.

This method of UV generation comes with a helpful side effect. The strong field of the ultrafast pulses leads to self-phase modulation within the fiber, which results in significant spectral broadening. Conversely in BBO, the intensity of the mixing process is strongly dependent on mixing angle, which is set by the frequency of the input beams. Therefore, much

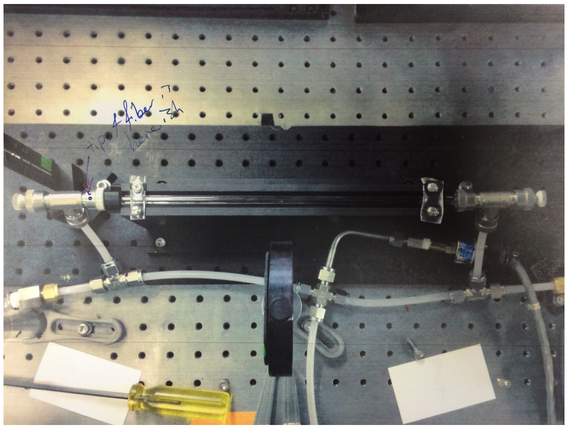

Figure A.1: Four-wave mixing apparatus after modifications to the original designs.

of the broad bandwidth of the ultrafast pulses is not converted efficiently, which leads to a systematic narrowing of the spectral width of the generated light. In a fiber, the spectrum of the generated light is broadened enough that the output beam allows for temporal compression beyond the transform limit of the *input* beam. Essentially, the four-wave mixer acts as a hollow-core fiber compressor.

Designs

The original designs for the four-wave mixing cell used, briefly, in the Neumark Group were done by R. M. Young[1] and were based on designs from Durfee, et. al.[2, 3] and Jailaubekov and Bradforth [4]. Testing and implementation of the design were incomplete as of the finish of R. M. Young's thesis; therefore, a short discussion of the modifications and implementation notes on the designs is merited here.

The heart of the FWM set-up is a $100\mu m$ ID fused silica capillary (Polymicro). This is housed inside of a larger glass tube with a $400\mu m$ ID (Schott Duran glass 6mm OD), which is just larger than the $350\mu m$ OD of the capillary. Both tubes are about 30 cm long with the capillary being slightly longer than the outer tube, such that the ends of the capillary are exposed. Two 1/4" UltraTorr tees cover the ends of the outer tube. In the far ends of the tees, two 1/2" windows (CaF_2, 3 mm thick) are epoxied onto 1/4" stainless steal tube. The off-axis ends of the tees are connected to polyethylene tube, from which the capillary assembly can be filled with gas (50-60 Torr of Argon) or purged as necessary.

The outer glass tube is supported by a specially designed cradle. This replaces the optic posts shown in Young's thesis. The UltraTorr fittings are still supported by optic posts. The cradle and all assorted tubes and gauges are clamped to a 24" x 6" breadboard. This allows the entire assembly to be moved on and off the table when not in use.

Ultimately, the four-wave mixing setup was never put into regular use because of the difficultly of aligning the fiber. The Clark laser system that this was used with was likely the origin of the stability problems.

Design Changes

The original designs called for quarter inch optic posts to support the outer glass tube. The glass bent considerably when on the optic table due to the weight of the UltraTorr fittings. While this bending would not make alignment in to the fiber impossible, it did make it somewhat more difficult to predict where the proper alignment might be. A new cradle was designed for the fiber and painted matte black. The designs for the cradle are at the end of this section.

Next, in order to reduce the weight and flexing of the beam tube, all components beyond the original UltraTorr tees have been removed, and the windows have been mounted directly into the open ends of the tees. In order to mount the windows directly in the quarter inch fittings, the windows were replaced and reglued to a smaller tube. The original designs called for a second set of brass tubes which were used to support the windows. Once the cradle was added, this additional support became unnecessary. The Ashcroft gauge pictured in Young's thesis, Fig. 2.5, was replaced with a convection and a thermocouple gauge. The Ashcroft gauge ran out of batteries quickly and would not hold a vacuum.

Daily alignment was quite difficult. Adding about 1 atm of gas to the cell made it much easier to see if the beam was hitting fiber or the glass housing. Finding temporal overlap of the 800 nm and 400 nm using SFG in a BBO was much easier than finding alignment in the cell, the temporal overlap inside the cell is slightly different but close at this point. Finally, using lens mounts with horizontal and vertical alignment adjust, not pictured, is crucial.

A.1 References

[1] R. M. Young, *Dynamics of excess electrons in atomic and molecular clusters*, Thesis, UC Berkeley (2011).

[2] C. G. Durfee III, S. Backus, M. M. Murnane, and H. C. Kapteyn, Opt. Lett. **22**, 1565 (1997).

[3] C. G. Durfee III, S. Backus, C. Herne, H. C. Kapteyn, and M. M. Murnane, Opt. Lett. **10**, 697 (1999).

[4] A. E. Jailaubekov and S. E. Bradforth, Appl. Phys. Lett. **87**, 021107 (2005).

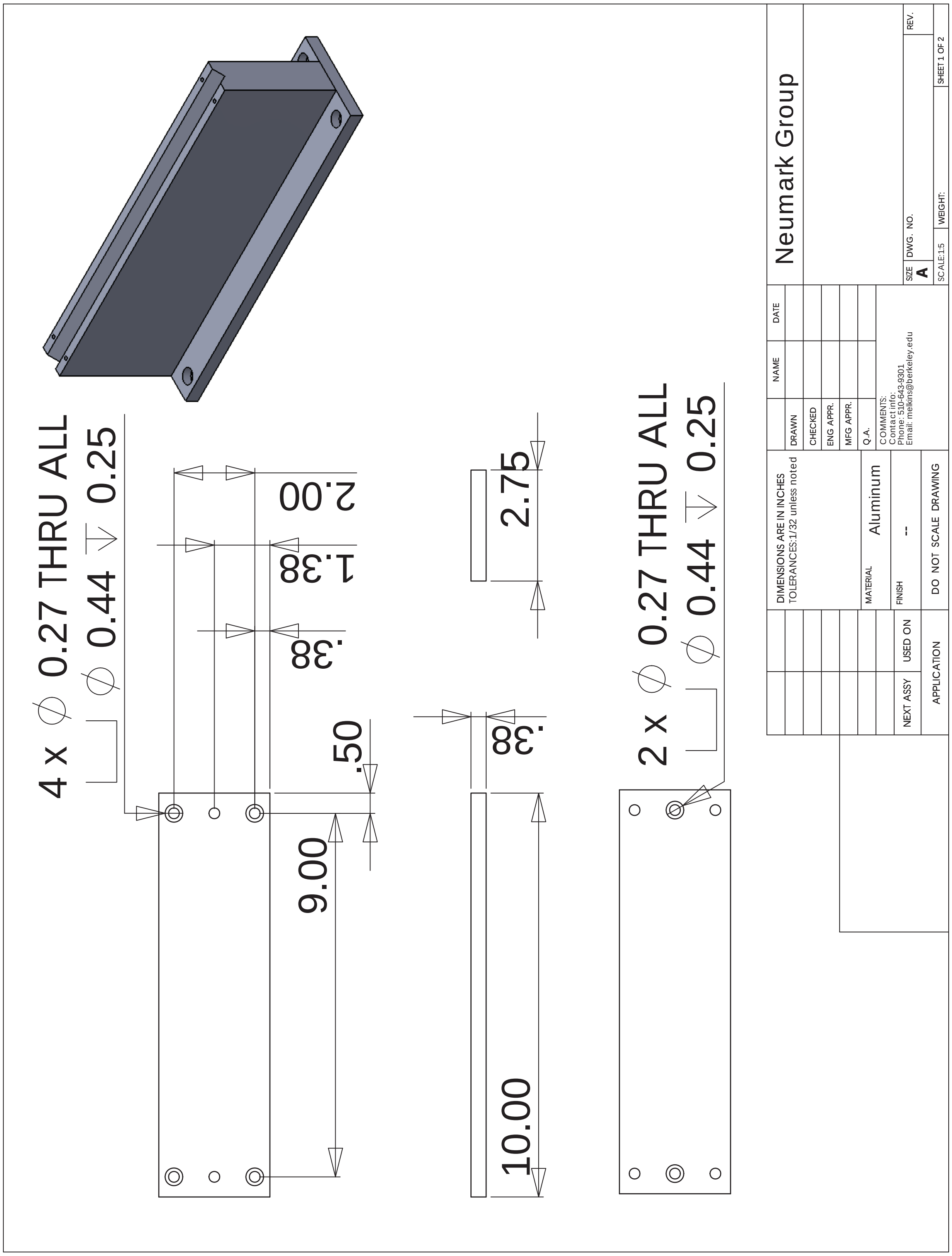

Figure A.2: Drawing for fiberstand

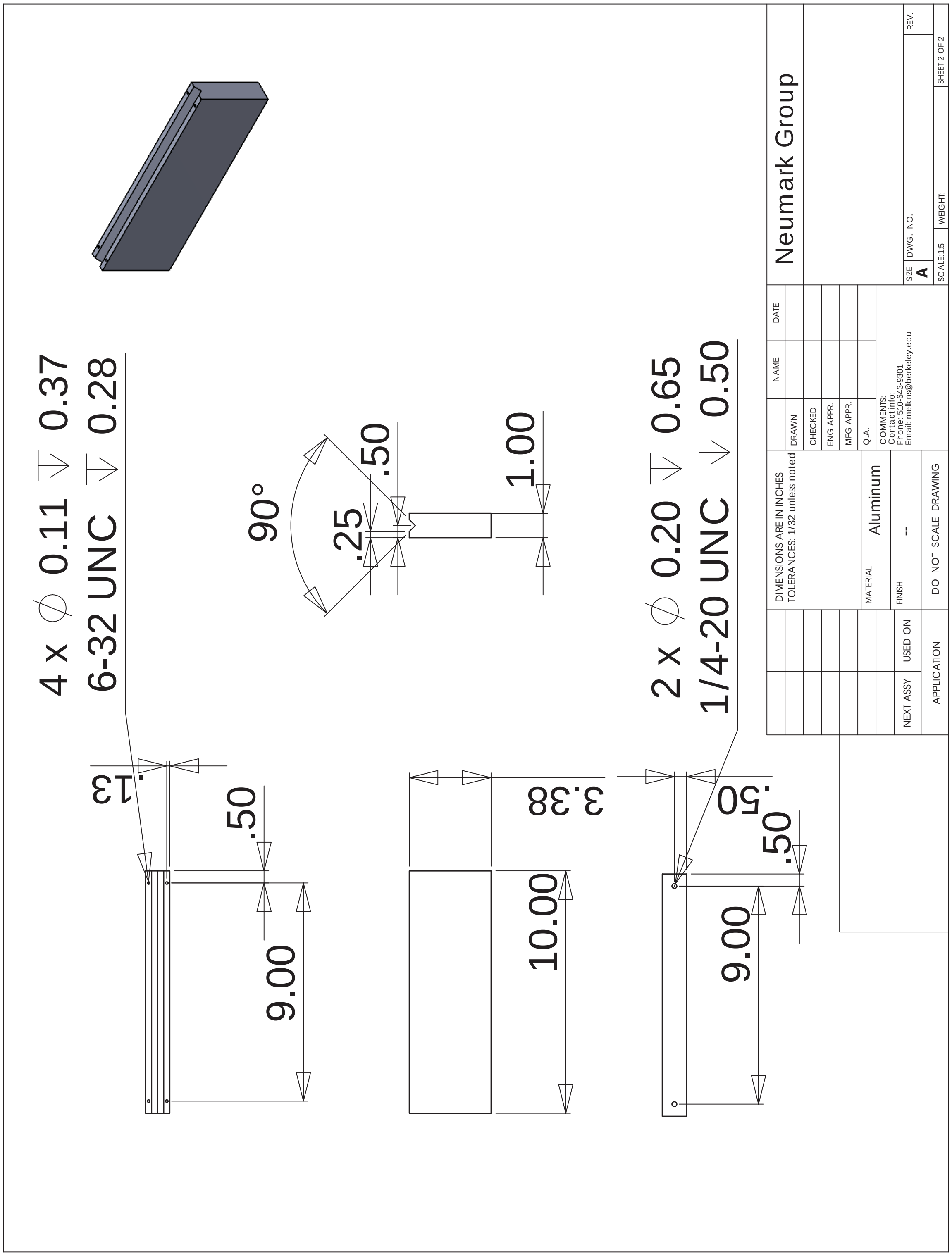

Figure A.3: Drawing for fiberstand

Appendix B

Non-Collinear Optical Parametric Amplifier

Ultrafast pulses at tunable wavelengths have been an important addition to the project. In particular, the efficiency at which solvated electrons are generated varies greatly with the cross section of the CTTS band. These band maxima vary strongly from solvent to solvent. Therefore, in order to generate a large solvated electron population, it became necessary to generate ultrafast pulses at variable UV wavelengths. There are several ways that this can be accomplished including: the second-harmonic sum-frequency signal of an IR-OPA (like the TOPAS in our lab), the second-harmonic of a non-collinear optical parametric amplifier (NOPA), four-wave mixing in a fiber, etc. Each method has its advantages and disadvantages. The SH-SFS of the TOPAS has high power and good stability but does not make wavelengths below 235 nm with any efficiency. The temporal width of the tunable UV generated from SH-SFS is also significantly broadened. The SH of a NOPA is capable of producing light below 225 nm but at low power. The four-wave mixing set-up described in the previous chapter produces even less UV power but with the shortest pulse width and bluest UV range.

Principles

The operation of a NOPA can be thought of as a variant on a difference-frequency mixing process. In difference frequency mixing, the energy of bluer of the two incident photons is equal to the sum of the redder photon and the new color being generated. This can be thought of as a stimulated emission process whereby the redder photon drives the emission of a photon with a frequency equal to the pump minus the signal; however, by energy conservation, yet another photon at the wavelength of the seed is generated.

In optical parametric amplification (OPA), the pump photon drives parametric fluorescence in the nonlinear crystal. In this process, the pump is split into a pair photons, the

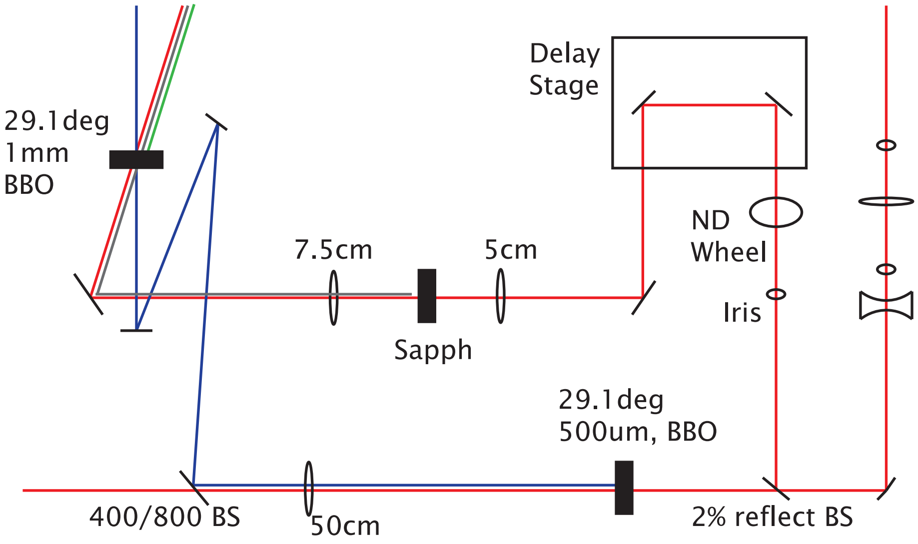

Figure B.1: Optical Layout for Non-collinear Optical Parametric Amplifier

signal and idler, subject to the energy balance below.

$$\omega_p = \omega_s + \omega_i \tag{B.1}$$

These pairs are generated at a wide range wavelengths and are emitted off of the pump beam axis, subject to conservation of momentum, in two cones of light around the central pump beam.

In a non-collinear OPA, amplification of the fluorescence being driven by the pump is accomplished by directing the seed beam along the axis of the superflourescence cone. If the seed beam is phase matched, spatially overlapped, and temporally overlapped, the seed drives the generation of light with the same wavelength as the seed (the signal) and also the difference between the seed and the pump (the idler).

In a white-light NOPA, a white-light continuum is used as the seed pulse. As long as the phase matching condition for each wavelength is met, a corresponding pair of photons will be generated. For this reason, the amplified light generated from a NOPA can exhibit a very broad bandwidth. This also allows for temporal compression of the beam past the transform limit of the pump beam.

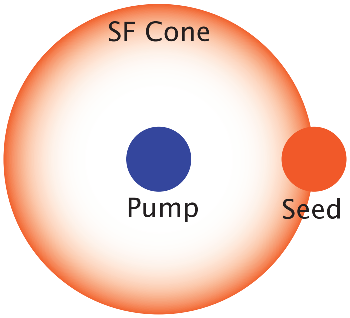

Figure B.2: Schematic showing the overlap of superfluorescence cone and seed beam after the crystal.

Design

The 800 nm fundamental from the amplifier is first telescoped down to approximately a 5 mm beam size. The maximum pump power should not exceed 400 mW at this level of focusing; otherwise, the crystals will be damaged. A longer pump pulse (120-150 fs) tends to result in higher power inside of the NOPA. From here, the optical beam path consists of two arms: one for the white light generation and one to generate the 400 nm pump beam.

2 to 5 % of the 800 nm beam is routed to the white light generation stage and the rest is doubled in a 29.1° BBO. The residual 800 nm is separated from the 400 nm with a dichroic beam splitter. It is important to remove as much of the 800 nm light as possible, so a second dichroic filter may be necessary at high input power. Because the superflorescence threshold is already near the damage threshold for the BBO, the extra 800 nm power simply damages the BBO.

The 400 nm pump beam is then focused just behind a 32° 1mm thick BBO, and in this particular design, the focal distance necessary is about 50 cm. Focusing of the 400 nm beam is best done with a spherical or off-axis parabolic mirror to conserve power and pulse duration, but the spherical lens used here is a cheaper option.

Superflorescence (SF) is generated in a cone around the pump beam. On a card, this will appear as a circle around the blue central beam. The crystal angle for optimum SF is 32°, but a 1 mm thick 29° crystal will do in a pinch. The main axis of the crystal should be 90° to the 400 nm pump beam. Both the position of the focus and the angle of the crystal need fine optimization, so the SF crystal should be mounted on a translation stage in a rotation mount.

The white light generation stage is somewhat trickier and requires quite a bit of futzing to achieve a stable alignment. The 800 nm beam should be focused tightly behind a sapphire plate, ∼5 cm focal length. The lens mount ahead of the sapphire must have horizontal and vertical fine adjustment to control the shape of the focus in the sapphire. An iris is used to make changes to the spatial mode of the 800 nm beam during alignment, and a neutral density wheel is used to change the power going into the sapphire. Less power is more stable but results in lower conversion efficiency.

The white light generated by the sapphire is much more divergent than the residual 800 nm; therefore, a lens that focuses nearly twice as tightly as would be expected to collimate the IR is necessary to collimate the white light. Nearly collimated white light rather than focused white light appeared to work better. Both lenses and the sapphire should be on an optic rail or small translation stages to fine adjust the foci.

The white light should meet the pump beam inside the crystal at as near an angle to 3° as possible. This corresponds to the seed propagating along the SF cone rather than the on the axis of the pump and is the origin of term non-collinear in the name NOPA. The two beams must be overlapped in time as well as space, so a translation stage on one of the two lines should be well aligned and adjusted until overlap is found in the crystal.

The output color ranges from teal (∼480 nm) to red (∼720 nm), depending upon the alignment, and has a maximum power at about orange (∼600 nm). The conversion efficiency of this single pass system was no more than a few percent efficient; however, multi-pass designs with efficiencies of up to 15% have been demonstrated. The output beam is slightly divergent, so a lens mount on the output will improve the collimation. Finally, the output beam is quite stretched in time and must be re-compressed using a prism compressor such as the one detailed in the thesis of R. M. Young[1].

Alignment Notes

- Begin by aligning on the entrances irises.

- Block the seed. Optimize 400 nm generation with BBO angle.

- Optimize SF generation, BBO angle, BBO rotation, focus position, and compression of pump beam from amplifier. Look for a bright stable circle of light around the 400nm beam. The circle of light from the superfluorescence should look like a rainbow with colors from red to green. The alignment is still not quite right if the color is only red to orange.

- Block the pump and unblock the seed. For first-time alignment after construction of the NOPA, pull both lenses and make sure that the beam propagates straight through the center of both post holders and level to the table.

- Add back in first lens making sure that the lens is VERY close to the sapphire. Walk the lens back looking for white light. It is important not to move the lens so far back the the focus is inside the sapphire plate. This will cause a burn.

- Optimize the white light generation using the horizontal and vertical adjust on the lens mount. Close the iris such that there is a red halo around the white light beam after the sapphire.

- Put the second lens back and center it on the white light beam.

- Align the white light beam on the SF BBO with as shallow an angle as you can manage. The closer that this angle is to 3 degrees off the pump beam the better the phase matching condition and the broader the bandwidth of the amplified beam. At this point, the second lens on the white light stage can be adjusted such that the seed beam is very weakly focused.

- Unblock the pump beam. Adjust the delay stage for temporal overlap. At this point, there should be amplified signal in some color. The power of the beam can be improved by adjusting: the steering of the seed, the focus of the seed, horizontal and vertical adjust of seed lenses, and power of the seed using the ND wheel.
- Changing the color: The color is changed primarily by adjusting the delay stage. Different colors appear at different delays. There is also a weak dependence on the steering of the seed. Finally, the BBO rotation, naturally, has a large effect of the SF spectrum. Getting the right color in good power and stability is difficult. Poor SF generation can limit the ultimate tunable range of the NOPA.

Possible Improvements:

The exact lens focal lens and the necessary ratio of pump to seed power depends greatly on input power, beam shape, and compression. Be prepared to adjust all of these as necessary. The layout of the pump line would be greatly improved from its current design with a few more high reflectors and a focusing mirror. Finally, the addition of a second amplification stage, pre-chirping the beam, or adding dispersion compensation between the two arms of the NOPA has not been attempted.

B.1 References

[1] R. M. Young, *Dynamics of excess electrons in atomic and molecular clusters*, Thesis, UC Berkeley (2011).

Appendix C

Machine Drawings: Liquid Jet Photoelectron Spectrometer for an Attosecond XUV Source

In this appendix are the machine drawings for a new liquid jet photoelectron spectrometer to be used as an endstation interchangeably with two attosecond sources at Berkeley and at the University of Central Florida. The designs are as discussed in section xxxx. The chamber consists of the liquid microjet, a magnetic bottle time of flight photoelectron spectrometer, and an XUV spectrometer for characterization of the attosecond beam. Improvements to the last instrument include the addition of a custom designed slide valve for the detector chamber, increased pumping on the the trap chamber, and a further increase in size of the trap volume and area. Finally, the chamber door and much of the designs for the magnetic bottle were kept from the original instrument.

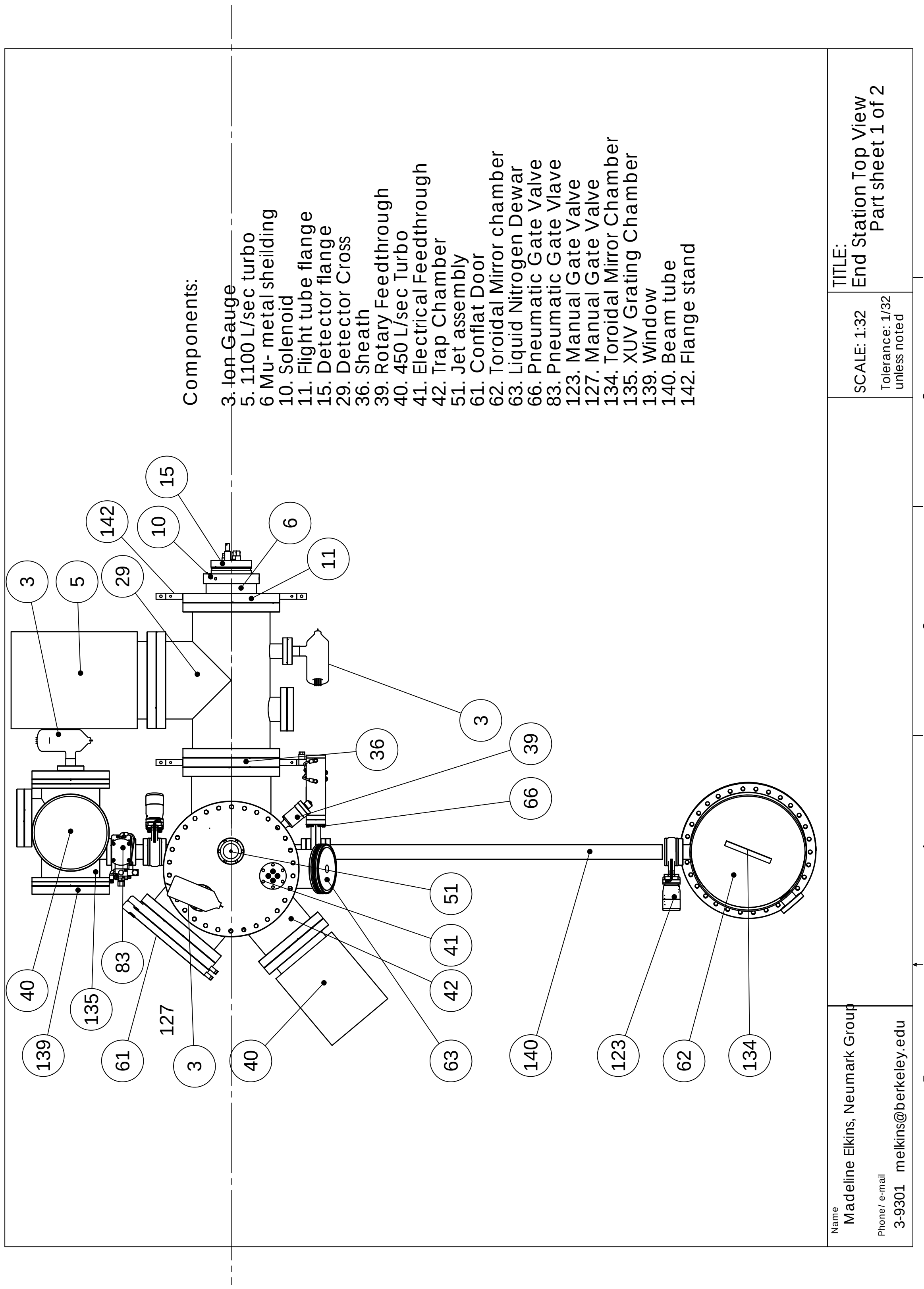
Components:
3. Ion Gauge
5. 1100 L/sec turbo
6 Mu- metal sheilding
10. Solenoid
11. Flight tube flange
15. Detector flange
29. Detector Cross
36. Sheath
39. Rotary Feedthrough
40. 450 L/sec Turbo
41. Electrical Feedthrough
42. Trap Chamber
51. Jet assembly
61. Conflat Door
62. Toroidal Mirror chamber
63. Liquid Nitrogen Dewar
66. Pneumatic Gate Valve
83. Pneumatic Gate Vlave
123. Manual Gate Valve
127. Manual Gate Valve
134. Toroidal Mirror Chamber
135. XUV Grating Chamber
139. Window
140. Beam tube
142. Flange stand
15
142
10
6
3
5
29
11
3
36
39
66
51
41
42
40
83
135
127
139
61
3
40
63
140
123
62
134
TITLE:
End Station Top View
Part sheet 1 of 2
SCALE: 1:32
Tolerance: 1/32 unless noted
Name
Madeline Elkins, Neumark Group
Phone/ e-mail
3-9301 melkins@berkeley.edu
1
2
3
4
5

Figure C.1:

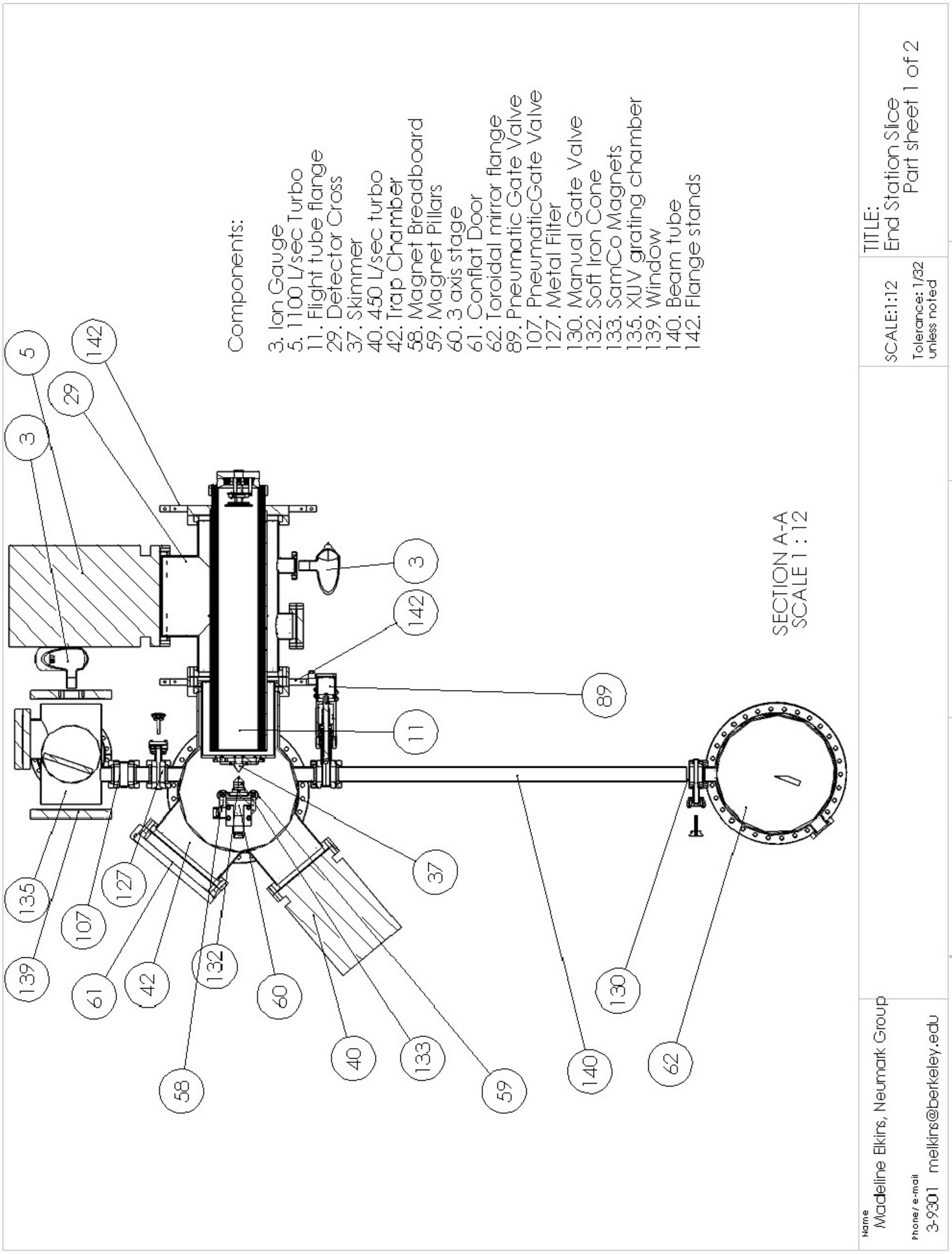
Components:
3. Ion Gauge
5. 1100 L/sec Turbo
11. Flight tube flange
29. Detector Cross
37. Skimmer
40. 450 L/sec turbo
42. Trap Chamber
58. Magnet Breadboard
59. Magnet Pillars
60. 3 axis stage
61. Conflat Door
62. Toroidal mirror flange
89. Pneumatic Gate Valve
107. PneumaticGate Valve
127. Metal Filter
130. Manual Gate Valve
132. Soft Iron Cone
133. SamCo Magnets
135. XUV grating chamber
139. Window
140. Beam tube
142. Flange stands
SECTION A-A
SCALE 1 : 12
3
5
29
142
3
142
89
11
37
135
107
127
139
61
42
132
60
40
133
59
140
130
62
58
1
2
3
4
5
TITLE:
End Station Slice
Part sheet 1 of 2
SCALE:1:12
Tolerance: 1/32
unless noted
Name
Madeline Elkins, Neumark Group
Phone/ e-mail
3-9301 melkins@berkeley.edu

Figure C.2:

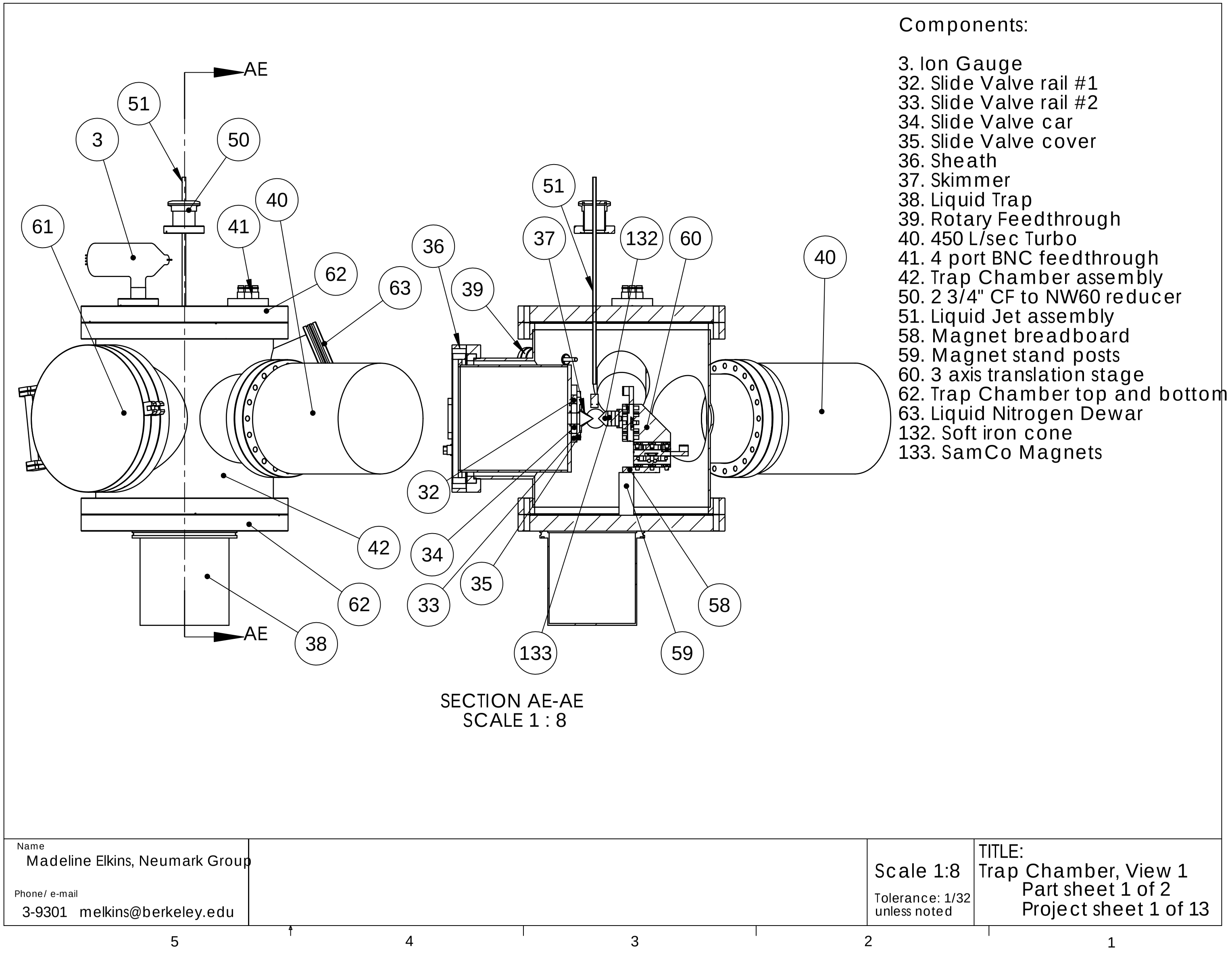
Components:
3. Ion Gauge
32. Slide Valve rail #1
33. Slide Valve rail #2
34. Slide Valve car
35. Slide Valve cover
36. Sheath
37. Skimmer
38. Liquid Trap
39. Rotary Feedthrough
40. 450 L/sec Turbo
41. 4 port BNC feedthrough
42. Trap Chamber assembly
50. 2 3/4" CF to NW60 reducer
51. Liquid Jet assembly
58. Magnet breadboard
59. Magnet stand posts
60. 3 axis translation stage
62. Trap Chamber top and bottom
63. Liquid Nitrogen Dewar
132. Soft iron cone
133. SamCo Magnets
AE
AE
51
3
50
61
40
41
62
63
42
62
38
36
39
32
34
33
35
37
51
132
60
133
59
58
40
SECTION AE-AE
SCALE 1 : 8
Name
Madeline Elkins, Neumark Group
Phone/ e-mail
3-9301 melkins@berkeley.edu
Scale 1:8
Tolerance: 1/32
unless noted
TITLE:
Trap Chamber, View 1
Part sheet 1 of 2
Project sheet 1 of 13
5
4
3
2
1

Figure C.3:

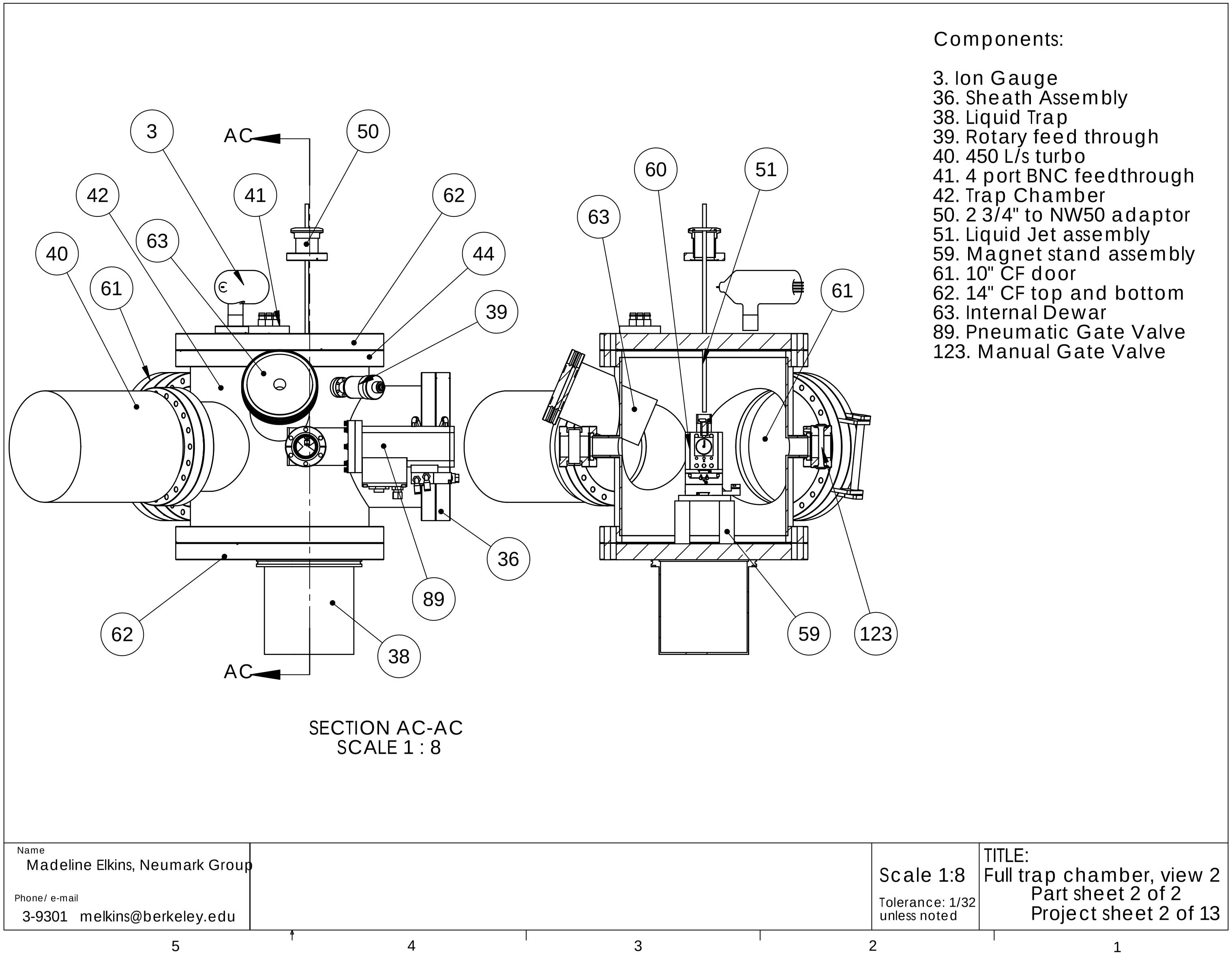
Components:
3. Ion Gauge
36. Sheath Assembly
38. Liquid Trap
39. Rotary feed through
40. 450 L/s turbo
41. 4 port BNC feedthrough
42. Trap Chamber
50. 2 3/4" to NW50 adaptor
51. Liquid Jet assembly
59. Magnet stand assembly
61. 10" CF door
62. 14" CF top and bottom
63. Internal Dewar
89. Pneumatic Gate Valve
123. Manual Gate Valve
3
AC
50
42
41
62
63
44
40
61
39
36
89
62
38
AC
SECTION AC-AC
SCALE 1 : 8
60
51
63
61
59
123
Name
Madeline Elkins, Neumark Group
Phone/ e-mail
3-9301 melkins@berkeley.edu
Scale 1:8
Tolerance: 1/32
unless noted
TITLE:
Full trap chamber, view 2
Part sheet 2 of 2
Project sheet 2 of 13
5
4
3
2
1

Figure C.4:

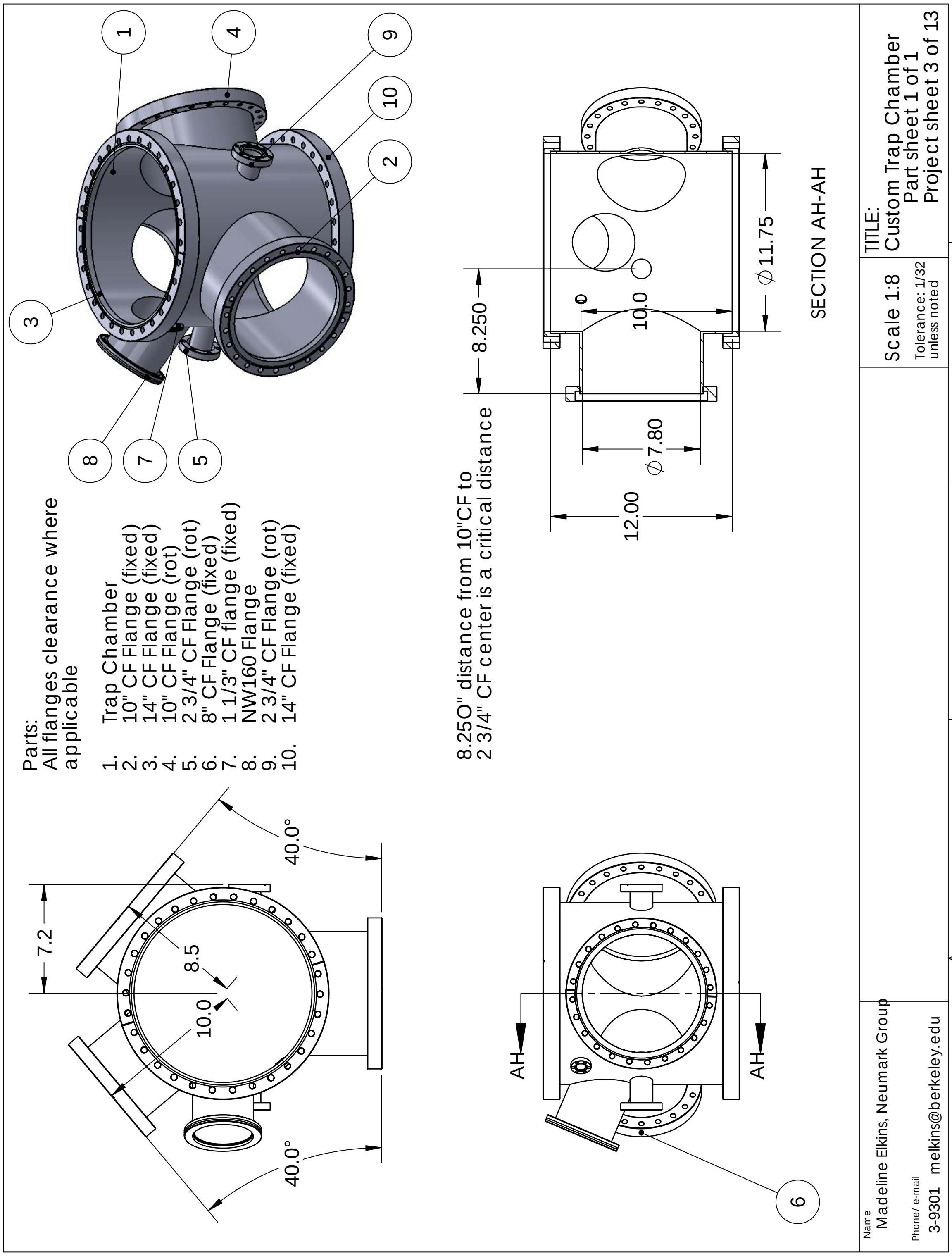
Parts:
All flanges clearance where applicable
1. Trap Chamber
2. 10" CF Flange (fixed)
3. 14" CF Flange (fixed)
4. 10" CF Flange (rot)
5. 2 3/4" CF Flange (rot)
6. 8" CF Flange (fixed)
7. 1 1/3" CF flange (fixed)
8. NW160 Flange
9. 2 3/4" CF Flange (rot)
10. 14" CF Flange (fixed)
8.25O" distance from 10"CF to 2 3/4" CF center is a critical distance
1
2
3
4
5
6
7
8
9
10
7.2
8.5
10.0
40.0°
40.0°
AH
AH
8.250
10.0
⌀11.75
⌀7.80
12.00
SECTION AH-AH
Name
Madeline Elkins, Neumark Group
Phone/ e-mail
3-9301 melkins@berkeley.edu
Scale 1:8
Tolerance: 1/32 unless noted
TITLE:
Custom Trap Chamber
Part sheet 1 of 1
Project sheet 3 of 13
1
2
3
4
5

Figure C.5:

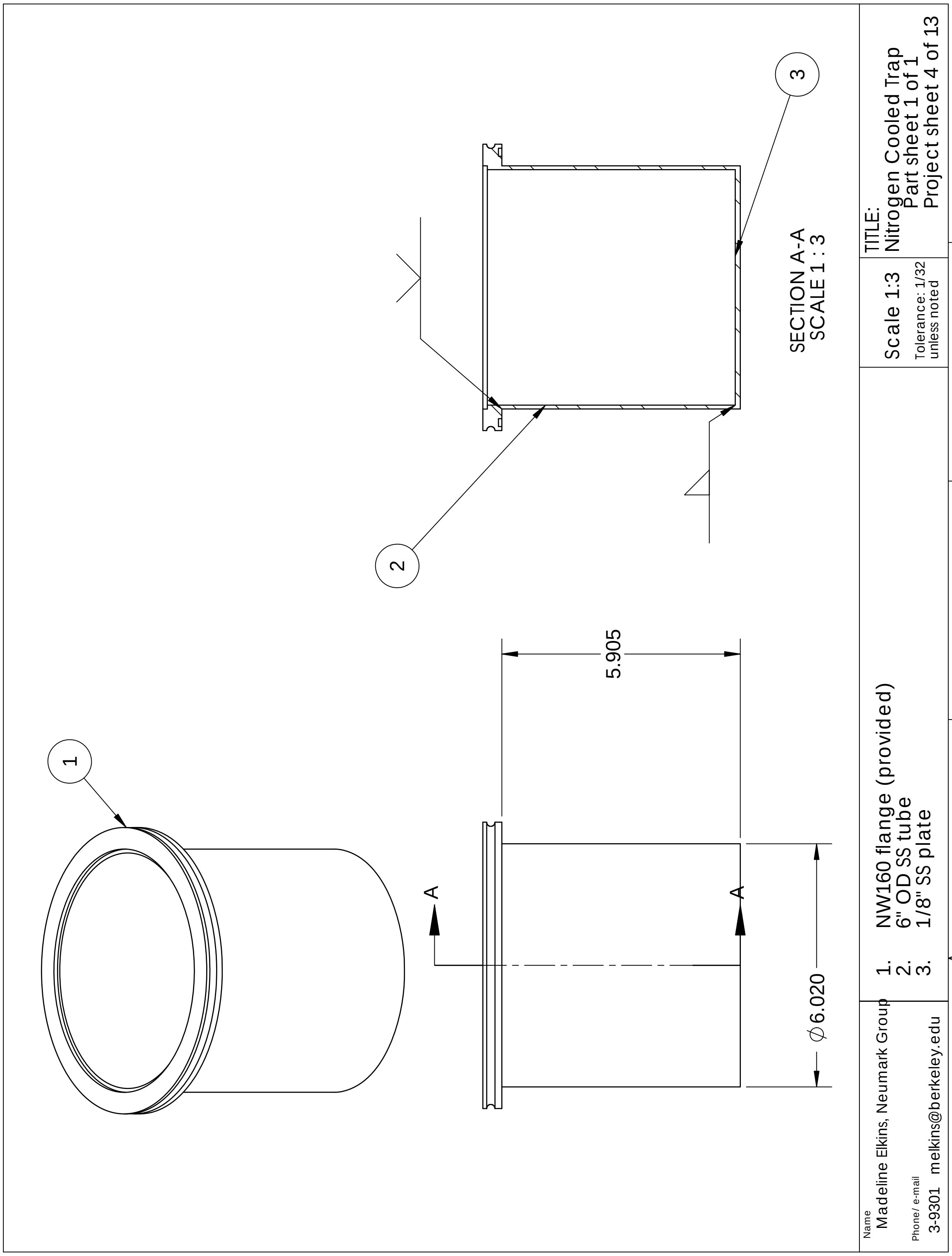
1
2
3
A
A
5.905
∅6.020
SECTION A-A
SCALE 1 : 3
1. NW160 flange (provided)
2. 6" OD SS tube
3. 1/8" SS plate
Name
Madeline Elkins, Neumark Group
Phone/ e-mail
3-9301 melkins@berkeley.edu
Scale 1:3
Tolerance: 1/32
unless noted
TITLE:
Nitrogen Cooled Trap
Part sheet 1 of 1
Project sheet 4 of 13
1
2
3
4
5

Figure C.6:

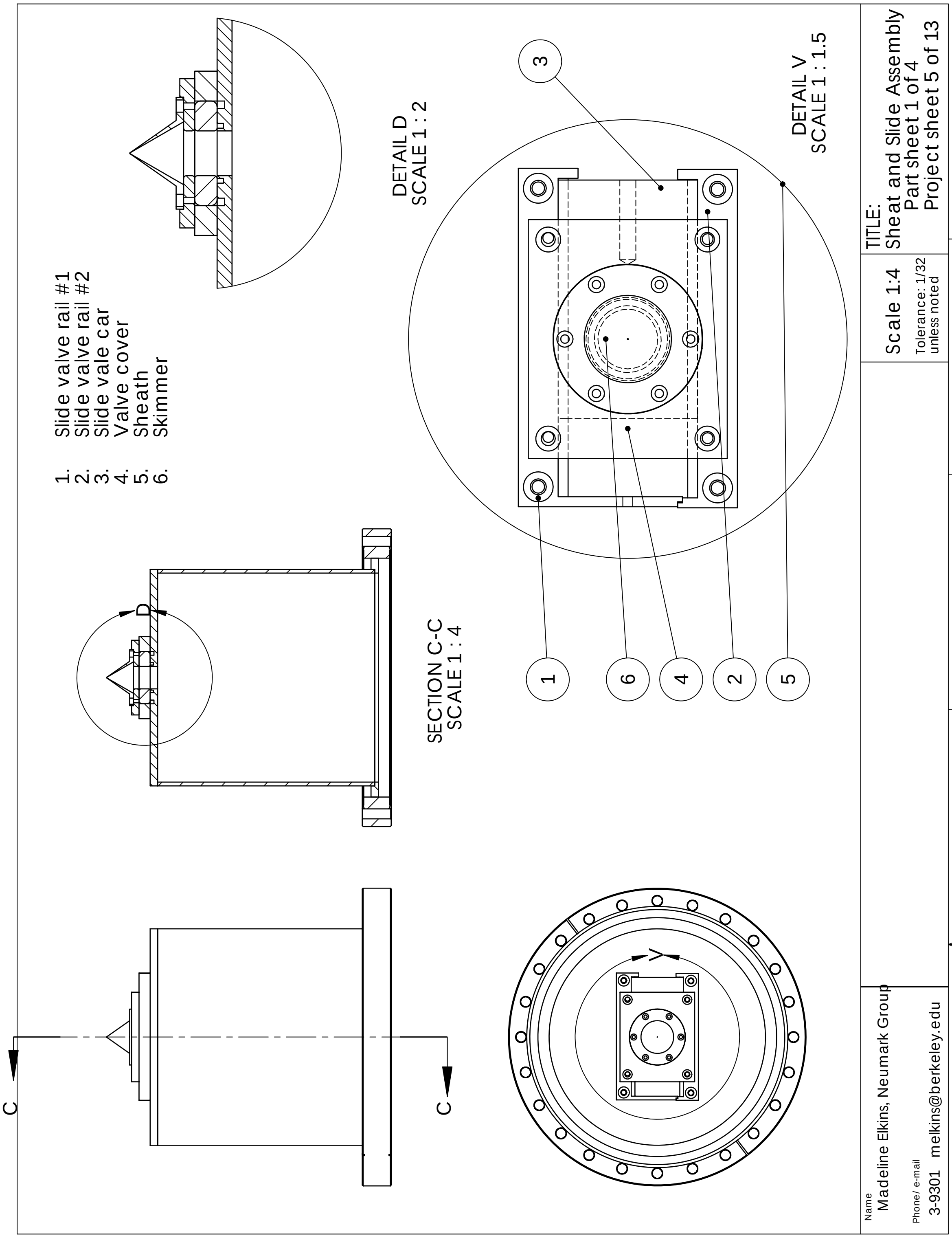
1. Slide valve rail #1
2. Slide valve rail #2
3. Slide vale car
4. Valve cover
5. Sheath
6. Skimmer
DETAIL D
SCALE 1 : 2
DETAIL V
SCALE 1 : 1.5
SECTION C-C
SCALE 1 : 4
D
V
C
C
1
2
3
4
5
6
TITLE:
Sheat and Slide Assembly
Part sheet 1 of 4
Project sheet 5 of 13
Scale 1:4
Tolerance: 1/32
unless noted
Name
Madeline Elkins, Neumark Group
Phone/ e-mail
3-9301 melkins@berkeley.edu
1
2
3
4
5

Figure C.7:

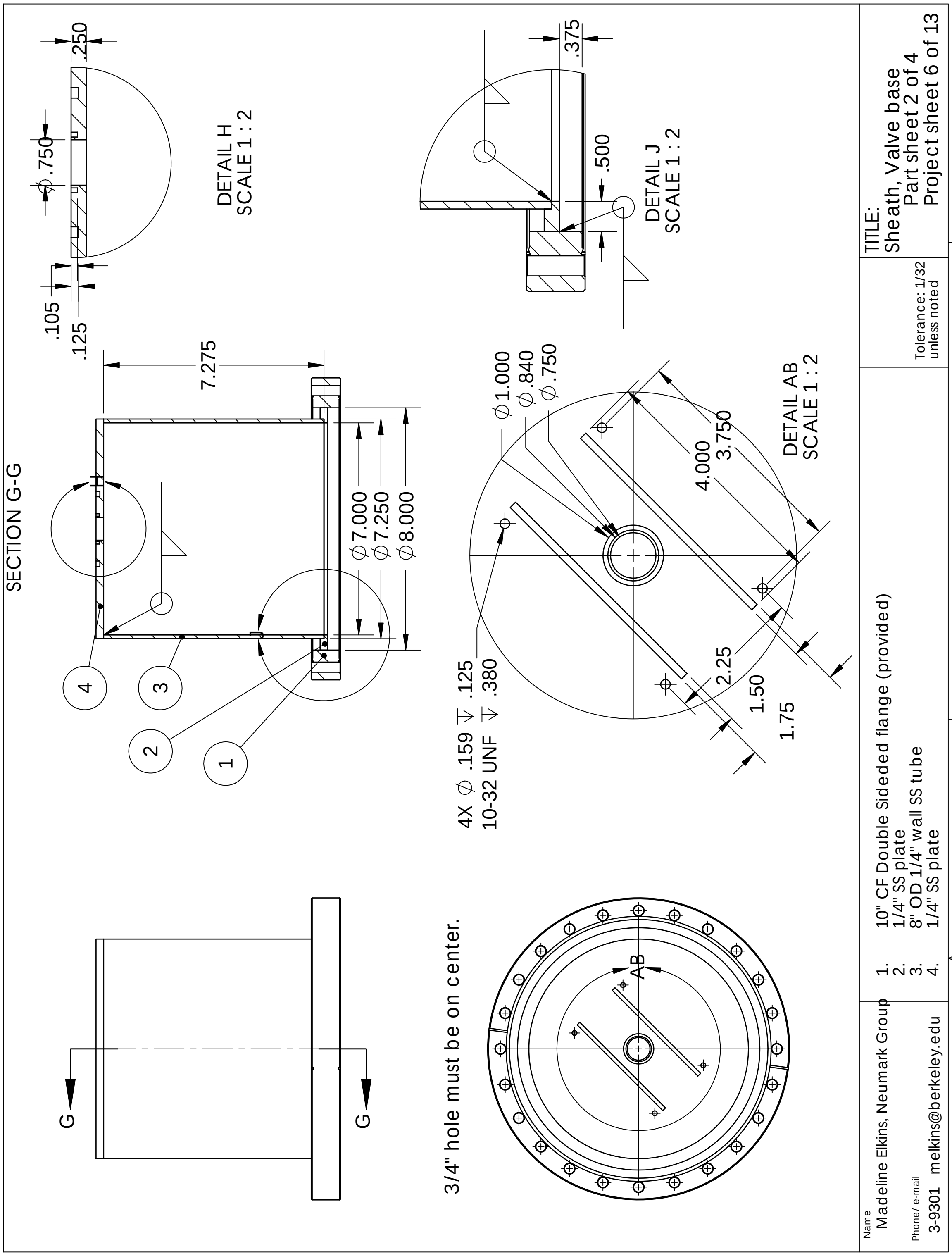
SECTION G-G
H
J
4
3
2
1
7.275
Ø7.000
Ø7.250
Ø8.000
.105
.125
.250
Ø.750
DETAIL H
SCALE 1 : 2
.375
.500
DETAIL J
SCALE 1 : 2
Ø1.000
Ø.840
Ø.750
4.000
3.750
DETAIL AB
SCALE 1 : 2
2.25
1.50
1.75
4X Ø .159 ⊽ .125
10-32 UNF ⊽ .380
G
G
AB
3/4" hole must be on center.
Name
Madeline Elkins, Neumark Group
Phone/ e-mail
3-9301 melkins@berkeley.edu
1. 10" CF Double Sideded flange (provided)
2. 1/4" SS plate
3. 8" OD 1/4" wall SS tube
4. 1/4" SS plate
Tolerance: 1/32
unless noted
TITLE:
Sheath, Valve base
Part sheet 2 of 4
Project sheet 6 of 13
1
2
3
4
5

Figure C.8:

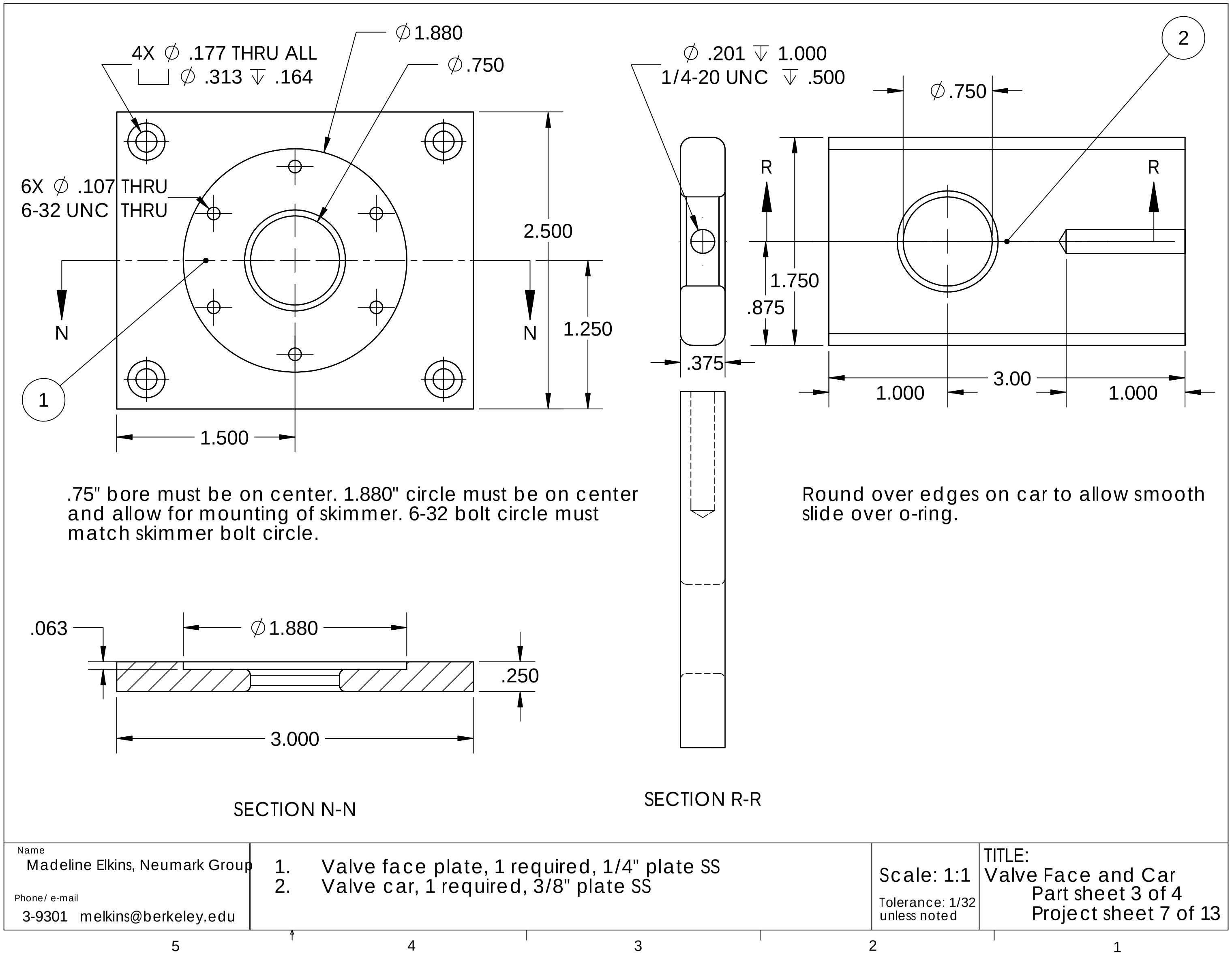

.75" bore must be on center. 1.880" circle must be on center and allow for mounting of skimmer. 6-32 bolt circle must match skimmer bolt circle.

Round over edges on car to allow smooth slide over o-ring.

Name
Madeline Elkins, Neumark Group
Phone/ e-mail
3-9301 melkins@berkeley.edu

1. Valve face plate, 1 required, 1/4" plate SS
2. Valve car, 1 required, 3/8" plate SS

Scale: 1:1
Tolerance: 1/32
unless noted

TITLE:
Valve Face and Car
Part sheet 3 of 4
Project sheet 7 of 13

Figure C.9:

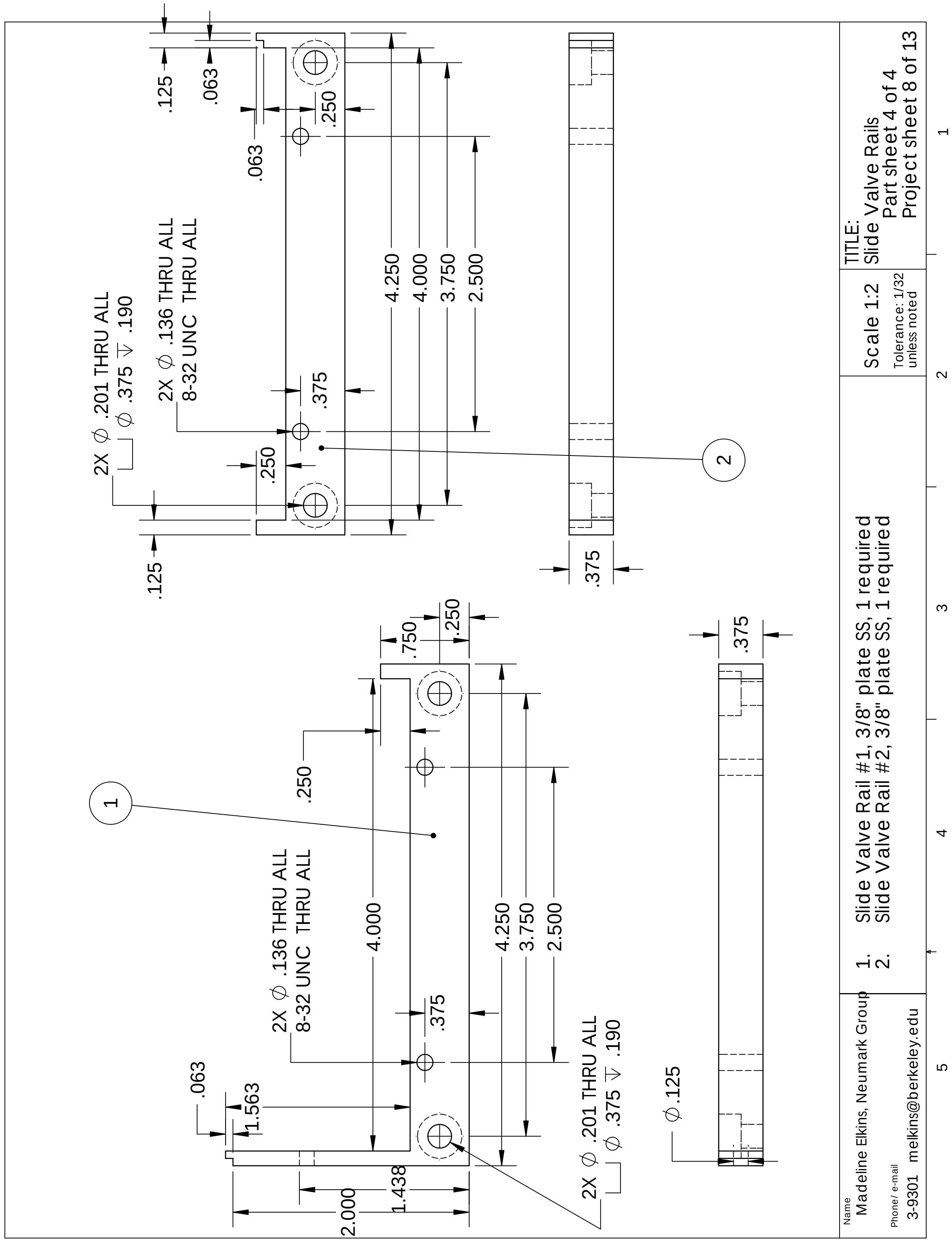
TITLE:
Slide Valve Rails
Part sheet 4 of 4
Project sheet 8 of 13
Scale 1:2
Tolerance: 1/32 unless noted
1. Slide Valve Rail #1, 3/8" plate SS, 1 required
2. Slide Valve Rail #2, 3/8" plate SS, 1 required
Name
Madeline Elkins, Neumark Group
Phone/ e-mail
3-9301 melkins@berkeley.edu
1
2
3
4
5
2X ⌀ .201 THRU ALL
⌴ ⌀ .375 ↧ .190
2X ⌀ .136 THRU ALL
8-32 UNC THRU ALL
.125
.063
.063
.250
.250
.375
4.250
4.000
3.750
2.500
.125
.375
.250
.750
.250
4.000
4.250
3.750
2.500
.375
.375
.063
1.563
1.438
2.000
⌀ .125

Figure C.10:

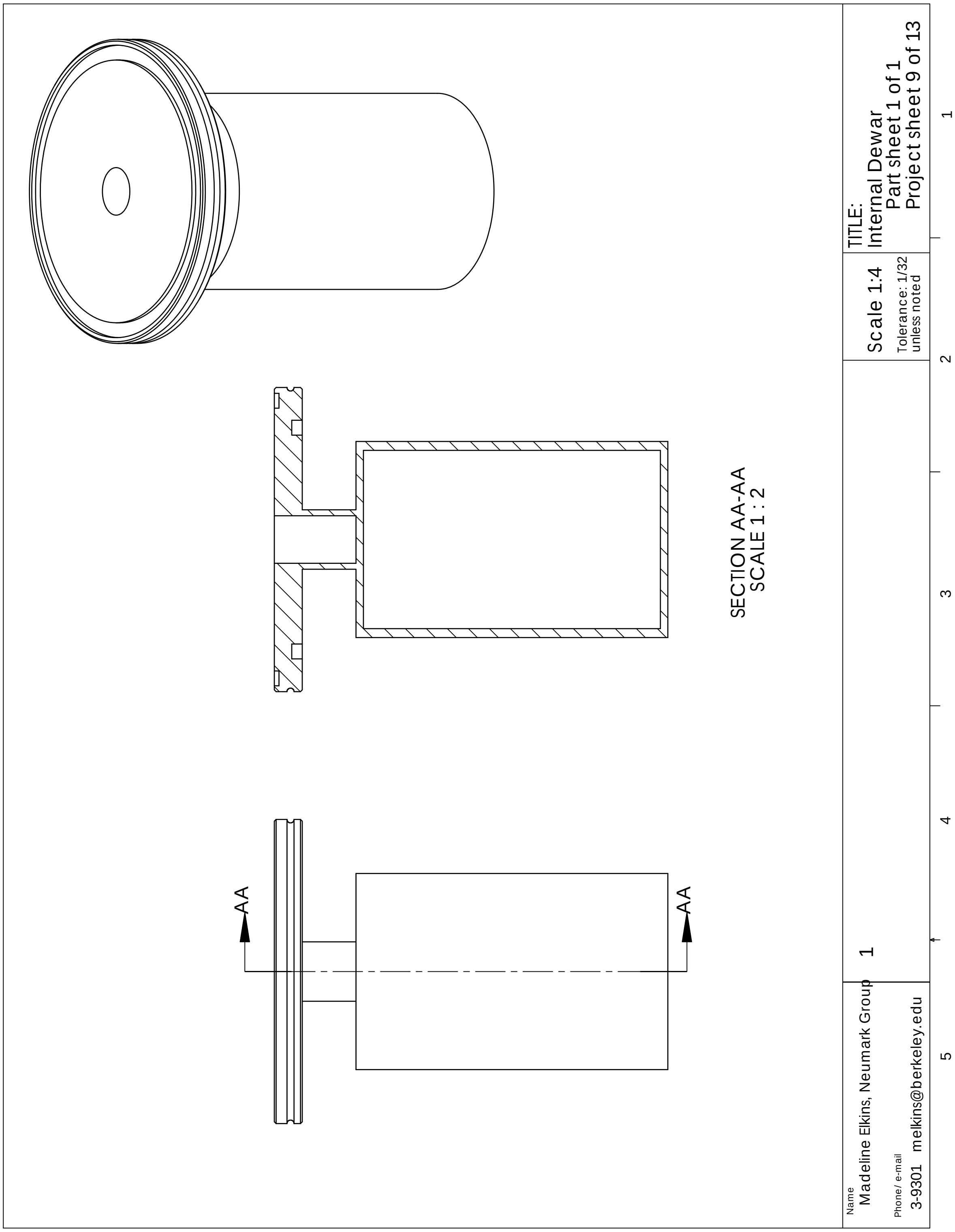
AA
AA
SECTION AA-AA
SCALE 1 : 2
TITLE:
Internal Dewar
Part sheet 1 of 1
Project sheet 9 of 13
Scale 1:4
Tolerance: 1/32
unless noted
Name
Madeline Elkins, Neumark Group
1
Phone/ e-mail
3-9301 melkins@berkeley.edu
1
2
3
4
5

Figure C.11:

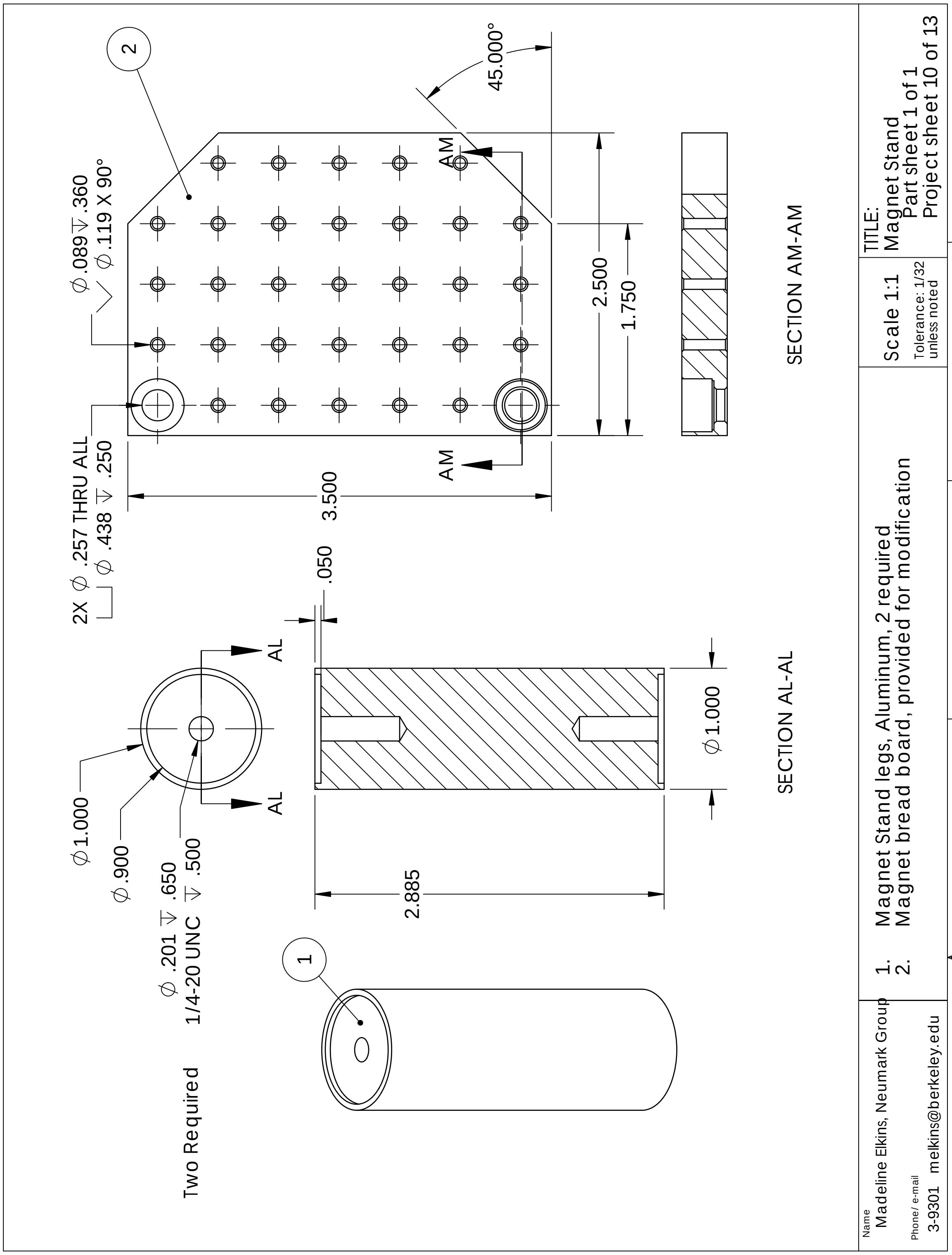
2
1
Two Required
Ø.089 ↧ .360
⌵ Ø.119 X 90°
2X Ø .257 THRU ALL
⌴ Ø .438 ↧ .250
45.000°
AM
AM
2.500
1.750
3.500
SECTION AM-AM
.050
AL
AL
Ø1.000
Ø.900
Ø .201 ↧ .650
1/4-20 UNC ↧ .500
2.885
Ø1.000
SECTION AL-AL
Name
Madeline Elkins, Neumark Group
Phone/ e-mail
3-9301 melkins@berkeley.edu
1. Magnet Stand legs, Aluminum, 2 required
2. Magnet bread board, provided for modification
Scale 1:1
Tolerance: 1/32 unless noted
TITLE:
Magnet Stand
Part sheet 1 of 1
Project sheet 10 of 13
1
2
3
4
5

Figure C.12:

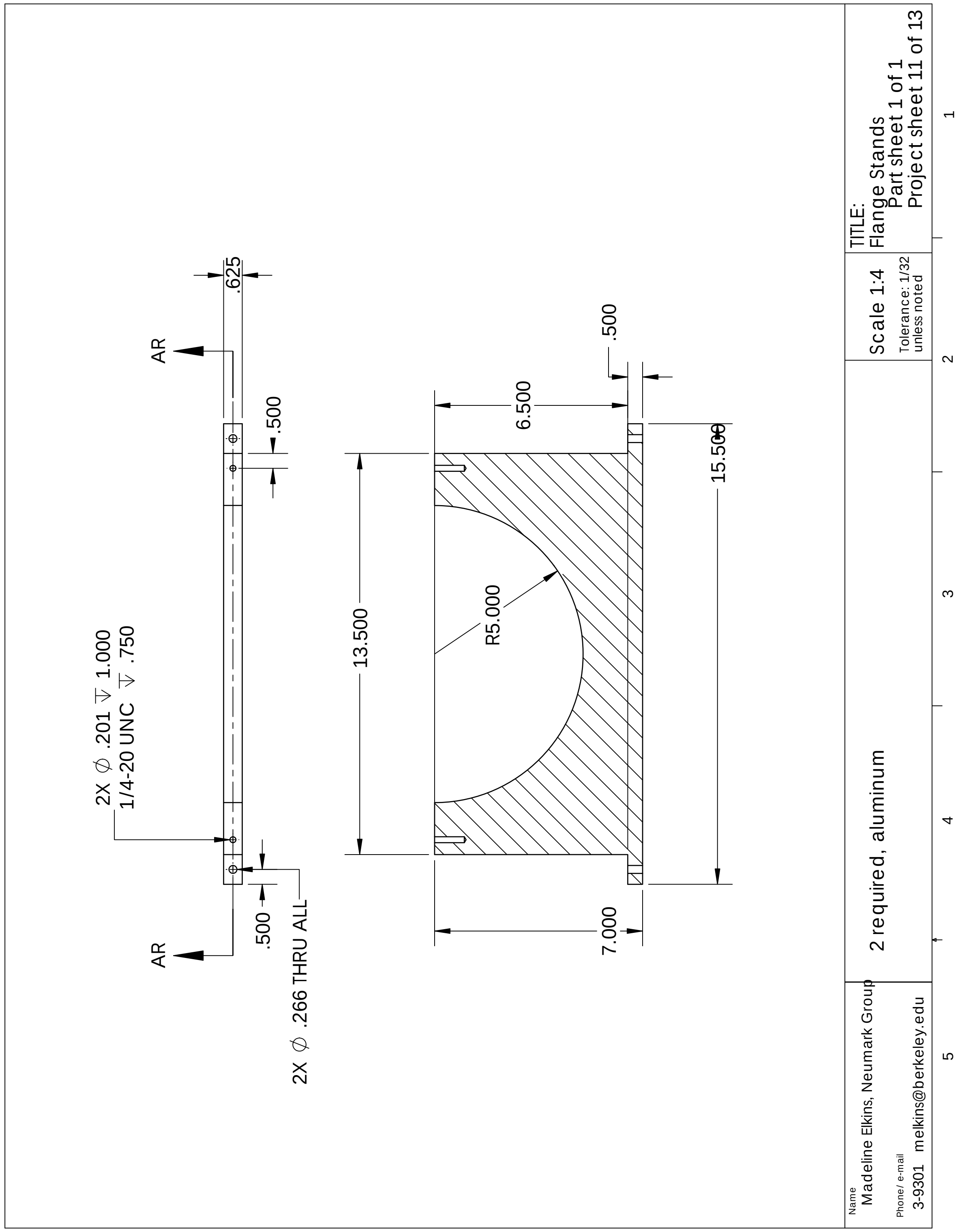
AR
.625
.500
2X ∅ .201 ↧ 1.000
1/4-20 UNC ↧ .750
.500
2X ∅ .266 THRU ALL
AR
6.500
.500
15.500
13.500
R5.000
7.000
Name
Madeline Elkins, Neumark Group
Phone/ e-mail
3-9301 melkins@berkeley.edu
2 required, aluminum
Scale 1:4
Tolerance: 1/32
unless noted
TITLE:
Flange Stands
Part sheet 1 of 1
Project sheet 11 of 13
1
2
3
4
5

Figure C.13:

Appendix D

Code: Post-Processing and Data Analysis

D.1 Post-Processor

```
%post processor

%directions:
%MUST CHANGE # OF BACKGROUND SCANS BASED ON TYPE OF DATA
%You will be asked which delay scan number should be used to find
   a flat base
%line
%You will be asked which region is non-flat in that delay

%% set-up, import
tau=[125,400];
IRFFWHM=100;
fig=1;
numbkgd = 1;

t0=-16;
len=66;

ekeEfile='CombinedSums.csv';
%ekeEfile='combinedsumsedit.csv';
configfile='ConfigTable.csv';

%datmatl=csvread(ekeEfile);
datmatl=csvread(ekeEfile,1,0);
```

```

numeKE=length(datmatl);
numdelays=size(datmatl,2)-numbkgd;

%confmat=csvread(configfile,0,0,[0,0,numdelays,0]);
confmat=csvread(configfile);
binstof = linspace(2, 2000, 1000);

%create column of eKE values
E=284.3174 .*(len^2./(binstof-t0).^2);
eeKE=E';

%create delays matrix
delays=(20/3*confmat(1:numdelays,2))';

%generate weights for jacobian transformation
datE=zeros(1000,numdelays);
dataE=zeros(1000,numdelays);

escale=eeKE.^(3/2);

%% Background subtraction
bkgd=zeros(numeKE,1);
for r=1:numbkgd;
bkgd=datmatl(:,numdelays+r)+bkgd;
end

Bkgd=[];
for l=1:numdelays
    Bkgd=[Bkgd,bkgd];
end

%subd=datmatl;
subd=datmatl(:,1:numdelays)-Bkgd;

%% Baseline Flattening
%user select delay for eKE lane
prompt = 'Enter number of delay to use for baseline correction';
lanes=inputdlg(prompt);
lane=str2double(lanes);

eKElane=subd(:,lane);
```

```

figure(20000135)

plot(binstof,eKElane)

excludes = inputdlg({'start ToF range to exlcude','end Tof range to exclude'},'Info');
vals1=excludes{1};
val1=str2double(vals1);
vals2=excludes{2};
val2=str2double(vals2);
exclude=(val1/2:1:val2/2);

b=-.004;

[xData, yData] = prepareCurveData( binstof, eKElane' );

% Set up fittype and options.
ft = fittype( 'linefit(x,b)', 'independent', 'x', 'dependent', 'y' );
excludedPoints = excludedata( xData, yData, 'Indices', exclude);
opts = fitoptions( 'Method', 'NonlinearLeastSquares' );
opts.Display = 'Off';
opts.StartPoint = b;
opts.Exclude = excludedPoints;

% Fit model to data.
[fitresult, gof] = fit( xData, yData, ft, opts );

fitresult

bs = coeffvalues(fitresult);
dataavg=subd-bs;

%% Jacobian Transformation

for n=1:numdelays
    dataE(:,n)= dataavg(:,n)./escale;
end

datmat=dataE;

```

```
%% Rebin to 10ns tof lanes

rusbd=[];
for l = 1: numdelays;
    for n = 1: numeKE/5
            rsubd(n,l) = datmat(5*n,l) + datmat(5*n-1,l) + datmat(5*n-2,l)+ datmat(5*n-3,l) + datmat(5*n-4,l);
    end
end

%% Write Mat File
newbinstof = linspace(10, 2000, 200);

%create column of eKE values
nE=284.3174 .*(len^2./(newbinstof-t0).^2);
neKE=nE';

newnumeKE=length(rsubd);

eKE=flipud(neKE(50:200));
ldelay=length(delays);
tTRPES=flipud(rsubd(50:200,1:ldelay));

filenamefitmat='BkgdBaselineJacScaleRebin.mat';
save(filenamefitmat,'IRFFWHM','tau','fig','delays','eKE','tTRPES');
```

D.2 Degenerate Global Fitter

Main Code

```
function [DAS, taus, decays, fit, residuals, t0, FWHM, y0] = DegenGlobalFit(tau, IRFFWHM, delays, eKE, TRPES, fig)
%%GlobalFit
%Perform a global fit on a TRPES matrix.

% INPUTS:
% tau = row vector of initial guesses for time constants
% IRFFWHM = intial guess for FWHM of the IRF
% delays = row vector of delays data were sampled at
% eKE = column vector of energies data were sampled at
```

```
% TRPES = matrix of TRPES data, in the format described by delays and eKE
% fig = no. of figure to output to.

% OUTPUTS:
% DAS = matrix of decay associated spectra, one column for each component
% taus = vector of time constants
% decays = matrix of time-integrated signals. First n columns are the
%          decays for each n componenets, followed by the experimental data, then
%          the total fit
% fit = matrix of fitted TRPES
% residuals = matrix of experiment - fit
% t0 = fitted t0
% FWHM = fitted FWHM
% y0 = fitted linear offset (accounts for noise)

%[rTRPES, binseKE]=rebinbyenergygap(eKE,delays,binSize,TRPES);
rTRPES = TRPES;
binseKE = eKE;
sigma = IRFFWHM / 2.35;
%rTRPES=rTRPES(1:length(binseKE),:)

persistent cstring;

%Plot raw data as contour in figure 1, position 1 in 3x2
figure(fig);
subplot(3,2,1);
[cha,cha] = contourf(delays, binseKE, rTRPES , 25);
set(cha,'linestyle','none');
ax = caxis;
title('Data');
xlabel('t / fs');
ylabel('eKE / eV');
%axis([-500 2500 binSize max(eScale)]);
colorbar;
drawnow;

%create initial values for fit
x0 = ones(length(binseKE)+4, length(tau))*0.1;
```

```
x0(1,:) = tau;
x0(2,1) = -10; %t0
x0(3,1) = 0; %y0
x0(4,1) = sigma;

%uncomment these and change the fit line to use limits.

 %lower = ones(length(binseKE)-3, length(tau))*-5;
 %lower(1,:) = [20,500,1000]; %tau
 %lower(2,1) = -100; %t0
 %lower(3,1) = -1; %y0
 %lower(4,1) = 50/2.35; %FWHM

 %upper = ones(length(binseKE)+3, length(tau))*5;
 %upper(1,:) = [300,1000, 8000];%tau
 %upper(2,1) = 100; %t0
 %upper(2,2) = 1; %y0
 %upper(3,1) = 300/2.35; %FWHM


%generate weights (to account for non-linear eKE axis)
%N.B. the *10 factor is to get the residulas into a regime the fitter
%likes. Tweaking this can change the tolerance and fitting speed
weight = repmat(diff(eKE),1,length(delays));
weight = [weight; repmat(weight(end,1), 1, length(delays))]*10000;

%% Start with the default options
options = optimset;
%% Modify options setting
options = optimset(options,'Display', 'iter-detailed');
options = optimset(options,'ScaleProblem', 'Jacobian');
options = optimset(options,'PlotFcns', { @outfun });
[x,resnorm,residual,exitflag,output,lambda,jacobian] = ...
lsqnonlin(@(x)((GenerateDegenTRPES(delays,binseKE,x(1,:),x(5:end,:),x(2,1),x(4,1),x(3,1))-rTRPES).*weight).*1,x0,[],[],options);

%% if limits are required, replace the [], [], above with lower, upper - and fill out the matricies above.

taus = x(1,:)
```

```
t0 = x(2,1)
y0 = x(3,1)
FWHM = x(4,1)*2.35

%x(4:end,2)= zeros(length(eScale),1);

fitTRPES = GenerateDegenTRPES(delays, binseKE, taus, x(5:end,:),
    t0, FWHM/2.35, y0);
fit = fitTRPES;

figure(fig);
subplot(3,2,2);
[chb,chb] = contourf(delays, binseKE, fitTRPES, 25);
set(chb,'linestyle','none');
caxis(ax);
title('Fit');
xlabel('t / fs');
ylabel('eKE / eV');
colorbar;
drawnow;

%% plot DAS
subplot(3,2,3);
cla;
DAS = plotDAS(x);
drawnow;

%% plot residuals
subplot(3,2,4);
residuals = (fitTRPES - rTRPES);
[chc,chc] = contourf(delays, binseKE, residuals, 25);
set(chc,'linestyle','none');
caxis(ax - max(ax)/2);
title('Residuals');
xlabel('t / fs');
ylabel('eKE / eV');
colorbar;
drawnow;

%% plot decays
subplot(3,1,3);
cla;
```

```
decays = plotDecays(x);


%% function to plot the DAS
    function DAS = plotDAS(xc)
        cstring=[];

        DAS = zeros(length(binseKE), length(xc(1,:)));
        for i=(1:length(xc(1,:)))
            plot(binseKE, xc(5:end,i));
            DAS(:,i) = xc(5:end,i);

            %legend(sprintf('%0.1f fs', x(1,i)));
            cstring{end+1} = sprintf('%0.0f fs', xc(1,i));
            hold all;
        end
        hold off;
        title('Decay Associated Spectra');
        xlabel('eKE / eV');
        hline = refline([0 0]);
        set(hline, 'Color', 'k');
        legend(cstring);
    end

%%function to plot total integrals
    function decays = plotDecays(xc)
        decays = zeros(length(xc(1,:)) + 2, length(delays));
        decays(length(xc(1,:)) + 2, :) = trapz(binseKE, GenerateDegenTRPES(delays, binseKE, xc(1,:), xc(5:end,:),xc(2,1), xc(4,1), xc(3,1)));
        decays(length(xc(1,:)) + 1, :) = trapz(binseKE, rTRPES);

        plot((delays(1:end)), trapz(binseKE, GenerateDegenTRPES((delays(1:end)), binseKE, xc(1,:), xc(5:end,:),xc(2,1), xc(4,1), xc(3,1))), 'k');
        hold all;
        plot(delays, trapz(binseKE, rTRPES), 'ok');
        for i=(1:length(xc(1,:)))
            singleComp = zeros(length(binseKE), length(tau));
            singleComp(:,i) = xc(5:end,i);
            plot((delays(1:end)), trapz(binseKE, GenerateDegenTRPES((delays(1:end)), binseKE, xc
```

```
               (1,:), singleComp,xc(2,1), xc(4,1), xc(3,1))));
            decays(i,:) = trapz(binseKE, GenerateDegenTRPES(delays
               , binseKE, xc(1,:), singleComp, xc(2,1), xc(4,1),
               xc(3,1)));
        end

        title('Total Integral');
        xlabel('t / fs');
        legend(sprintf('sigma = %0.0f fs', xc(4,1)), sprintf('t0 =
            %0.0f fs', xc(2,1)));
        hold off;
    end

%%function to plot real time fit results
    function stop = outfun(xc,optimvalues, state)
        stop = false;
        switch state
            case 'iter'
                subplot(2,1,1);
                plotDAS(xc);

                subplot(2,1,2);
                plotDecays(xc);

            otherwise
                hold off;
        end
    end
end
```

Fit Function for Global Fit

```
function [ TRPES ] = GenerateDegenTRPES( delays, eKE, tau, DAS, t0
   , sigma, y0 )
%GenerateTRPES
%This function generates a full TRPES matrix, given the delays,
   energy
%scale, decay assoc. spectra, etc.

TRPES = zeros(length(DAS), length(tau));

for i=(1:length(delays))
```

```
    TRPES(:,i) = GenerateDegenPES(DAS, tau, delays(i), t0, sigma, y0);
end
end
```

```
function [ PES ] = GenerateDegenPES(DAS, tau, t, t0, sigma, y0 )
%Returns the convoluted and decayed spectra at time t, given a decay
%associated spectra matrix, DAS, t0; the cross correlation,
%sigma; and an offset factor y0

%initialize the PES vector
PES = ones(length(DAS(:,1)), 1).*y0 ;

%loop through each decay component
for i=(1:length(tau))
    B = (sigma^2/(2*tau(i)^2)) - (t - t0)/tau(i);
    C = erfc( (-1/sqrt(2)) .* (tau(i)/abs(tau(i))*(t-t0)/sigma - sigma/tau(i)));

    PES = PES + (DAS(:,i) .* exp(B) .* C);
end
end
```

D.3 Confidence Intervals for Degenerate Fitter

Main Code

```
%Basic support plane analysis for 2 variable (time constant global
%fit) A DEGENERATE FITTER

%space of tau values over which to optimize, should be centered around the
%optimum value, where 80 is the number of steps. Optimization chi2 contours
%will be a #stepsx#steps matix consisting of a least squares fit at every
%value (big)
tau1 = linspace(30, 200, 100);
tau2 = linspace(200, 1000, 100);
tau3 = -120000;
tau4 = 120000;
```

```matlab

%initialize chi matrix
chi = zeros(length(tau1), length(tau2));
% chi matrix will be a ratio of chi versus chiMin, these are your optimum fit
% values
chiMin = DegenGlobalFitFixed([-120000,81, 457,120000], FWHM, delays, eKE, tTRPES, 23);
n=length(tau1);

%loop that generates the chi^2 values
parfor j = 1:length(tau2)
    for i = 1:n
        chi(i, j) = DegenGlobalFitFixed([tau3 tau1(i) tau2(j) tau4], FWHM, delays, eKE, tTRPES, 23);
        [tau1(i) tau2(j)]
        [j i]
    end
end

%final contour with full matrix
figure(22377);
contour(tau2, tau1, chi/chiMin);
figure(22379);
contourf(tau2, tau1, chi/chiMin);

%calculate plane of values that give 95% confidence
p = length(delays) + length(eKE)*3 + 5; %%%SET FOR DTMP
v = length(tTRPES(:)) - p;
chiRatio = 1+finv(0.95, p, v) * p/v

hold all;
[c1,h1]= contour(tau2, tau1, chi/chiMin, [chiRatio chiRatio]);
set(h1,'linecolor','k');
set(h1,'linewidth',3);
```

Fixed Lifetime Global Fitter

```matlab
function [chisq] = DegenGlobalFitFixed(tau, IRFFWHM, delays, eKE, TRPES, fig)
%%GlobalFit
%Perform a global fit on a TRPES matrix.
```

```

% INPUTS:
% tau = row vector of initial guesses for time constants
% IRFFWHM = intial guess for FWHM of the IRF
% delays = row vector of delays data were sampled at
% eKE = column vector of energies data were sampled at
% TRPES = matrix of TRPES data, in the format described by delays and eKE
% fig = no. of figure to output to.

% OUTPUTS:
% DAS = matrix of decay associated spectra, one column for each component
% taus = vector of time constants
% decays = matrix of time-integrated signals. First n columns are the
%          decays for each n componenets, followed by the experimental data, then
%          the total fit
% fit = matrix of fitted TRPES
% residuals = matrix of experiment - fit
% t0 = fitted t0
% FWHM = fitted FWHM
% y0 = fitted linear offset (accounts for noise)

%[rTRPES, binseKE]=rebinbyenergygap(eKE,delays,binSize,TRPES);
rTRPES = TRPES;
binseKE = eKE;
sigma = IRFFWHM / 2.35;
%rTRPES=rTRPES(1:length(binseKE),:)

persistent cstring;

%create initial values for fit
x0 = ones(length(binseKE)+4, length(tau))*0.1;
x0(1,:) = tau;
x0(2,1) = 0; %t0
x0(3,1) = 0; %y0
x0(4,1) = sigma;

%uncomment these and change the fit line to use limits.

```

```
 %lower = ones(length(binseKE)-3, length(tau))*-5;
 %lower(1,:) = [20,500,1000]; %tau
 %lower(2,1) = -100; %t0
 %lower(3,1) = -1; %y0
 %lower(4,1) = 50/2.35; %FWHM

 %upper = ones(length(binseKE)+3, length(tau))*5;
 %upper(1,:) = [300,1000, 8000];%tau
 %upper(2,1) = 100; %t0
 %upper(2,2) = 1; %y0
 %upper(3,1) = 300/2.35; %FWHM


%generate weights (to account for non-linear eKE axis)
%N.B. the *10 factor is to get the residulas into a regime the
    fitter
%likes. Tweaking this can change the tolerance and fitting speed
weight = repmat(diff(eKE),1,length(delays));
weight = [weight; repmat(weight(end,1), 1, length(delays))]*10000;

%% Start with the default options
options = optimset;
%% Modify options setting
%options = optimset(options,'Display', 'iter-detailed');
options = optimset(options,'ScaleProblem', 'Jacobian');
%options = optimset(options,'PlotFcns', { @outfun });
[x,chisq,residual,exitflag,output,lambda,jacobian] = ...
lsqnonlin(@(x)((GenerateDegenTRPES(delays,binseKE,x(1,:),x(5:end
    ,:),x(2,1),x(4,1),x(3,1))-rTRPES).*weight).*1,x0,[],[],options)
    ;

%% if limits are required, replace the [], [], above with lower,
    upper - and fill out the matricies above.

taus = x(1,:);
t0 = x(2,1);
y0 = x(3,1);
FWHM = x(4,1)*2.35;

%x(4:end,2)= zeros(length(eScale),1);

```

```
fitTRPES = GenerateDegenTRPES(delays, binseKE, taus, x(5:end,:), t0, FWHM/2.35, y0);
 fit = fitTRPES;


%% function to plot the DAS
    function DAS = plotDAS(xc)
        cstring=[];

        DAS = zeros(length(binseKE), length(xc(1,:)));
        for i=(1:length(xc(1,:)))
            plot(binseKE, xc(5:end,i));
            DAS(:,i) = xc(5:end,i);

            %legend(sprintf('%0.1f fs', x(1,i)));
            cstring{end+1} = sprintf('%0.0f fs', xc(1,i));
            hold all;
        end
        hold off;
        title('Decay Associated Spectra');
        xlabel('eKE / eV');
        hline = refline([0 0]);
        set(hline, 'Color', 'k');
        legend(cstring);
    end

%%function to plot total integrals
    function decays = plotDecays(xc)
        decays = zeros(length(xc(1,:)) + 2, length(delays));
        decays(length(xc(1,:)) + 2, :) = trapz(binseKE, GenerateDegenTRPES(delays, binseKE, xc(1,:), xc(5:end,:),xc(2,1), xc(4,1), xc(3,1)));
        decays(length(xc(1,:)) + 1, :) = trapz(binseKE, rTRPES);

        plot((delays(1:end)), trapz(binseKE, GenerateDegenTRPES((delays(1:end)), binseKE, xc(1,:), xc(5:end,:),xc(2,1), xc(4,1), xc(3,1))), 'k');
        hold all;
        plot(delays, trapz(binseKE, rTRPES), 'ok');
        for i=(1:length(xc(1,:)))
            singleComp = zeros(length(binseKE), length(tau));
            singleComp(:,i) = xc(5:end,i);
```

```
            plot((delays(1:end)), trapz(binseKE, GenerateDegenTRPES((delays(1:end)), binseKE, xc(1,:), singleComp,xc(2,1), xc(4,1), xc(3,1))));
            decays(i,:) = trapz(binseKE, GenerateDegenTRPES(delays, binseKE, xc(1,:), singleComp, xc(2,1), xc(4,1), xc(3,1)));
        end

        title('Total Integral');
        xlabel('t / fs');
        legend(sprintf('sigma = %0.0f fs', xc(4,1)), sprintf('t0 = %0.0f fs', xc(2,1)));
        hold off;
    end

%%function to plot real time fit results
    function stop = outfun(xc,optimvalues, state)
        stop = false;
        switch state
            case 'iter'
                subplot(2,1,1);
                plotDAS(xc);
                subplot(2,1,2);
                plotDecays(xc);

            otherwise
                hold off;
        end
    end
end
```

D.4 Shifting Global Fitter

```
function [tauds, tauts, x0s, xiinfs, wi0s, wiinfs, fit, residuals, t0s, sigmas, y0s] = ShiftingFit(taud, taut,xi0,xiinf,wi0,wiinf, IRFFWHM, delays, eKE, TRPES, fig)
%INPUTS:
% eKE = column vector of energies data were sampled at
% taud = row vector of guesses for the decay rate constants
% taut = row vector of guesses for the thermalization rate constants
```

```
% xiinf = row vector of guesses for the center of the peak at long time
% xi0 = row vector of guesses for the initial center of the peak
% wi = row vector of guesses for the width of the peak
% delays = row vector of delays data were sampled at
% IRFFWHM = guess for width of laser pulse, full width half max of
% autocorrelation
% TRPES = matrix of TRPES data, in the format described by delays and eKE
% fig = no. of figure to output to.

% OUTPUTS:
% tauds,tauts = vector of time constants
% fit = matrix of fitted TRPES
% residuals = matrix of experiment - fit
% t0s = fitted t0
% sigmas = fitted FWHM
% y0s = fitted linear offset (accounts for noise)
hold off;
cla;

figure(fig);

rTRPES = TRPES;
binseKE = eKE;
sigma = IRFFWHM / 2.35; %convert to sigma of gaussian

persistent cstring;

%Plot raw data as contour in figure(fig), subplot position 1 in 3 x2
figure(fig);
subplot(3,2,1);
[cha,cha] = contourf(delays, binseKE, rTRPES , 25);
set(cha,'linestyle','none');
ax = caxis;
title('Data');
xlabel('t (fs)');
ylabel('eKE (eV)');
%axis([-500 2500 binSize max(eScale)]);
colorbar;
drawnow;
```

```

%create matrix of initial values for fit
x0 = ones(9, length(taud));
x0(1,:) = taud;
x0(2,:) = taut;
x0(3,:) = xi0;
x0(4,:) = xiinf;
x0(5,:) = wi0;
x0(6,:) = wiinf;
x0(7,1) = -200; %t0
x0(8,:) = 0.01; %y0
x0(9,1) = sigma;


%uncomment these and change the fit line to use limits.

 %lower = ones(length(binseKE)-3, length(tau))*-5;
 %lower(1,:) = [20,500,1000]; %tau
 %lower(2,1) = -100; %t0
 %lower(3,1) = -1; %y0
 %lower(4,1) = 50/2.35; %FWHM

 %upper = ones(length(binseKE)+3, length(tau))*5;
 %upper(1,:) = [300,1000, 8000];%tau
 %upper(2,1) = 100; %t0
 %upper(2,2) = 1; %y0
 %upper(3,1) = 300/2.35; %FWHM


%generate weights (to account for non-linear eKE axis)
%N.B. the *10 factor is to get the residulas into a regime the fitter
%likes. Tweaking this can change the tolerance and fitting speed
weight = repmat(diff(eKE),1,length(delays));
weight = [weight; repmat(weight(end,1), 1, length(delays))]*10000000;

%% Start with the default options
options = optimset;
%% Modify options setting
options = optimset(options,'Display', 'iter-detailed');
options = optimset(options,'ScaleProblem', 'Jacobian');
```

```
options = optimset(options,'PlotFcns', { @outfun });
[x,resnorm,residual,exitflag,output,lambda,jacobian] = ...
lsqnonlin(@(x)((GeneratePESshift(binseKE,x(1,:),x(2,:),x(3,:),x
    (4,:),x(5,:),x(6,:),delays,x(7,1),x(9,1),x(8,:))-rTRPES).*
    weight).*1,x0,[],[],options);

%% if limits are required, replace the [], [], above with lower,
    upper - and fill out the matricies above.

%write out new fit params from fit
tauds = x(1,:);
tauts = x(2,:);
x0s = x(3,:);
xiinfs = x(4,:);
wi0s = x(5,:);
wiinfs = x(6,:);
t0s = x(7,1); %t0
y0s = x(8,:); %y0
sigmas = x(9,1);

fitTRPES = GeneratePESshift(binseKE, tauds,tauts,x0s,xiinfs,wi0s,
    wiinfs,delays, t0s, sigmas, y0s);
fit = fitTRPES;

figure(fig);
subplot(3,2,2);
[chb,chb] = contourf(delays, binseKE, fitTRPES, 25);
set(chb,'linestyle','none');
caxis(ax);
title('Fit');
xlabel('t  (fs)');
ylabel('eKE (eV)');
colorbar;
drawnow;

%% plot spectra
subplot(3,2,3);
cla;
[SPECTRA0, SPECTRAinf] = plotSPECTRA(x);
drawnow;

%% plot residuals
```

```
subplot(3,2,4);
residuals = (fitTRPES - rTRPES);
[chc,chc] = contourf(delays, binseKE, residuals, 25);
set(chc,'linestyle','none');
caxis(ax - max(ax)/2);
title('Residuals');
xlabel('t  (fs)');
ylabel('eKE (eV)');
colorbar;
drawnow;

%% plot decays
subplot(3,1,3);
cla;
decays = plotDecays(x);

hold off


%% function to plot the spectra
    function [SPECTRA0, SPECTRAinf] = plotSPECTRA(xc)
        cstring=[];

        SPECTRA0 = zeros(length(binseKE), length(xc(1,:)));
        SPECTRAinf = zeros (length(binseKE), length(xc(1,:)));
        for i=(1:length(xc(1,:)))
            for n=1:length(binseKE)
            spectraw0(n)=xc(8,i)/(xc(5,i)*2*pi)* exp(-2*(eKE(n)-xc(3,i)).^2/(xc(5,i)^2));
            spectrawiinf(n) =xc(8,i)/(xc(6,i)*2*pi)* exp(-2*(eKE(n)-xc(4,i)).^2/(xc(6,i)^2));
            end
            plot(binseKE, spectraw0);
            hold all;
            plot(binseKE, spectrawiinf);
            SPECTRA0 (:,i) = spectraw0(i);
            SPECTRAinf(:,i) = spectrawiinf(i);

            %legend(sprintf('%0.1f fs', x(1,i)));
            cstring{end+1} = sprintf('%0.0f fs decay', xc(1,i));
            cstring{end+1} = sprintf('%0.0f fs shift', xc(2,i));
        end
```

```
        hold off;
        title('Initial and Final Spectra');
        xlabel('eKE (eV)');
        hline = refline([0 0]);
        set(hline, 'Color', 'k');
        legend(cstring);

    end

%%function to plot total integrals
    function decays = plotDecays(xc)
        decays = zeros(length(xc(1,:)) + 2, length(delays));
        decays(length(xc(1,:)) + 2, :) = trapz(binseKE, GeneratePESshift(binseKE,xc(1,:),xc(2,:),xc(3,:),xc(4,:),xc(5,:),xc(6,:),delays,xc(7,1),xc(9,1),xc(8,:))); %fit integrated
        decays(length(xc(1,:)) + 1, :) = trapz(binseKE, rTRPES); %raw data integrated(delays(1):10:delays(end))

        plot((delays(1):10:delays(end)), trapz(binseKE, GeneratePESshift(binseKE,xc(1,:),xc(2,:),xc(3,:),xc(4,:),xc(5,:),xc(6,:),(delays(1):10:delays(end)),xc(7,1),xc(9,1),xc(8,:))), 'k');
        hold all;
        plot(delays, trapz(binseKE, rTRPES), 'ok');
        for i=(1:length(xc(1,:)))
            plot((delays(1):10:delays(end)),trapz(binseKE,GeneratePESshift(binseKE,xc(1,i),xc(2,i),xc(3,i),xc(4,i),xc(5,i),xc(6,i),(delays(1):10:delays(end)),xc(7,1),xc(9,1),xc(8,i))) );
        end

        title('Total Integral');
        xlabel('t (fs)');
        legend(sprintf('sigma = %0.0f fs', xc(9,1)), sprintf('t0 = %0.0f fs', xc(7,1)));
        hold off;
    end

%%function to plot real time fit results
    function stop = outfun(xc,optimvalues, state)
        stop = false;
```

```
        switch state
            case 'iter'
                subplot(2,1,1);
                plotSPECTRA(xc);

                subplot(2,1,2);
                plotDecays(xc);

            otherwise
                hold off;
        end

    end
end
```

Generate PES Shift

```
function [ TRPES ] = GeneratePESshift(eKE,taud,taut,xi0,xiinf,wi0, wiinf, delays, t0, sigma, y0 )
%INPUTS:
% eKE = column vector of energies data were sampled at
% taud = row vector of guesses for the decay rate constants
% taut = row vector of guesses for the thermalization rate constants
% xiinf = row vector of guesses for the center of the peak at long time
% xi0 = row vector of guesses for the initial center of the peak
% wi = row vector of guesses for the width of the peak
% delays = row vector of delays data were sampled at
% t0 = guess for zero pump-probe delay time
% sigma = guess for width of laser pulse
% y0 = guess for the amplitude of the gaussian

%OUTPUTS:
%TRPES : a matrix of energy x delay values subject to inital guess and
% fit function below

%fitting function for a three color data with allowed shifting.
TRPES = zeros(length(eKE), length(delays));
statea = zeros(length(eKE), length (delays));

```

```
for k= 1 : length(taud)

    B = (sigma.^2/(2*taud(k).^2)) - (delays - t0)/taud(k); % exponential in each decay component
    C = erfc( (-1/sqrt(2)) .* ((delays - t0)/sigma - sigma/taud(k))); %instrument response
    xi = xiinf(k) + (xi0(k) - xiinf(k)) * exp(- (delays -t0)/taut(k)) ; %shifting center of gaussian
    wi = wiinf(k) + (wi0(k) - wiinf(k)) * exp(- (delays -t0)/taut(k)) ; %shifting width of gaussian

 for n = 1 : length (eKE)
     for l = 1 : length(delays)
        statea(n,l) = C(l).* exp(B(l)).* y0(k)/(wi(l)*2*pi)*exp(-2*(eKE(n)-xi(l)).^2/(wi(l)^2)) ;
     end
 end
   TRPES = TRPES + statea;
end
end
```

Appendix E

Publications from Graduate Work

- **Elkins, M. H.**, Williams, H. W., Shreve, A. T., Neumark, D. M., Relaxation Mechanism of the Hydrated Electron. *Science*, **342**, 1496, (2013).

- Shreve, A. T., **Elkins, M. H.**, Neumark, D. M., Photoelectron Spectroscopy of Solvated Electrons in Alcohol and Acetonitrile Microjets, *Chemical Science*, **4**, 1633, (2013).

- **Elkins, M. H.**, Williams, H. W., Neumark, D. M., Dynamics of Electron Solvation in Methanol: Excited State Relaxation and Generation by Charge Transfer to Solvent, *Journal of Chemical Physics*, **142**, 234501, (2015).

- **Elkins, M. H.**, Williams, H. W., Neumark, D. M., Dynamics of Electron Solvation in Ethanol: Excited State Relaxation and Generation by Charge Transfer to Solvent Excitation, *In Prep.*

- **Elkins, M. H.**, Williams, H. W., Neumark, D. M., Isotope Effect of the Internal Conversion Lifetime of Photoexcited Solvated Electrons in Water and Deuterium Oxide, *In Prep.*